Universiteit Antwerpen

UNIVERSITY OF ANTWERP

MASTER THESIS

A study of the ETpathfinder longitudinal control through optical simulations

Author:
Karel PEETERMANS

Supervisor:
Prof. Dr. Hans VAN HAEVERMAET

A thesis submitted in fulfilment of the requirements for the degree of Master of Physics

at

EDF group, Department of Physics

29th May, 2023

"*The concept of what we're looking for is so important. The fact that the effect is tiny is just our misfortune.*"

- Rainer Weiss [1]

UNIVERSITY OF ANTWERP

Abstract

Faculty of Science

Department of Physics

Master of Physics

A study of the ETpathfinder longitudinal control through optical simulations

by Karel PEETERMANS

The Einstein Telescope pathfinder (ETpf) is an R&D facility located at Maastricht University, dedicated to exploring innovative techniques for the next generation of gravitational wave (GW) detectors. The primary focus of this thesis is on optical simulations for ETpf, which play a crucial role in the transition from the simulated phase to the experimental phase of the project. The main areas of investigation are the longitudinal control of the interferometer and laser-induced noise sources. Additionally, the thesis demonstrates the effect of introducing folding mirrors to the geometry, which causes an asymmetry in the arms. Regarding interferometer control, proven techniques based on frontal laser modulation are applied to control the arm cavities and the main degrees of freedom of the interferometer. The achieved sensitivities show promise, although for optimal performance more advanced systems would have to be implemented. This study further shows the need to effectively suppress laser frequency and amplitude noise within the specified budget. The impact of various design parameters, including a Michelson offset, the Schnupp asymmetry and the presence of an etalon in the input mirror, is investigated to assess their influence on noise levels. The effect of the asymmetry in the arms is limited in both topics, indicating that the folding mirrors will not present issues for the project. By delving into these areas, the aim is to contribute to the advancement of gravitational wave detector technologies, particularly in the context of ETpf.

Acknowledgements

I would like to thank my supervisor prof. dr. Hans Van Haevermaet for guiding me through the process of working on this project. He patiently taught me how to use FINESSE and was always available whenever I had trouble understanding what was going wrong. During our meetings he consistently provided good insight and suggested new directions for my research. I also very much appreciate his support throughout writing the thesis.

I am very thankful for my office coworkers of the EDF group. Our coffee breaks provided a nice social moment between work sessions. As a young researcher, their advice was very valuable to me while starting my entry into the field of physics research.

Lastly, I am grateful for the ETpf community for providing the opportunity to work with them. The simulation meetings with members from across Europe were a great place to ask questions to experts in the field. They also invited me to the ETpf workshop where I got to meet my colleagues and discuss the progress of the experiment.

Contents

Chapter 1

Overview

The field of gravitational wave (GW) astronomy has opened new horizons in mankind's understanding of the universe, allowing researchers to detect and study cosmic events with unprecedented precision as well as make observations of the universe at its earliest stages. As the whole sector enters the era of GW astronomy, the development of advanced technologies for the next generation of gravitational wave detectors becomes crucial. The Einstein Telescope pathfinder (ETpf) is an R&D facility located at Maastricht University dedicated to exploring innovative techniques and methodologies to enhance the capabilities of future GW detectors. The project is purely focused on development rather than making detections. This thesis is conducted within the framework of the ETpf project and aims to address several key objectives related to simulations of the ETpf interferometer. The primary goals are to investigate and optimise the longitudinal control of the interferometer and examine laser-induced noise sources. By employing simulations using FINESSE, a powerful tool for modelling interferometric systems, insights are gained into the performance and limitations of the ETpf design.

The next chapter of this thesis discusses the concepts and theory necessary to treat these topics in-depth. A brief overview of GWs and their detection methods is provided. The focus is on gravitational wave interferometers, which detect the passing of a wave by analysing the interference of the two perpendicular laser beams. A detailed approach to the implementation of arm cavities is given, as well as the theoretical background surrounding phase-modulation of the laser. Specifically, a frontal modulation scheme is reviewed since it will be applied to control the arm cavities and the main degrees of freedom of the interferometer. Furthermore, the ETpf experiment specifically will be introduced as well as the technologies it will be researching in function of the Einstein Telescope (ET) and other future observatories. The goals and strategies of the ET project are discussed. Moreover, the different noise sources that provide a challenge for ET are examined as well as how they could be mitigated. This provides context for the laser-related noise sources that will be examined in chapter four.

The third chapter delves into methods for the longitudinal control of the interferometer. The first part is dedicated to the control of the arm cavities. Cavity control involves the attempt to tune the mirror positions of a cavity to preserve its resonance condition, which ensures it sufficiently amplifies the laser field inside the cavity. To this end, a fraction of the laser field is extracted and analysed to be used as an error signal. This is where the modulation of the laser carrier proves useful, the signal can be demodulated, and the resulting signal is highly sensitive to any deviations of the cavity mirror position. Alternatively, this type of signal can instead be used to correct the laser frequency. The error signal response to the resonance deviations is then analysed in function of a few design parameters such as modulation index and mirror transmittance. Furthermore, the same ideas are applied to the

whole interferometer, which has several degrees of freedom that need to be controlled. The resulting system can be represented in a matrix equation coupling the degrees of freedom to the error signals. Theoretical predictions of this matrix are provided which are then compared to the simulated results. After that, the performance of the simulated system is reviewed, and a brief overview is given of more advanced systems that might be used to achieve results comparable to other experiments like Virgo.

The fourth and final chapter presents an analysis of laser frequency- and amplitude-related noise. These are inherent to any optical input system and should therefore be investigated to anticipate future challenges. The influence of various design parameters on noise transfer is examined, including the impact of a DC offset, Schnupp asymmetry and an etalon in the input mirror of the arm cavities. The latter induces higher order effects that occur from the mirror no longer being an infinitesimally thin surface, but rather allowing internal reflections like it would in reality. All these design choices increase the transfer of laser noise to the output port, where the gravitational wave is being measured. Moreover, the necessary gain factors required for effective noise suppression within the predefined noise budget are predicted.

Chapter 2

Introduction

2.1 Gravitational waves

In the same way that a photon can be seen as a wave or perturbation in the electric and magnetic field, a Gravitational Wave (GW) is a travelling perturbation in spacetime. The most important currently known source of gravitational waves are large masses which orbit each other and eventually collide. This is similar to the behaviour of orbiting electric charges, which will emit electromagnetic radiation as a result of their orbit since they experience acceleration. In contrast, the effect of a GW is not measured in any field but in the distortion of spacetime itself. More specifically, they do not perturb positions of anything in spacetime itself but rather the relative distances between them. A typical wave will periodically stretch and compress spacetime in the plane perpendicular to its motion, resulting in periodically longer and shorter distances between points in spacetime. Stretching in one direction corresponds to compressing in the perpendicular direction and vice versa. [2, chpt. 16]

The existence of gravitational waves had already been theoretically predicted soon after the development of general relativity, but their direct detection has formed a large problem up until recent years. This is very justifiable, as the effect of such waves is extremely small. For example, a 'standard' gravitational signal would only change lengths by one part in 10^{21}, or the order of $\frac{1}{1000}$ of a proton diameter in 3 kilometres [2, chpt. 1]. The dimensionless quantity indicating the amount of length change is called the *strain* h, which is the amplitude of the gravitational wave producing the effect. It appears in the spacetime metric after linearisation, causing lengths to be changed by a factor $\sqrt{1+h} \approx 1 + \frac{1}{2}h$. Therefore $h = \dfrac{2\Delta L}{L}$ for L some spatial dimension. This last relation already hints at the fact that a single body that is only subject to gravitational interactions, also called a test particle, does not suffice to detect a gravitational wave. In the reference frame of one such particle, it simply remains at rest while a wave passes. The effect only becomes noticeable when two or more test particles are considered, as their relative distance will be influenced by the wave. It is important to note that particles held together by other stronger forces would not see their relative distance being changed in the same way. For example, a steel rod is held together by bonds which are many orders stronger than the effect of a GW from a source far away. Such a rod could therefore be placed next to two test particles and be used as a reference to verify that the distance between the test particles has increased or decreased. [2, chpt. 16]

The first indirect evidence of the existence of GWs was found in the changing of pulsar frequencies,

which dates back to 1984. GWs are emitted from pulsars orbiting each other, causing the system to lose energy and increase its frequency over time. The loss of energy can be calculated from frequency measurements and is attributed to the emission of GWs. This is also why pulsar timing arrays are used for the measurement of GWs (mostly in the high frequency range). Today, they are also being directly detected here on earth by interferometer-based gravitational detectors. This technology is currently in what is called the second generation (2G) with the most important detectors being Advanced Virgo in Italy, the two Advanced LIGO detectors in the US and KAGRA in Japan. The Einstein Telescope will be part of the third generation (3G) of gravitational interferometers. It is currently under development for the 2030's. The demand for new detectors is not only driven by the search for higher sensitivities, but also by the need for cross-validation. Only when the gravitational signal is measured at different detectors at almost exactly the same time, other possible sources of signals can be excluded. Multiple perspectives of the same wave can also provide more information on the distance and direction of the source. In fact, the third generation is expected to make so many precise observations, they can be used as an astronomical tool, much like an optical telescope. Of course, these types of detectors need to have an incredible amount of precision to be statistically certain of the wave properties. [3] The process by which this certainty is achieved will be discussed in the following chapters.

The 'easiest' types of gravitational waves to detect are those originating from binary black holes (BBH) and binary neutron stars (BNS). When orbiting each other, they continually send out GW. These waves have twice the frequency of the orbit itself (typically detectable frequencies are 10 - 1000 Hz). As stated earlier however, spacetime is so rigid that this effect is barely noticeable at a distance. The amplitude of the wave is inversely related to the distance from the object. However, when the two masses come closer and closer and eventually collide, the resulting gravitational waves will be significantly stronger before dying out after the collision. The frequency of the signal also increases as the orbital frequency increases. This sudden increase in amplitude and frequency is called the *chirp* (fig. 2.1), which is detectable on earth if the objects are massive enough and not too far away. When the full merger and ringdown is captured in a GW-detector, the signal can be matched to simulation results to deduce properties of the original two masses and the final created mass. [2, chpt. 16]

At the time of writing, the sector is striving to enter the age of GW astronomy. The 2G detectors are currently operational and making weekly detections. ET will improve this event-frequency drastically, to perhaps an hourly rate. Making frequent precise detections allows testing currently accepted physical theories as well as selecting or rejecting proposed ones. This includes testing general relativity for the inspiral, merger and post-merger phase of a BBH. Furthermore, several dark matter and dark energy proposals can be evaluated. With better precision across the line, ET can attempt to detect stochastic backgrounds for GWs that trace back to the very early universe. These signals would date back further than the cosmic microwave background and exhibit physics at extremely high energy scales. The data ET would collect on GWs would allow researchers to study exciting new subjects across many different branches of physics. In the end this all leads to a much-improved understanding of the universe, and could allow promising new technologies to be developed. [4, Chpt. 1-2]

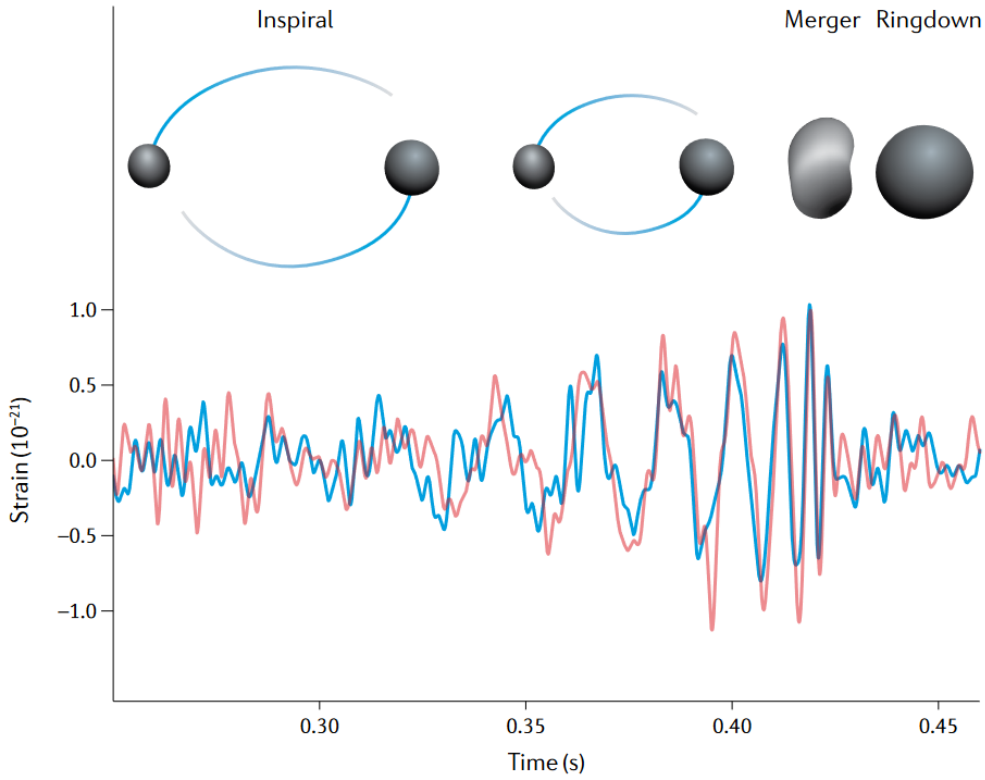

FIGURE 2.1: Amplitude of gravitational waves during the merger of two black holes [3, p. 346].

2.2 Interferometry for gravitational wave detection

To understand interferometers (ITFs) for GW detection, first the basic concepts of interferometry must be discussed. The type that is used in most GW experiments is a Michelson interferometer. The most basic layout is shown in figure 2.2. A laser beam is split into two perpendicular directions by the beam splitter (BS) and both beams travel multiple km's to a mirror at the end of a vacuum tunnel. The mirrors in gravitational detectors are often called test masses (TM), the ones at the end of the arms are called end mirrors (EM) or end test masses (ETM). After hitting the EMs, both beams return and get combined, which will cause the two beams to interfere with each other. The resulting superposition will then be measured by the photodetector (PD). [5, Chpt. 5] [6, chpt. 7]

The light wave can be characterised using the plane wave solution $A(x) = A_0 e^{ikx}$ with $k = \frac{2\pi}{\lambda}$ the wavenumber, λ the wavelength and A_0 the initial (complex) amplitude of the field at $x = 0$. Here only one dimension for the position is used which either represents the west-east axis or the south-north axis. A beam passing through the BS will acquire some phase, which is set to $\phi_{BS} = 90°$ in the simulations of this work. This results in a phase factor of $e^{i\phi_{BS}} = i$. The light hitting the north EM is

$$A(\text{NEM}) = \frac{1}{\sqrt{2}} A_0 e^{ikL_N}, \tag{2.1}$$

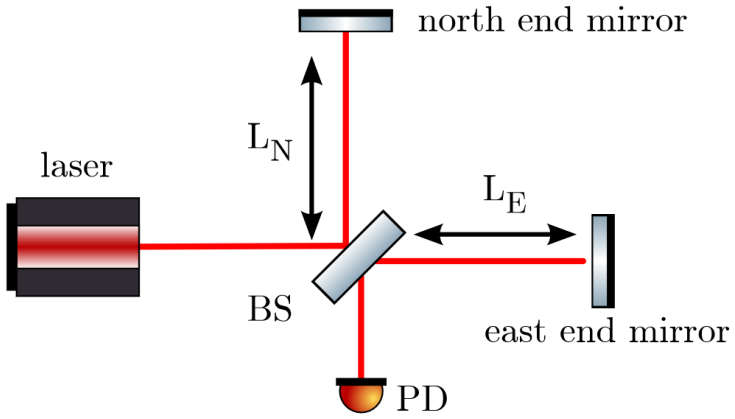

FIGURE 2.2: Optical layout of a basic Michelson interferometer [5, Chpt. 5].

where any phase acquired before the BS is added to A_0. It is assumed the BS divides the intensity I of the beam into two halves perfectly, meaning the reflected coefficient contains $\frac{1}{\sqrt{2}}$ s.t.

$$\frac{I}{I_0} = \frac{|A(\text{NEM})|^2}{|A_0|^2}| = \frac{1}{2}. \tag{2.2}$$

For the east EM the beam first passes through the BS, therefore adding the phase ϕ_{BS}. The field becomes

$$A(\text{EEM}) = \frac{e^{i\phi_{BS}}}{\sqrt{2}} A_0 e^{ikL_E} = \frac{i}{\sqrt{2}} A_0 e^{ikL_E}. \tag{2.3}$$

Before reaching the output port, the beam coming from the north travels through the arm in the other direction, meaning the total phase from hitting the EM and coming back is $2ikL_N$. This beam also has to pass through the BS, which adds $e^{i\phi_{BS}}$ as well. The beam coming from the east only reflects off the BS. At the output port the two beams recombine and experience interference. The light-field at the PD can then be expressed as the following superposition

$$A(\text{PD}) = \frac{1}{\sqrt{2}} e^{i\phi_{BS}} \left[\frac{1}{\sqrt{2}} A_0 e^{2ikL_N} \right] + \frac{1}{\sqrt{2}} \left[\frac{i}{\sqrt{2}} A_0 e^{2ikL_E} \right] \tag{2.4}$$

$$= \frac{i}{2} A_0 \left(e^{\text{i}2kL_N} + e^{\text{i}2kL_E} \right). \tag{2.5}$$

The following definitions of common arm-length and arm-length difference are now used

$$\bar{L} = L_N + L_E \tag{2.6}$$

$$\Delta L = L_N - L_E, \tag{2.7}$$

so that

$$A(\text{PD}) = \frac{i}{2} A_0 \left(e^{\text{i}k(\bar{L}+\Delta L)} + e^{\text{i}k(\bar{L}-\Delta L)} \right) = iA_0 e^{\text{i}k\bar{L}} \cos(k\Delta L). \tag{2.8}$$

The intensity measured by the PD is then

$$I(\text{PD}) = A(\text{PD}) A(\text{PD})^* = A_0^2 \cos^2(k\Delta L). \tag{2.9}$$

The signal is therefore periodic in the differential motion of the end mirrors and insensitive to any common motion [5, Chpt. 5]. Often it is chosen to have a slight offset between the two arms, shifting the zero point to the *dark fringe*, i.e. $\Delta L = \Delta L' + \frac{\pi}{2}$. This means the y-arm is set 90° back s.t. a round trip adds a 180° phase. This ensures if $\Delta L' = 0$ the signal will be zero as well. This transforms the signal equation to

$$I(\text{PD}) = A_0^2 \cos^2(k\Delta L' + \frac{\pi}{2}) = A_0^2 \sin^2(k\Delta L'). \tag{2.10}$$

2.2.1 Measurement of a gravitational wave

Equation 2.10 shows the sensitivity to the detection of gravitational waves. As a wave passes the path lengths and $\Delta L'$ will change and this will alter the measured intensity I. Some formulas are taken from [2, Chpt. 16] to clarify this point. Assume for simplicity a wave hits the ITF with amplitude h and angular frequency ω in the so-called '+ polarisation', which influences a ring of test particles like illustrated in figure 2.3. It may also be assumed the GW arrives perpendicularly to the ITF, and that the arms line up perfectly with the x- and y-axis. In this case the lengths between the BS and the EMs change periodically following

$$\frac{\delta L_x}{L_x} = +\frac{1}{2} h \sin(\omega t), \qquad \frac{\delta L_y}{L_y} = -\frac{1}{2} h \sin(\omega t). \tag{2.11}$$

This immediately implies $\Delta L' = h \sin(\omega t)$, meaning the signal at the PD is

$$I(\text{PD}) = A(\text{PD}) A(\text{PD})^* = A_0^2 \sin^2 [kh \sin(\omega t)] \approx A_0^2 k^2 h^2 \sin^2(\omega t). \tag{2.12}$$

The amplitude and frequency of this detected signal can now be retrieved to know what the GW looked like. Qualitatively, what happens is that space is distorted and the length of the light's path changes. The time it takes to travel back and forth to the ETM will periodically increase and decrease, causing a phase difference when reaching the BS. During the passing of the wave, the beams will therefore no longer destructively interfere perfectly in the detector. Suddenly, some photons will be measured and this is interpreted as the measurement of the GW. The duration and intensity of the signal is of course strongly dependent on the source of the wave [7, chpt. 3].
This illustrates the importance of the mirrors behaving like test particles, for if the mirrors were not free to move the path length of the light would not be changed. In that case, the GW would not be measured. The TMs will generally be suspended and isolated from all other sources of force so only gravitation applies. Only then can the GW be discerned. The amplitudes h are generally very small and difficult to observe, thus all sources of noise should also be reduced as much of possible. The situation becomes more complicated for different polarisations, angles of incidence and frequency spectra, but these ideas form the foundation for this detection method. [2, Chpt. 16] [6, chpt. 7]

To enhance the previously mentioned interferometer, optical cavities (Fabry-Perot cavities) will be used in the arms of the detector to increase the effective distance travelled. An example of such a setup is shown in fig. 2.4. Light enters through a semi-reflective input test mass (ITM) and bounces off the end test mass (ETM), which is nearly fully reflective. Upon returning to the ITM, a substantial proportion will be reflected back into the arm. This happens repeatedly of course, and depending on the reflectance of the ITM, the mean distance travelled by the light can be found. Since the mean

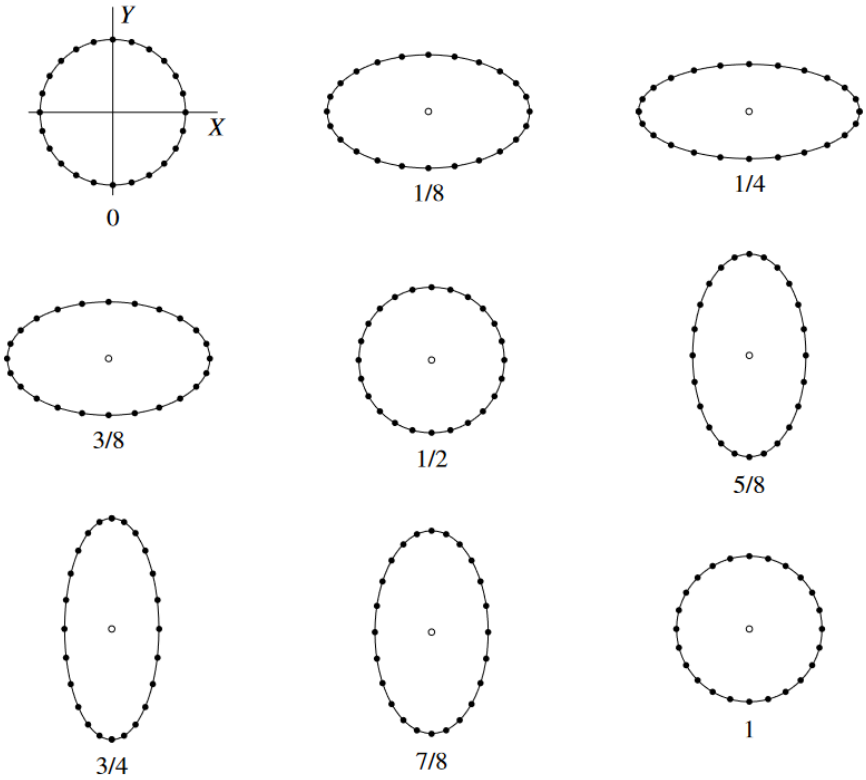

FIGURE 2.3: Illustration of a GW with the + polarisation [2, Chpt. 16].

distance increases by a lot, the effect of the GW on the interference is also much larger, allowing for an easier detection. [6, chpt. 7] Arm cavities are studied in more detail in section 2.2.2.

2.2.2 Optical arm cavities

Resonance

The mirrors that are used are semi-transparent and their reflectance R and transmittance T need to be balanced. If one assumes mirrors without loss, $R+T=1$. In figure 2.4, the ITM and ETM form an optical cavity for each arm. The distance between the mirrors is characterised by two lengths: the macroscopic length L and a phase-angle ϕ. The macroscopic length is approximately the distance between the two mirrors, in case of ETpf this would be around 9.22m but for ET this will be in the order of multiple km. This length is used for example for calculating the focal lengths of the mirrors etc. The phase refers to the precise microscopic 'tuning' of the positions of the mirrors. ϕ corresponds to a difference in distance of the order of wavelengths. For example, 360° corresponds to placing the mirror one wavelength further back. 180° would mean half of a wavelength, resulting in a full wavelength difference when considering the round-trip path. If the total distance of the cavity is exactly an integer multiple of the wavelength, it is in *resonance*. In the case of resonance, the cavity amplifies the power of the signal significantly because a standing wave is formed that gets amplified by the light entering the cavity [9]. The resonance effect is seen in figure 2.6, corresponding to $\mathrm{PD}_{\mathrm{circ}}$

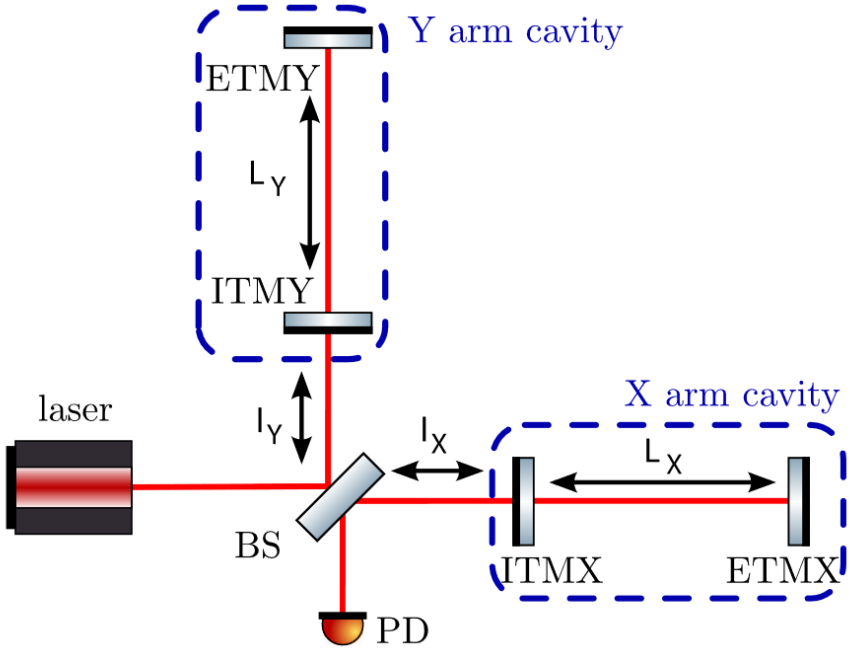

FIGURE 2.4: Simplified optical layout of a gravitational interferometer [8, Chpt. 7].

in figure 2.5.[1] The wavelength that is generally used in this work is $\lambda = 1550$ nm, which is one of the wavelengths used in ETpf.

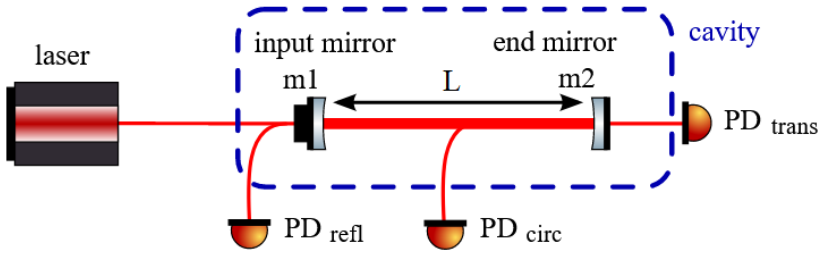

FIGURE 2.5: Schematic layout of one optical cavity [9].

[1] The plots in section 2.2.2 have been made by adapting FINESSE code from GWoptics.

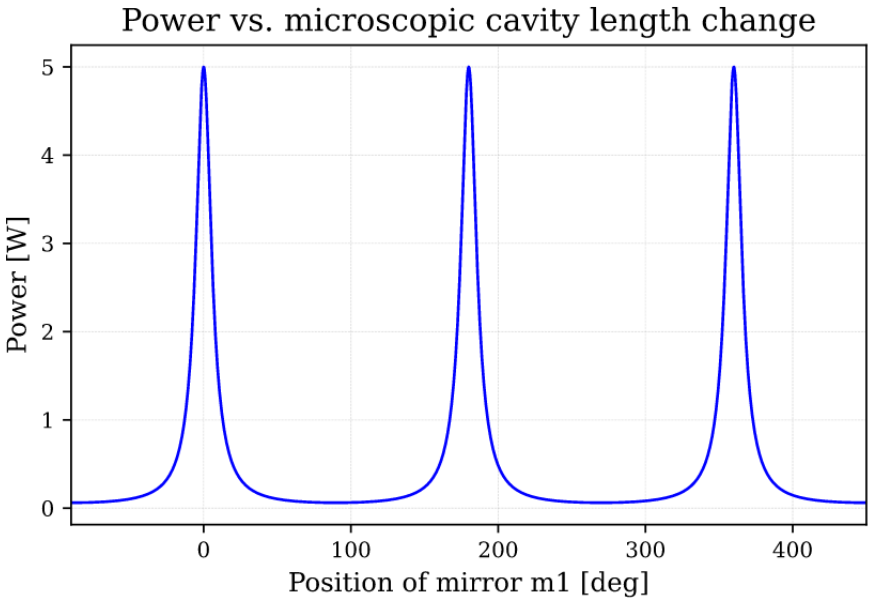

FIGURE 2.6: Power in the cavity vs. ϕ, showing resonance at 0°, 180° and 360°.

A measure of how precise this resonance peak is, is called the *finesse* of the cavity. Higher finesse means narrower resonance, i.e. if the frequency is closer to the true resonance-frequency stronger power-amplification will occur. Translated into the changing of mirror position, this means if the round-trip length is very close to an integer number of wavelengths, the power-amplification can be very high [7, Chpt. 11]. The finesse of a cavity can be calculated with the full spectral range (FSR) and the full-width half maximum (FWHM) or the reflectances of the cavity using the equation from [8, Chpt. 5]. The reflection coefficient $r = \sqrt{R}$ is introduced here as well

$$F = \frac{\text{FSR}}{\text{FWHM}} = \frac{\pi}{2\arcsin\left(\frac{1-\sqrt{R_1R_2}}{2\sqrt[4]{R_1R_2}}\right)} \approx \frac{\pi\sqrt{r_1r_2}}{1-r_1r_2}. \tag{2.13}$$

When all optical cavities in an interferometer are on resonance, the interferometer is called *locked*.

Transmittance matching

As the previous section implies, choosing the right values of transmittance and reflectance is very important. For m1 and m2 these are called $T1$, $R1$ and $T2$, $R2$ respectively. As stated before, since the signal has to end up in the detector in the south of figure 2.4, mirrors at the end of the cavity will need to have a large reflectance. The cavity therefore operates in the so-called over-coupled regime $T1 > T2$. To see what happens with the reflected and circulating power, an analysis of changing $T1$ can be made. [10]

For $T2 = 0.2$, the changing of $T1$ is simulated in figure 2.7. For $T1 = 0.2$, the same situation is found as in figure 2.6 for ϕ in resonance. When both transmittances are equal, the system is in impedance-matched regime. One can see that in this case, no power seems to be reflected on the first mirror. This is paradoxical since $R1 = 0.8$, which implies 80% of the incoming light already gets reflected

back to the laser. The explanation can be found by checking the phase of the reflected and circulating signal. Passing through a mirror results in a phase shift of 90° (in the convention of this programming language). Assuming the cavity is in resonance, a round trip will add no net phase for any number of cycles in the cavity. Light from the cavity that leaks out of the cavity (adding a phase shift of 90° again) will therefore have a phase difference of 180° w.r.t. the directly reflected light. The laser is set to have a power of 1 W, which is why at $T1 = 0.2$ the directly reflected light will have an amplitude of 0.8 W. The light in the cavity reaches 5 W due to the amplification effect. Imagine now the 5 W beam bouncing at m2 and returning (4 W left). Of this resulting beam, $4\ W \cdot 0.2 = 0.8\ W$ will also go into the detector for reflected light, but with a phase difference of 180°. This is why, due to interference, the total reflected light will have a net power of 0 W. Having no light for interference measurements is not practical of course, which is why an over-coupled regime is chosen. In this case, the power of the circulating light will be slightly lower but there will also be slightly less directly reflected light. The circulating light 'wins' and the net observed light will have the phase difference of 180° w.r.t. the light that was sent in. Most importantly though, this light will have travelled a much larger distance than the directly reflected light and will be highly sensitive to gravitational waves.

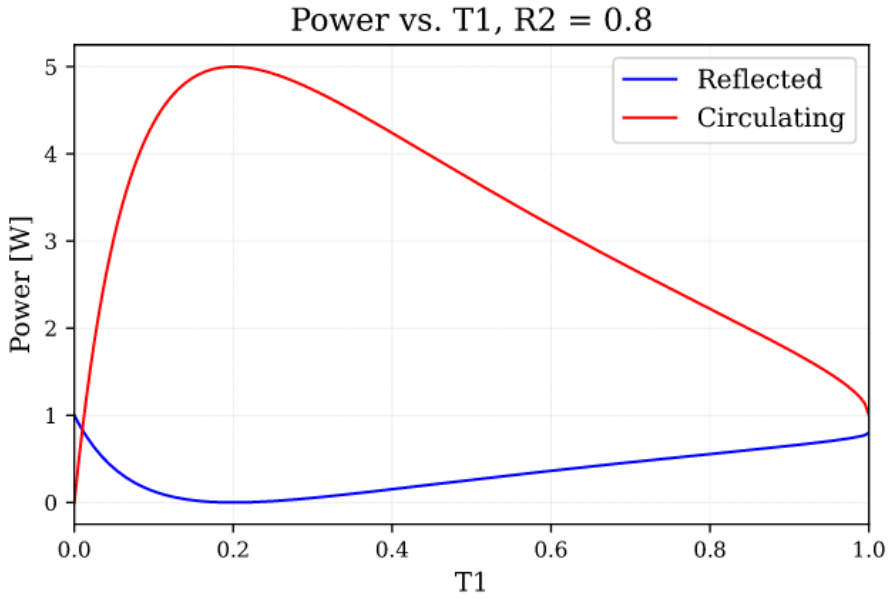

FIGURE 2.7: Power reflected/circulating in the cavity vs. $T1$.

The amount of light coming back from the cavity can be calculated through the effective reflection coefficient of the cavity. The formula adapted from [8, Chpt. 2] is

$$\begin{aligned} r_c(\phi) &= r_{IM} - \frac{r_{EM} t_{IM}^2}{\exp(-2i\phi) - r_{IM} r_{EM}}, \\ &= \frac{r_{IM} - r_{EM} \exp(2i\phi)}{1 - r_{IM} r_{EM} \exp(2i\phi)}. \end{aligned} \tag{2.14}$$

Here ϕ refers to the microscopic tuning of the cavity end mirror. For an impedance-matched cavity with reflection coefficient r on resonance one can see that

$$\frac{r_{EM}t_{IM}^2}{\exp(-2i\phi) - r_{IM}r_{EM}} = \frac{r(1-r^2)}{1-r^2} = r$$
$$\implies r_c(0) = 0,$$

as was also shown above.

After having discussed this theory, it is interesting to see which values were actually picked in the ETpf simulations. The values used are $T1 \approx 0.003$ and $T2 \approx 6.4 \times 10^{-6} \approx 0$. Both mirrors also have some loss $L_1 = L_2 = 5 \times 10^{-5}$ that is included as $R + T + L = 1$. The finesse of such a cavity is $F \approx 2020$. These values generate a very large power amplification effect inside the cavities. This means the de facto laser power is much higher than the initial laser output and thus decreasing the shot-noise in the results (see sec. 2.5.1). The light travels, on average, a much higher distance than a single round-trip.

2.2.3 Phase modulation and demodulation

Modulation

A representation of signal modulation can be seen in figure 2.8. In this work exclusively phase-modulation will be used, where a time-dependent phase is added to the carrier signal of the laser. The derivation below is based on the one found in [5, Chpt. 3]. Only the time-dependent part of the light field is considered, which reads

$$A(t) = A_0 \exp(i\omega_0 t), \tag{2.15}$$

with ω_0 the carrier angular frequency. After phase modulation this becomes

$$A(t) = A_0 \exp(i(\omega_0 t + m\cos(\Omega t))), \tag{2.16}$$

where m is the modulation index and Ω the modulation frequency. The standard modulation index that is used in this work is 0.1. After modulation the wave will not only contain its carrier frequency (for ETpf $f_0 = \frac{\omega_0}{2\pi} \approx 200$ THz) but also various sidebands starting at $f_0 \pm \frac{\Omega}{2\pi}$ and getting weaker with every higher order of Ω. This can be seen by expanding the second part of the expression above using the identity

$$\exp(iz\cos\varphi) = \sum_{n=-\infty}^{\infty} i^n J_n(z)\exp(in\varphi), \tag{2.17}$$

where J_n refers to the Bessel functions of the first kind. Therefore eq. 2.16 becomes

$$A(t) = A_0 \exp(i\omega_0 t) \sum_{n=-\infty}^{\infty} i^n J_n(m)\exp(in\Omega t) \tag{2.18}$$

$$= A_0 \sum_{n=-\infty}^{\infty} i^n J_n(m)\exp(i(\omega_0 + n\Omega)t). \tag{2.19}$$

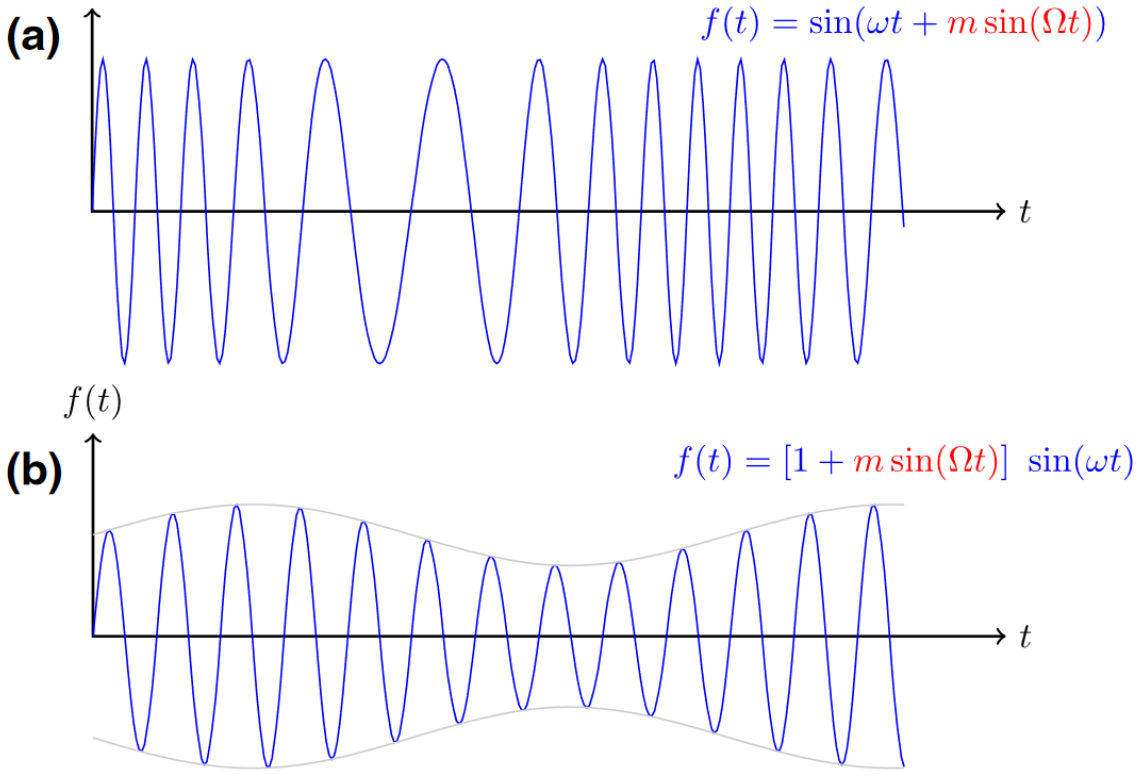

FIGURE 2.8: (a) Phase-modulated sine wave, (b) amplitude-modulated sine wave [8, Chpt. 3] .

For small m the values of the Bessel functions will become smaller for higher orders of n. This means the sum will converge and an approximation for small n can be made. There holds

$$J_n(m) = \left(\frac{m}{2}\right)^n \sum_{p=0}^{\infty} \frac{\left(-\frac{m^2}{4}\right)^p}{p!(n+p)!} = \frac{1}{n!}\left(\frac{m}{2}\right)^n + O\left(m^{n+2}\right), \tag{2.20}$$

and

$$J_{-n}(m) = (-1)^n J_n(m). \tag{2.21}$$

Writing out eq. 2.19 up to m^2 results in

$$\begin{aligned} A(t) = A_0 \exp(i\omega_0 t)\Bigg[1 - \frac{m^2}{4} + i\exp(i\Omega t)\frac{m}{2} + i\exp(-i\Omega t)\frac{m}{2} \\ - \exp(2i\Omega t)\frac{m^2}{8} - \exp(-2i\Omega t)\frac{m^2}{8}\Bigg] \end{aligned} \tag{2.22}$$

$$= A_0 \exp(i\omega_0 t)\left[1 - \frac{m^2}{4} + i\, m\cos(\Omega t) - \frac{m^2}{4}\cos(2\Omega t)\right]. \tag{2.23}$$

This shows the amplitude of the carrier has decreased by $-\frac{m^2}{4}$ and sidebands have appeared at $\omega_0 \pm \Omega$ and $\omega_0 \pm 2\Omega$. Of course even higher orders are present in progressively smaller amplitudes, as represented in fig. 2.9. This is highly useful since the interferometer is resonant for the carrier frequency but not necessarily for the sidebands, which will therefore have different behaviour. This provides

more information on for example mirror positions in the interferometer [8, Chpt. 3]. For ETpf several useful modulation frequencies have been determined in previous work. A determining factor is that the frequency should be as far as possible from resonances of higher order modes of the carrier signal. This is illustrated in fig. 2.10. The resulting frequencies are $f_1 = \frac{\Omega}{2\pi} = 12.319743$ MHz ≈ 12.3 MHz and secondarily $f_2 \approx 6.13$ MHz. These correspond to wavelengths of 24.4m and 48.9 m. Unless explicitly stated only the first modulation frequency is used. These are sufficiently far from resonances of the cavity for them to be considered anti-resonant. The result is that the sidebands are reflected by the cavity with no amplification. [11]

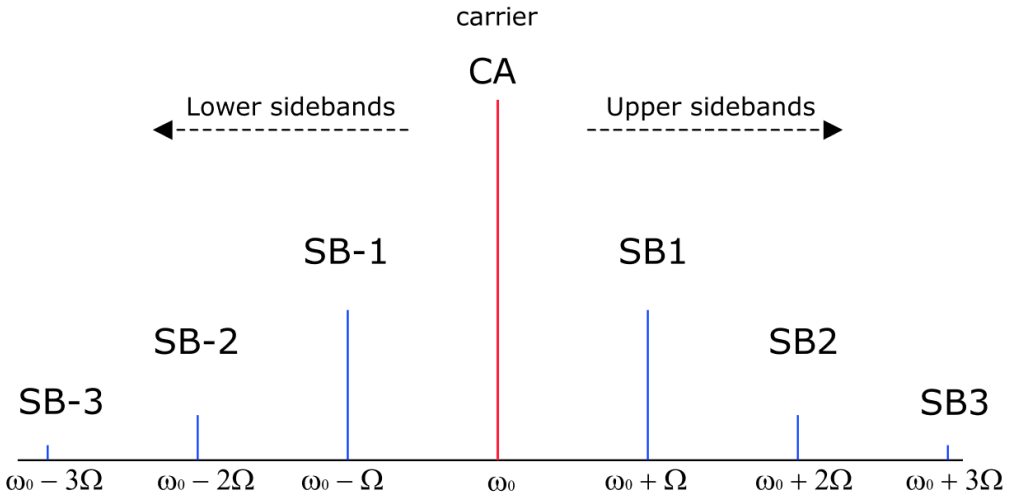

FIGURE 2.9: Illustration of carrier and sidebands. ω_0 is the carrier angular frequency, Ω is the sideband angular frequency [12].

The Schnupp modulation scheme

At this point it is useful to see how modulation would be implemented at ETpf (and similar experiments). The technique used is called Schnupp or frontal modulation, which was developed by dr. Lise Schnupp as a new scheme to allow the modulated signal to reach the output port. In general, since the wavelength of the modulation is orders of magnitude bigger than the carrier wavelength, the modulation will not be sensitive to the microscopic tuning of the end mirrors. In fact, the sidebands are basically reflected by the cavity due to being anti-resonant. This means if Michelson arm-lengths[2] are equal, no modulation will reach the output port. To solve this, an asymmetry $\Delta L = 10$ cm is added between the BS and the EMX (relative to the y-arm). Microscopically the tuning is still set at a multiple of the carrier wavelength, meaning the same interference conditions hold for the carrier. The sidebands can now however reach the output port since they will no longer completely destructively interfere. [8, Chpt. 8]

The exact proportion of light that reaches the output port is calculated in [13, Chpt. 1.3] and also in chapter 3. This calculation is done for an ITF without arm cavities. The result for the first sideband

[2]The Michelson arms are defined from the BS to the IM, therefore excluding the arm cavities.

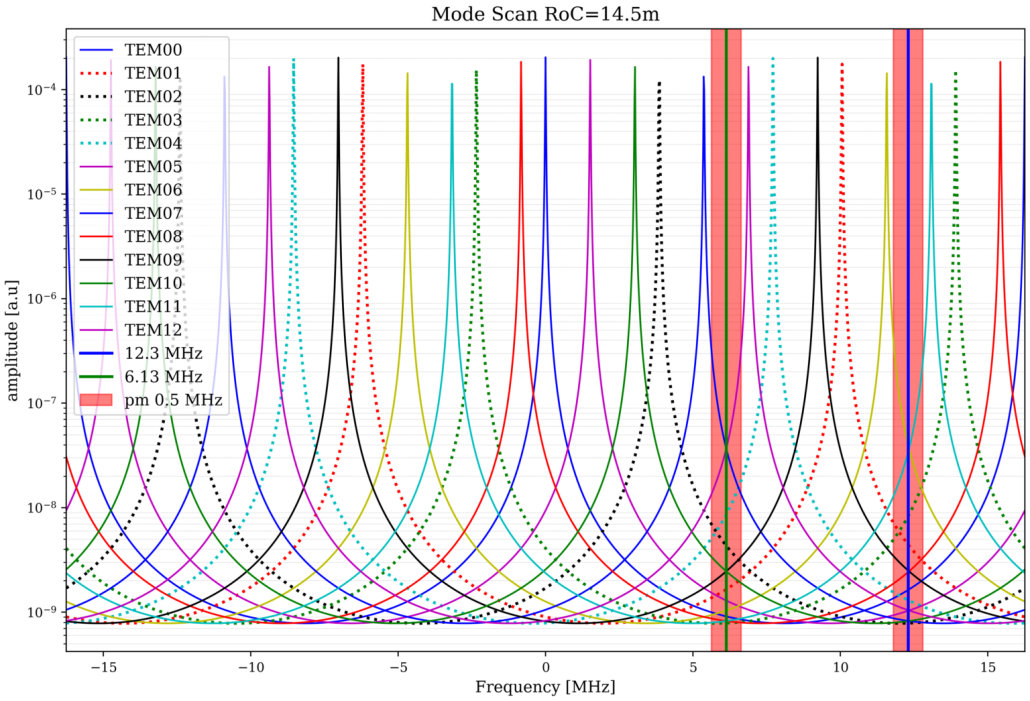

FIGURE 2.10: Higher-order mode scan of the arm cavities to identify modulation frequency candidates of the interferometer [11].

frequency is shown here for reference, with ϕ the phase difference of the two arms.

$$I \propto -2J_0(m)J_1(m)\sin\left(\frac{\Omega\Delta L}{c}\right)\sin(\phi) \approx -m\sin\left(\frac{\Omega\Delta L}{c}\right)\sin(\phi) \tag{2.24}$$

$$\approx -m\sin\left(\frac{\Omega\Delta L}{c}\right)\phi. \tag{2.25}$$

For $f_1 = 12.3$ MHz and $\Delta L = 10$ cm the following value is found

$$m_{\text{eff}} = m\sin\frac{\Omega\Delta L}{c} \approx 0.02578 \cdot m. \tag{2.26}$$

This means 2.6% of the input modulated light power reaches the output port. This is only a small fraction, but it significantly differs from zero. Therefore, when the ITF deviates from the dark fringe now also the sidebands will show up at the output port, which can then be used to control the ITF or be used as an optical beat for measuring a GW. The validity of eq. 2.24 is confirmed by a FINESSE simulation of the ITF without arm cavities, the result is shown in fig. 2.11. More information about FINESSE can be found in section 2.6. The theoretical linear approximation is also plotted for comparison. The portion of modulated light reaching the output port could be increased by increasing the Schnupp asymmetry. This would however also increase the amount of noise in the signal at that port which will be discussed in more detail in chapter 4. An optimal length could be found through balancing these two effects, but 10 cm is a good (although maybe temporary) value that is in the same order of magnitude as used in similar experiments.

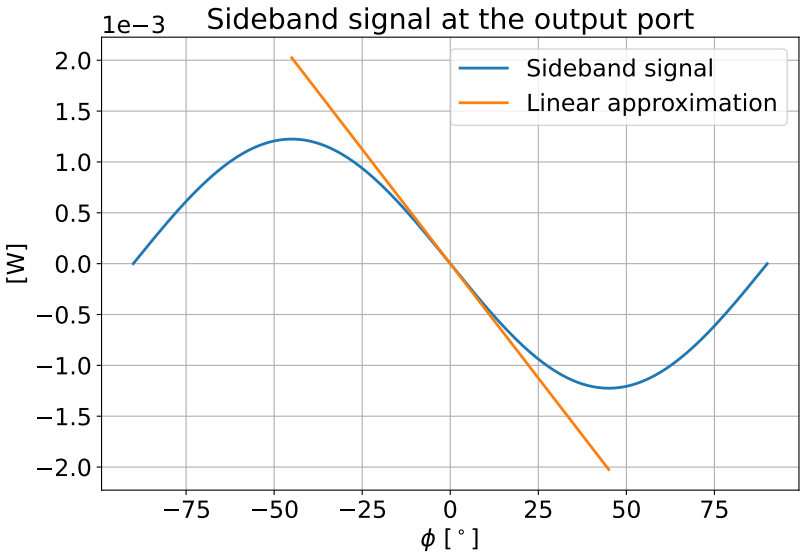

FIGURE 2.11: Simulated sideband signal at the output port for a Schnupp asymmetry of $\Delta L = 10$ and modulation index of $m = 0.1$. The linear approximation of eq. 2.25 is also shown. This plot is made without DC offset (see sec. 2.4).

Demodulation

As stated earlier, when travelling through the interferometer the amplitudes of the different frequency components will evolve separately. The one corresponding to the carrier for example will be amplified by the arm cavities. However, the interferometer is set to the dark fringe only for the carrier. The specific way in which this is done is discussed later. Sidebands will therefore "leak" through to the dark port, allowing them to be measured there. This provides a tool to monitor mirror positions for example. In this section the extraction of sideband information will be discussed, based on [13, Chpt. 1.4]. At the output ports all amplitudes will have a different amplitude than right after modulation, so the light field can be represented by

$$A(t) = \exp(i\omega_0 t)\left[a_0 + a_+ \exp(i\Omega t) + a_- \exp(-i\Omega t)\right]. \tag{2.27}$$

Here only frequency components up to first order in m are shown, but the treatment can be expanded for higher orders. The goal is however to show that even for expansion until the first order, a signal with a frequency of 2Ω will still be measured. The measured signal will be proportional to the square of the field amplitude, i.e.

$$\begin{aligned} I &\propto |A(t)|^2 \\ &= |a_0|^2 + |a_+|^2 + |a_-|^2 + (a_0 a_+^* + a_0^* a_-)\exp(-i\Omega t) + (a_0^* a_+ + a_0 a_-^*)\exp(i\Omega t) \\ &\quad + a_+ a_-^* \exp(2i\Omega t) + a_+^* a_- \exp(-2i\Omega t). \end{aligned} \tag{2.28}$$

So notably a signal at double the modulation frequency is present when only performing the calculation up to the first order of m.

Now it is of interest to see how the information contained in these amplitudes can be extracted. In

simulations this is as simple as defining a photodetector with a demodulation frequency and phase, which will return the amplitude of the photocurrent at that frequency. The mathematical description of this is based on [5, Chpt. 4]. The given frequency ω_d and phase ϕ_d define a local oscillator $\cos(\omega_d t + \phi_d)$ that is multiplied with the signal at the detector. Starting with a field amplitude of

$$A(t) = \sum_{i=0}^{N} a_i e^{i\omega_i t}, \tag{2.29}$$

the signal becomes proportional to

$$S_0 = E \cdot E^* = \sum_{i=0}^{N} \sum_{j=0}^{N} a_i a_j^* e^{i(\omega_i - \omega_j)t}. \tag{2.30}$$

After multiplication with the local oscillator this becomes

$$S_1 = E \cdot E^* = \sum_{i=0}^{N} \sum_{j=0}^{N} a_i a_j^* e^{i(\omega_i - \omega_j)t} \frac{1}{2} \left(e^{i(\omega_d t + \phi_d)} + e^{-i(\omega_d t + \phi_d)} \right). \tag{2.31}$$

Now the DC component of this new signal is measured. This filters out the elements of the sum where $\omega_i - \omega_j = \pm\omega_d$.

$$S_{1,DC} = \frac{1}{2} \left(\sum_{(i,j)\in A} a_i a_j^* e^{-i\phi_d} + \sum_{(i,j)\in A} a_j a_i^* e^{i\phi_d} \right) \tag{2.32}$$

$$\text{with } A = \left\{ (i,j) \mid i,j \in \{0,\ldots,N\} \wedge \omega_i - \omega_j = \omega_d \right\}$$

$$= \sum_{ij\in A} \Re \left\{ a_i a_j^* e^{-i\phi_d} \right\}. \tag{2.33}$$

Depending on ϕ_d two different (orthogonal) measurements can be made to extract all information in the $a_i a_j^*$ terms. The in-phase measurement theoretically has $\phi_d = 0$ and the quadrature-phase measurement uses $\phi_d = \pi/2$. In simulation/measurement the phases are rather arbitrary, and therefore the in-phase component is often defined at the phase with the strongest signal. This is further discussed in the chapter on longitudinal control (chpt. 3). The quadrature-phase is always the 'in-phase' phase plus 90°.

2.3 Einstein telescope

ETpathfinder is designed as a test-bench for the Einstein Telescope and other future detectors. The goal is to keep updating the pathfinder so that it is always performing experiments for the next generation of detectors. As stated earlier, the current detectors are in the second generation. ETpf will perform tests for the third generation, in which ET will be a significant contributor. Before discussing the specifics of the ETpf project, the goals of ET should therefore be outlined instead. That way it will be clear what direction the GW-field is headed and why ETpf was brought to life.

ET is designed to have at least two interferometers, of which one is optimised for low-frequency

signals (LF) and one for high-frequencies (HF). There might be three of these couples implemented to be overlapping in the novel triangular shape shown in figure 2.12. There is however not yet a complete consensus on the final shape, as the different interferometers might end up being built at separate locations. The major ways ET will differ from and improve upon previous detectors are listed below and are based on [4, Chpt. 6], [14, Chpt. 1] and [8, Chpt. 6].

- Firstly, **cryogenic temperatures** will be implemented for the most important TMs. This technology is already being applied by KAGRA and will be tested for ET at ETpf. Cooling the mirrors reduces thermal effects such as thermal lensing that occurs due to the laser heating the TM. This forms an important source of noise in the LF regime, which ET will attempt to mitigate.
- Furthermore, the mirrors will be made of a new material, namely **silicon** as opposed to fused silica (AdV & ALigo) or sapphire (KAGRA). Fused silica is unfortunately not suitable for use at very low temperatures, as its mechanical quality drops significantly. Sapphire is less abundant and harder to polish than silicon, making it slightly less attractive for ET. The transition to silicon will involve many changes in aspects such as polishing and coating as well as differences for the mechanical implementation. The LF detector will run at 10-20 K using silicon TMs, while the HF detector will operate at room temperature with fused silica.
- This new material has different optical properties and requires the use of **longer wavelengths** to reduce absorption in the mirror material. ETpf will perform experiments for wavelengths of 1550 nm and 2 μm as opposed to the 1064 nm of 2G. This also implies some changes for all other optical components of the detector such as the laser itself, photodetectors, modulators etc.
- A final noteworthy area of improvement for 3G is that of quantum noise (QN) mitigation, see sec. 2.5.1 for an explanation. ETpf will experiment with **advanced quantum noise reduction techniques** to maximally improve the system's precision. These could then also be utilised for ET at a later stage.

The question of why these improvements are necessary arises since 2G detectors are currently operational and making weekly detections. Rather than only making frequent detections, ET aims to serve the function of an *observatory* as the whole sector enters the age of GW astronomy. The signals and their sources should be reconstructed with a much higher precision to reach the scientific goals that were mentioned in section 2.1. This requires higher sensitivity and signal-to-noise ratios (SNR). Attempts could be made to improve the currently existing infrastructures. This would however necessitate a complete overhaul as well as long downtimes. All the while improvements are constrained by the pre-existing conditions of the infrastructure. This makes the idea of a new site a lot more attractive. [4, Chpt. 1]

ET aspires to make in the order of 10^5-10^6 BBH coalescence observations per year, up to a redshift distance of $z \sim 20$, and even higher for some mass-combinations. This includes some of the time-period before star formation, which allows for detection of primordial BHs. For comparison, 2G detectors might soon reach a distance of $z \simeq 1$. Not only in distance, but also a wider region in mass will become explorable. ET will be able to 'see' the lightest and heaviest of BHs. Similar improvements will apply to BNS detections, increasing the detection rate to 6×10^4 per year up to $z \simeq 2-3$. The high-frequency precision of ET will allow detection of the merger phase of BNS that is

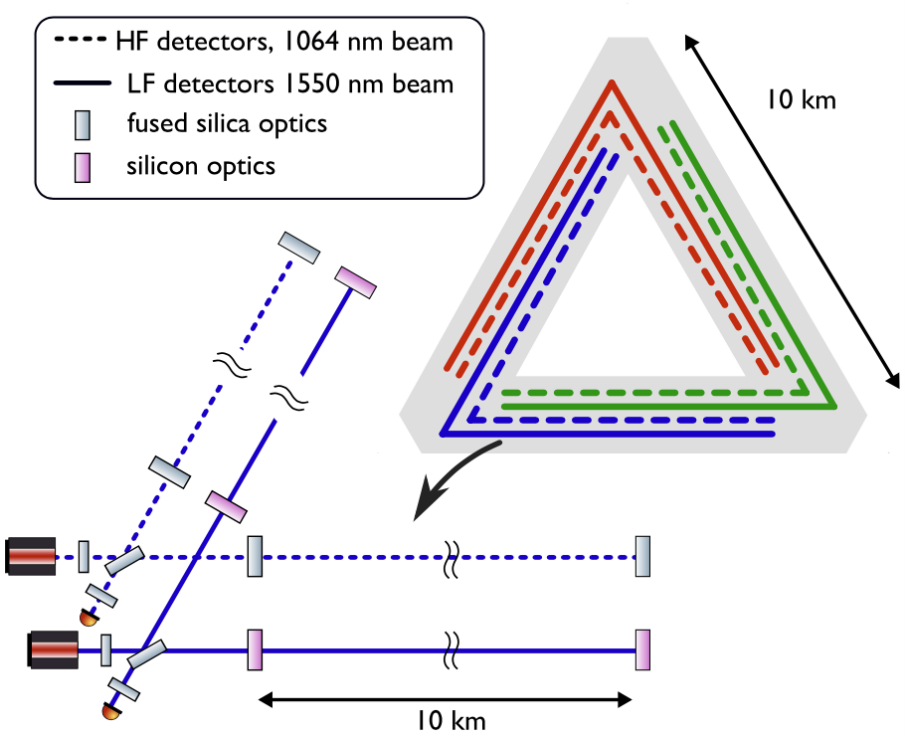

FIGURE 2.12: General overview of the ET layout, with 3 detectors forming a equilateral triangle of 10 km length. Bottom left is a sketch that shows that each detector consists of two interferometers, one optimised for LF and one for HF [15, Chpt. 1].

currently not visible. The observatory further aims to detect new sources such as supernovae collapse or continuous GW from isolated pulsars. [4, Chpt. 1-2]

2.4 The Einstein Telescope pathfinder and its layout

It is clear that a lot of modern technologies will be implemented at ET. Hence there is a very good motivation for building the Einstein Telescope pathfinder (ETpf) as an R&D facility to acquire the experience necessary before applying them at the large scale. ETpf is based at Maastricht University and focuses on studying these new methods to prepare for future GW detectors. The project is only dedicated to development rather than actually detecting gravitational waves.

The optical layout of ETpf will differ slightly from other detectors. It is shown in figure 2.13, real-life pictures can be found in chpt. B. Since ETpf will not be large enough to make any GW detections, the two beams that are formed by the BS will be sent into the same arm. This simplifies the situation and allows measurements to be made with less towers operational. The two beams will also share some of the optics, thus lowering the total cost and allowing for the other arm to perform an independent experiment with different optics, temperatures and wavelength. The wavelengths used are 1550 nm ($\sim$ 200 THz) and 2 μm ($\sim$ 150 THz) and both have their challenges and advantages. In this work only the 1550 nm beam is discussed, although most concepts and simulations could easily be applied to the other beam as well. Two beams of the same wavelength will still be referred to as the x- and

y-beam or -arm even though they are travelling parallel to each other in the same physical arm. [14, Chpt. 6]

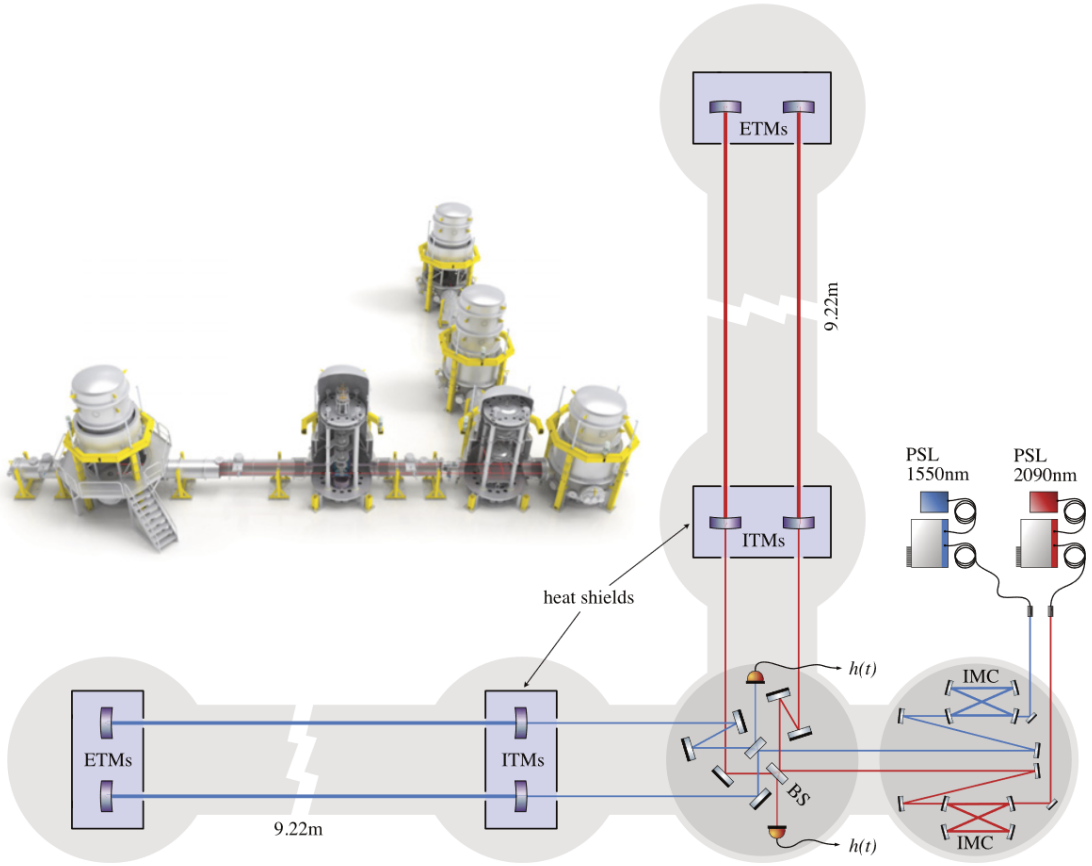

FIGURE 2.13: Layout of the first phase of ETpf. The blue beam represents 1550 nm and the red beam 2 μm [14, Chpt. 2].

ETpf will feature input mode cleaners (IMC) for each beam, which can filter unwanted modes and help stabilise the laser frequency. Output mode cleaners (OMC) will have a similar function for filtering the outgoing signal. The positions of the OMC mirrors are locked to the laser frequency instead of the other way around. Currently there is no power- or signal recycling stage planned. [14, Chpt. 7]

Folding mirrors (FMs) or steering mirrors are used to aim the beam right before entering the cavity and will be slightly transmissive so the light that passes through can be used for control of the cavity. In figure 2.13 they can be found between the beamsplitter and ITMs. Their transmittance is expected to be around $T = 0.005$ or 0.5%. The y-beam of each arm can be steered using only one FM. The x-beam however will have two such mirrors, creating an asymmetry between the two arms. This is more clear in figure 2.14. The influence of this difference will be discussed in later chapters.

In figure 2.14 the beam comes in from the left. There it passes through the electro-optic modulator (EOM) where the signal becomes modulated. The next important component is the beamsplitter which divides the beam in two equal parts. As stated earlier, the interferometer is operated on the dark fringe. When all mirrors are in their resting position the beams destructively interfere at the output port, which is the southern side in fig. 2.14. The output port is also referred to as the asymmetric port,

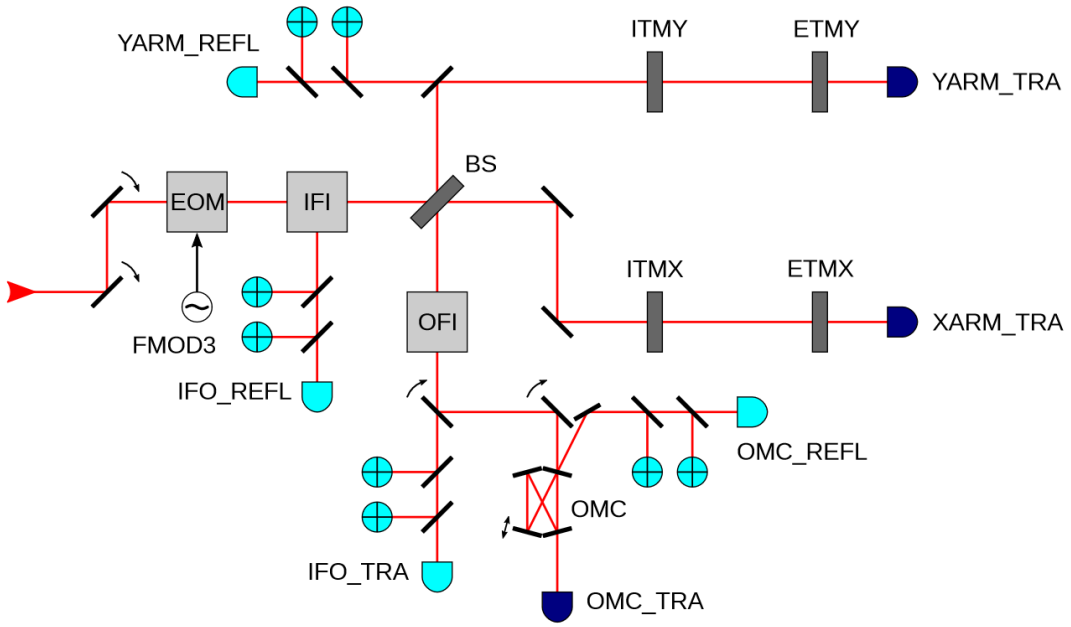

FIGURE 2.14: Control scheme and sensor setup for one ETpf beam. All photodiodes in dark blue are for DC monitoring only, while those in light blue are demodulated [14, Chpt. 7] .

or by the name of its node in the FINESSE simulations: 'nout'. For simplicity the simulations will neither contain all optics at the output port, nor an OMC. Any detectors will simply be placed some distance from the BS without any other preceding reflections. The input port of the BS is also called the reflected port and goes by the name 'nBSin'. The interferometer is operated at a slight offset from the dark fringe for practical reasons that are treated in sec. 3.2.6. This means the BS is moved by 2.114° towards the x-arm. This so-called DC offset or Michelson offset allows a base amount of carrier light to reach the detector at the operating point. The amount of light should still be kept low, as high-efficiency and low-noise photodiodes can often not detect large photocurrents. It is important to note this offset influences all signals and sidebands. This contrasts with the Schnupp asymmetry, treated in section 2.2.3. A path length of 10 cm is added between the BS and the ITMX, causing an asymmetry relative to the y-arm. [8, Chpt. 8] [14, Chpt. 7]

Going north from the BS, the light reaches the folding mirror and enters the cavity. The light returning from the cavity hits the same FM and a fraction of it passes through to reach a control sensor behind the FM. This sensor is named 'YARM_REFL' in the figure and 'pd_FMAy' at node 'nFMAyOut' in FINESSE. A similar simulated sensor 'pd_FMx' is placed behind the FM closest to ITMX in node 'nFMAxOut2'. [14, Chpt. 7]

2.5 Noise budgets

Several mentions have already been made about reducing noise for more precise detections. This allows an increase in signal-to-noise ratio SNR which is of the highest importance when making observations with high confidence. This section will go into detail about the different kinds of relevant

noises and how to interpret noise budget curves such as the ones shown in fig. 2.15 and 2.16. The first displays the projected noise budgets for the two ET ITFs, the second shows the noise budget for ETpf.

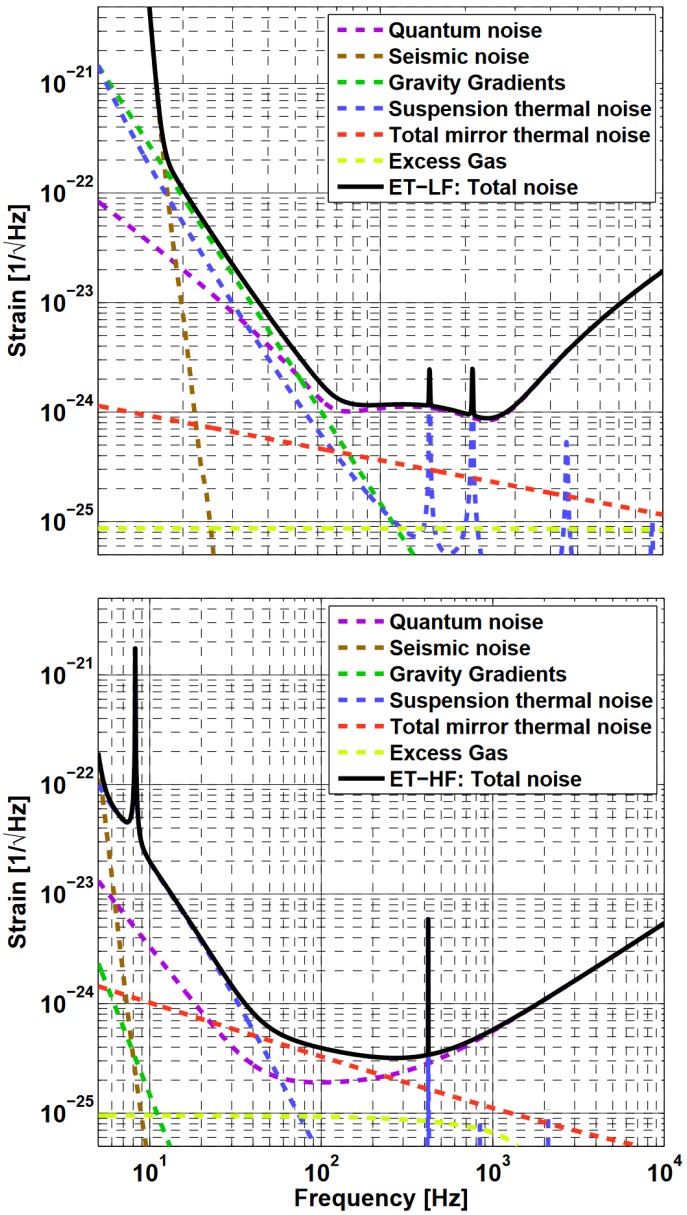

FIGURE 2.15: Projected noise budget for the low-frequency (top) and high-frequency (bottom) interferometer of ET. The total noise is based on a quadratic sum of all noise sources due to them being statistically independent [4, Chpt. 1].

2.5.1 Low frequency noise sources

The most relevant sources of noise in the LF regime are seismic noise, gravity gradients and quantum noise. As stated earlier the LF interferometer has less problems with thermal effects due to the very low temperature it is operated at.

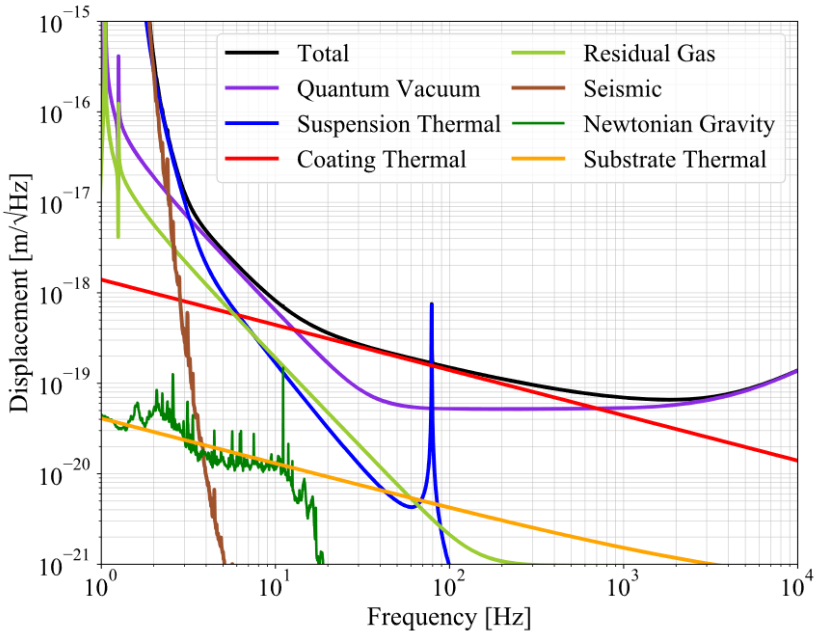

FIGURE 2.16: Projected noise budget for ETpf operating with a 1550 nm carrier wavelength at 18 K [16, Chpt. 3].

Seismic noise

Seismic noise refers to noise stemming from movements and vibrations of the Earth around the detector. Such vibrations include fast-changing antropogenic sources as well as the hour-long period of the Earth's tide motion. ET draws inspiration from the passive stabilisation techniques implemented at Virgo. The process by which mode-frequencies of the mirror suspension are intentionally kept very low is called attenuation. The most important optics will be suspended using a six-stage pendulum system termed the Superattenuator (see fig. 2.17). These pendula aim to dampen any movements and vibrations. This pendulum chain itself hangs from an inverted pendulum at the top, upon which actuators can actively correct for movements. By doing so, the TMs act very close to a test particle whose motion is only influenced by a passing GW. Similar attenuators will be implemented at ETpf as well, which will be hosted in the towers shown for example in figure B.2. [16, Chpt. 3] [4, Chpt. 1, 6]

Newtonian noise

Gravity gradients originating from direct gravitational interactions between the surrounding soil and the mirrors also provide a source of noise. These gradients are not always constant; a dominant contribution is caused by seismic movements of the Earth mentioned in the previous paragraph. This effect can however not be isolated from the mirrors since it is a direct interaction between mirror and soil. ET attempts to mitigate its influence by constructing the observatory 200-300 m underground, in a geographical region where less seismic motion is present and the soil is relatively homogeneous. This also reduces antropogenic seismic noise. The two candidate regions that fit the requirements are located in the Euregio Meuse-Rhine and in Sardinia. [16, Chpt. 3] [4, Chpt. 1, 7]

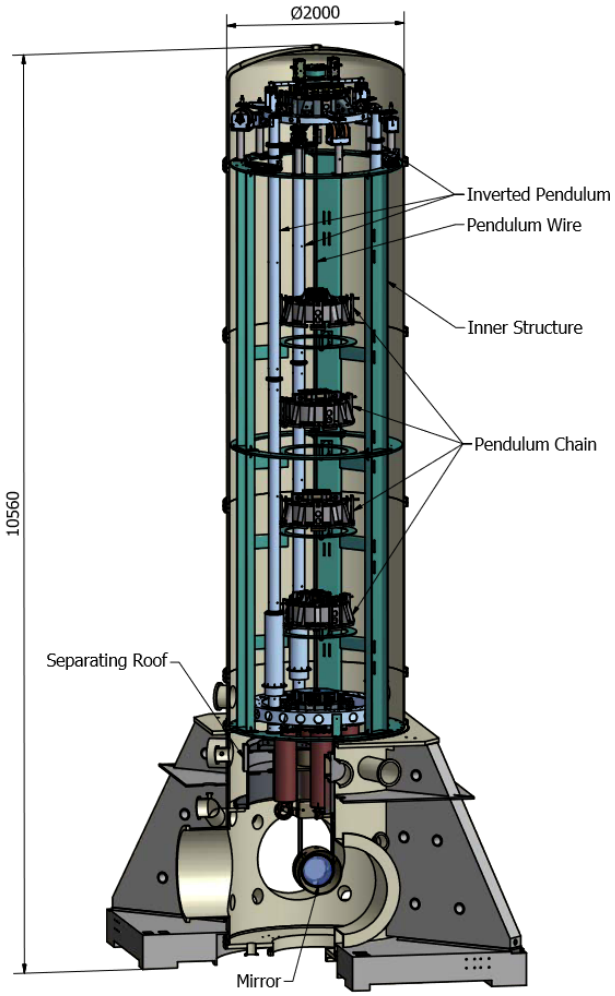

FIGURE 2.17: Schematic view of a Virgo Superattenuator, similar to the ones proposed for ET [4, Chpt. 1].

Quantum noise

Quantum noise can be understood as a result of the Heisenberg uncertainty principle associated with the amplitude and phase of the light field. Since they are an observable conjugate pair, their uncertainties can be minimised but will never become zero. What is left after minimisation is called the vacuum noise. There are two types of quantum noise: shot-noise and radiation pressure noise. One can not minimise both at the same time. The former is most important in the HF regime and will be discussed in the next subsection. The latter is explained here.

Radiation pressure noise arises from increased laser power, which applies radiation pressure onto the mirrors. Quantum fluctuations in the laser amplitude cause movement of the mirrors, which results in a phase fluctuation of the laser light. The effect is strongest at lower frequencies. This noise is carried all the way to the output port. To decrease the noise smaller fluctuations of light amplitude are necessary, which will unfortunately correspond to bigger phase fluctuations. This can be achieved using a type of *squeezed light*, which are light states with correlations between the phase

and amplitude. A state is first prepared with lower phase fluctuations, which is then sent through a filter cavity. After this it possesses the desired property of minimal amplitude fluctuations and higher phase uncertainty. Amplitude fluctuations are also decreased by using heavier TMs. [8, Chpt. 6] [16, Chpt. 3] [4, Chpt. 1]

2.5.2 High frequency noise sources

For the HF regime the most relevant noise sources include shot-noise, but also thermal noise which entails noise from the suspension and from the mirrors/coatings itself. [4, Chpt. 6]

Thermal noise

Suspension thermal noise can either come from mechanical losses on the surface of the suspension, losses at the attachment with the TM or thermoelastic noise from statistical temperature fluctuations. The first two are caused by the Brownian motion of the particles at the surface. This motion undergoes internal or molecular friction, which introduces losses, causing kinetic energy to be converted to heat. Localised heat sources cause thermal lensing effects for the laser hitting the mirror that therefore introduce noise. These thermal noise sources are well studied in other GW detectors and can be mitigated sufficiently for ET. For the LF detector suspension thermal noise is reduced significantly by the cryogenic cooling and the use of silicon. [4, Chpt. 6] [17, Chpt. 2]

Coating thermal noise can arise from the Brownian motion of the coating material or from thermoelastic effects. One way of reducing coating noise is by increasing the size of the optics and therefore the laser spot size, thus reducing the thermal gradient within the mirror and also the relative effect of the Brownian motion in the coating. Fused silica is known to have very low mirror thermal noise, which is why it's chosen for the HF detector. In general, the coating of a mirror needs to have low mechanical loss and thickness. Since a lot of progress has been made in almost all aspects of coatings, it is expected that for most frequencies quantum noise will form the dominant challenge. ETpf will be experimenting with coatings for silicon that haven't been researched as much as those for fused silica. [4, Chpt. 6]

Quantum noise

Shot-noise is associated with the statistical nature of the release of electrons in a photodetector. This is non-deterministic and the number of captured photons will always have some spread, which is seen as noise in the results. Its effect is most dominant in the HF regime. The sensitivity w.r.t. shot-noise improves with the square root of the cavity power, and is thus mitigated by using cavities with higher finesse. Shot-noise can also be reduced by applying squeezed-light techniques. To reduce shot-noise, states are chosen with lower phase fluctuations at the cost of higher amplitude fluctuations. [8, Chpt. 6] [16, Chpt. 3] [4, Chpt. 1]

Shot-noise is thus dominant in the HF regime, while radiation pressure noise is dominant for LF. This is a big argument for the separate LF and HF interferometers. The LF interferometer runs at cryogenic temperatures with low arm cavity power ($\sim$ 18 kW) and will use squeezed light for minimal amplitude fluctuations and thus minimal radiation pressure noise. The HF interferometer however runs at much higher power ($\sim$ 3 MW) to reduce phase fluctuations and thus shot-noise. As stated earlier ETpf will already test systems to reduce either type as much as possible. In theory, by combining the results from the two interferometers a much wider frequency spectrum is optimised for quantum noise, allowing for more precise measurement, see fig. 2.18. [4, Chpt. 1] [14, Chpt. 1]

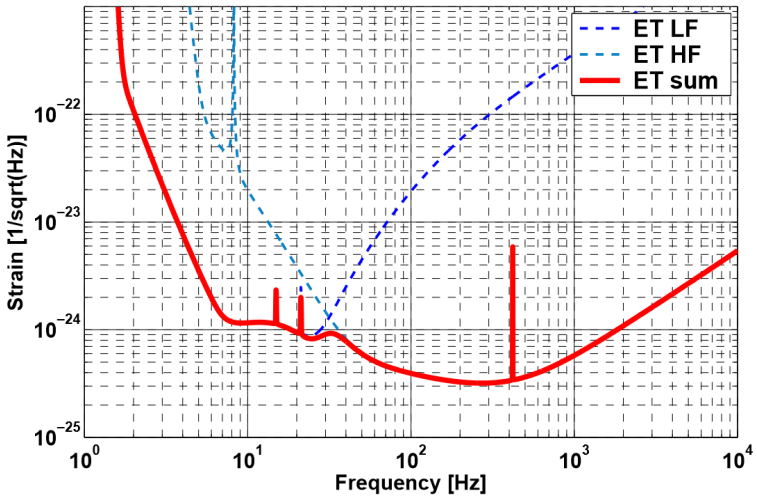

FIGURE 2.18: Quantum noise budget for LF and HF interferometers, as well as the combined results for ET [4, Chpt. 1].

2.6 The FINESSE simulation software

Finally, before any results can be treated a brief introduction to the FINESSE software should be provided. FINESSE was used for all simulated results in this thesis. More specifically, the Python interface PyKat was utilised. The information in this section has been adapted from [18]. FINESSE allows the user to specify the geometry of an interferometer consisting of specific components. In this work the following are implemented:

- Lasers, with power, wavelength and shape of the beam set by the user;
- free spaces, with chosen index of refraction;
- mirrors and beam splitters, defined with values of R, T and L and optionally a radius of curvature (ROC);
- modulators to apply modulation to the carrier laser;
- power-/photodetectors (PDs) with an option for defining a demodulation frequency and phase.

Every component occupies one or more nodes of which some of the names were already mentioned in sec. 2.4. The program computes the light field amplitudes at all nodes and can run iterative simulations where one or more parameters will be changed. Such a parameter is then often displayed on the x-axis of a plot. The user decides either to only consider the plane-wave laser mode or consider Hermite-Gauss modes, which includes higher orders. The former is a lot faster, however sometimes a realistic result is only found when using the latter. The highest order under consideration is indicated by the value of 'maxtem'. Unless stated otherwise, this work uses plane-wave calculations. The reason for this is not limited to reducing computation time, but also that ETpf will deploy an IMC and OMC. These are currently not present in the simulated geometry as they are still under development. Simulating without higher orders is therefore relatively close to the real experiment.

FINESSE uses an initial geometry specified in a file called 'ifo.kat', which contains an interferometer layout featuring the most important components of ETpf with the correct dimensions and parameters. Part of the work performed for this thesis was updating this file to include folding mirrors for both arms. The file 'ifo.yaml' goes into more detail about coatings, mirror materials, noise sources, temperatures and much more. The version used in this thesis was updated on 2022-05-13. A GitHub repository containing all scripts used in this thesis is found at `https://gitlab.nikhef.nl/etpathfinder/simulations`.

Chapter 3

Longitudinal control of the interferometer

3.1 Control of the arm cavities

Before the whole interferometer reaches its locked state, the individual arm cavities can be locked first. This will be done using the Pound-Drever-Hall (PDH) technique. According to the technical design report [14, chpt. 7.3], the interferometer will feature at least one photo-detector behind the folding mirror in the y-arm which will be called 'pd_FMAy' in this work. Folding mirrors (FMs) or steering mirrors are used to aim the beam right before entering the cavity and will be slightly transmissive so the light that passes through can be used for control of the cavity. Their transmittance is expected to be around 0.005 or 0.5%. The x-arm will have two such mirrors, creating an asymmetric situation. One can imagine a similar setup in the x-arm, where 'pd_FMAx' is chosen to be located behind the steering mirror closest to the cavity. Locking the y-cavity was already achieved by prof. dr. Hans Van Haevermaet, and in this work the same method is applied to the x-cavity. It is also valuable to compare the effect of having two FMs in one arm vs only one FM, which is what will be done in the following sections.

3.1.1 The PDH technique

The PDH technique uses a modulated signal to detect if the mirrors of the cavity move from their locked position. Ideally an error signal is found where the measured amount of light increases linearly when the mirror moves in one direction and decreases when it moves in another direction. In that case depending on the changes in the amount of light it is immediately clear how to correct the position(s) of the mirror(s). In general, error signals will not be perfectly linear. Optical gain is defined as the derivative of the error signal at the point of zero-displacement. One can often linearise the signal around the zero-point, and the higher the derivative the stronger the reaction of the chosen error signal to any deviation from zero. In other words, a higher optical gain allows the deviation from zero to be determined with higher accuracy [8, Chpt. 8]. The region of linearity for an arm cavity in ETpf is approximately [12, Chpt. 3]

$$|\Delta L| < \frac{\lambda}{4F} \approx 2 \times 10^{-10} m \approx 0.045^{\circ}, \tag{3.1}$$

where F is the finesse of the cavity. In the case of the arm cavities the error signal is the detected signal behind the FM after demodulation with frequency $f_1 \approx 12.3$ MHz. To achieve the clearest possible signal, first the optimal demodulation phase is determined. This is simply done by looping over all phases and choosing the phase with the highest optical gain for each detector. From this point on this is done for every detector with every signal. An example of finding the optimal demodulation phase ϕ_{opt} can be seen in figure 3.1. The signal demodulated at this optimal phase will be referred to as the in-phase (I) measurement (even though it is not really in phase with the modulator). One can define a so-called second quadrature (Q) by demodulating at a phase $\phi_{opt} + 90°$, which produces an orthogonal signal. Keep in mind that these phases depend on the exact positioning of the modulator, photo-detectors and the lengths of cables, making them relatively arbitrary. This is why the optimal demodulation phase is chosen as the in-phase quadrature. [12]

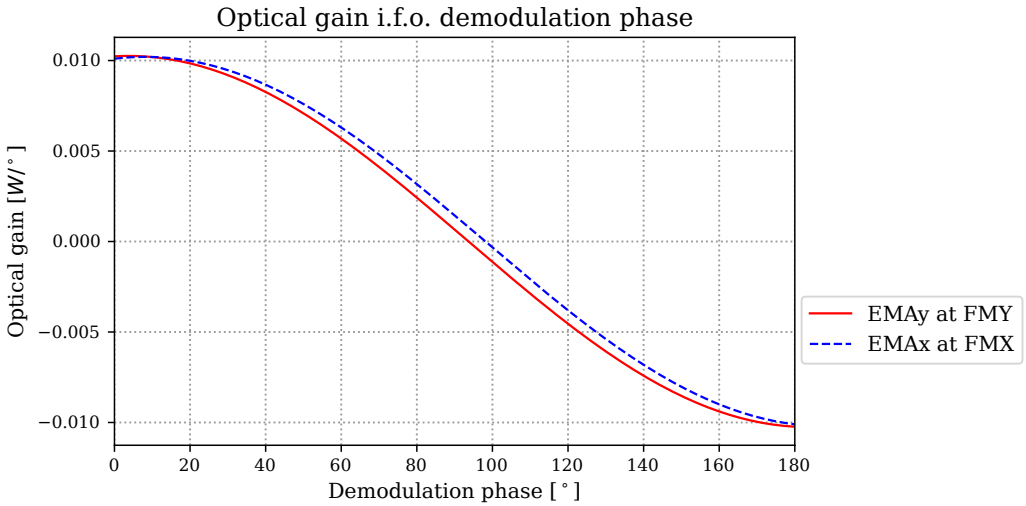

FIGURE 3.1: Finding the optimal demodulation phase, which turned out to be $\phi_x = 8.28°$ and $\phi_y = 3.6°$.

The shape of the simulated error signal for the y-arm cavity is shown in figure 3.2. A signal with this characteristic shape is also called the PDH signal. This error signal is ideal for controlling the cavity length since it has a sharply peaked derivative in the zero-point. The optical gain is 1.02554×10^{-2} W/°. Figure 3.3 shows the same result zoomed in around zero. The error signal is approximately linear for $|\Delta L| < 0.025°$.
In figure 3.4, the PDH signal for the x-arm is shown. The only difference with the y-arm is the addition of an extra folding mirror and a slightly different optimal demodulation phase. The optical gain is 1.02042×10^{-2} W/°, which is about 0.5% lower than the result for y. This is exactly equal to the amount of light lost at the second x-arm folding mirror FM since its transmittance is $T = 0.005$. This simple relation between the two arms is later confirmed by simulation in figure 3.6.

3.1.2 Dependence on transmission coefficient

It is worth looking further at the influence of the transmission coefficient of the FM on the optical gain and related quantities. Intuitively it is clear that higher transmission will result in higher optical gains, but also lower power in the cavity. The consequences of this are shown more quantitatively in the following plots. Each time the comparison is made between the x- and y-arm. As always the

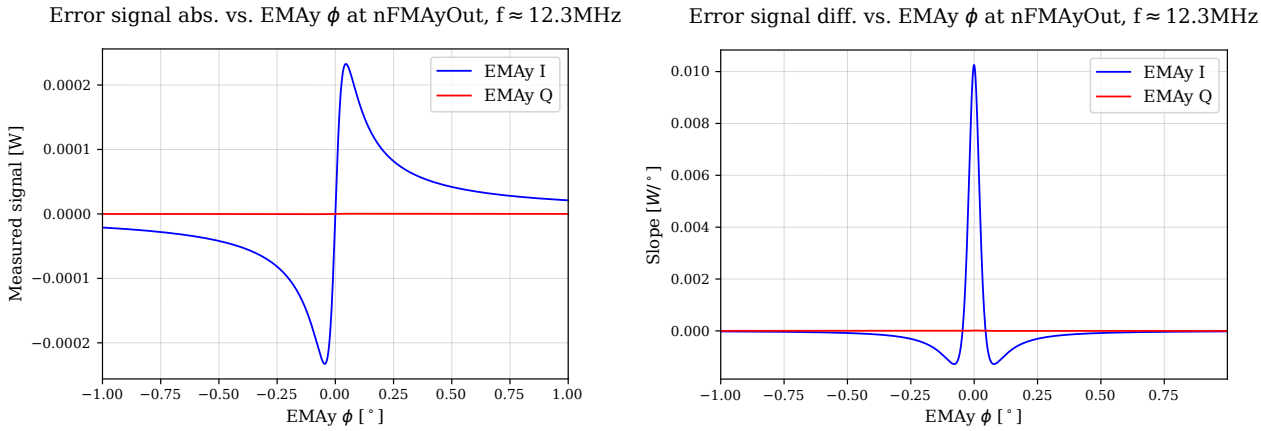

(A) Absolute demodulated signal

(B) Derivative w.r.t. ϕ

FIGURE 3.2: PDH signal of the y-arm cavity.

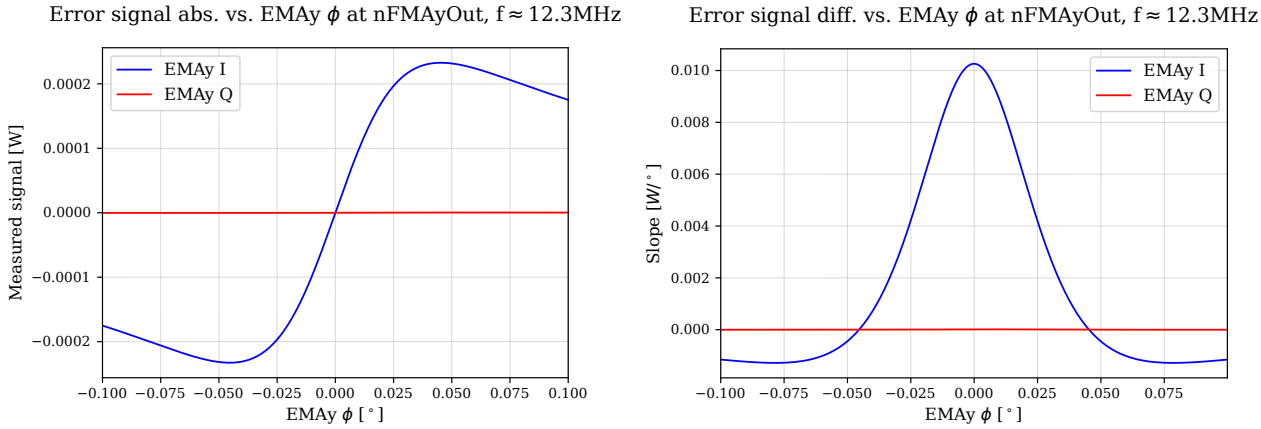

(A) Absolute demodulated signal

(B) Derivative w.r.t. ϕ

FIGURE 3.3: Zoom of the PDH signal of the y-arm cavity

x-arm has two FMs while the y-arm only has one. Some of the plots will be made with a logarithmic x-axis. This is done because the transmittance of the FM is not definitive yet, and it is therefore of interest to consider multiple orders of magnitude.

Fig. 3.5 shows that using two FMs only results in a significant difference once the transmittance becomes high. The value $T_R = 0.005 = 5 \times 10^{-3}$ is indicated by the grey dotted line. The scaling hides this, but the y-gain increases linearly with the transmittance, while the x-gain has two FMs and therefore scales with $T(1-T)$. This because the first x-folding mirror only reflects a fraction $1-T$ of the light. The cavity lets the light circulate for some time until it leaks back out, back to the FM. The optical gain is then linearly related to the amount of light coming the cavity. This becomes evident when considering the ratio between the x- and y-optical gains behaves as $\frac{T(1-T)}{T} = 1-T$, which is clear from figure 3.6.

In the explanation above it was expected the amount of light inside the cavity is linearly related to the amount of light entering it. Fig. 3.7 shows this with a logarithmic axis, and 3.8 shows that the fraction of x-cavity power versus y-cavity power follows $1-T$ again. The asymmetry therefore only has a significant effect on the circulating power for high values of T.

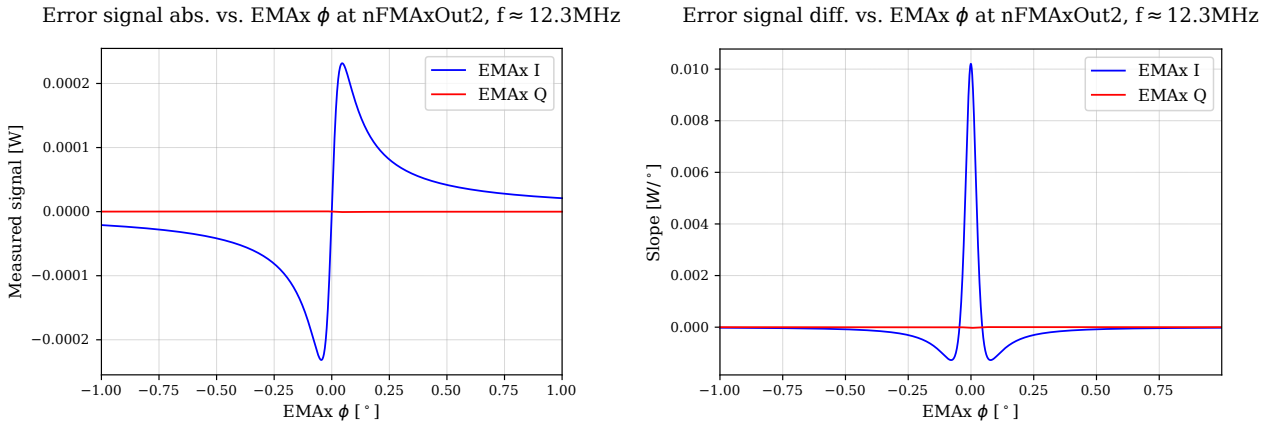

(A) Absolute demodulated signal

(B) Derivative w.r.t. ϕ

FIGURE 3.4: PDH signal x-arm

Quantum shot-noise (qshot noise) is the simplest type of noise to consider in simulation since it can be approximated by white noise around the modulation frequency of 12.3 MHz. This means its spectrum is flat and the noise can therefore be characterised by its average amplitude. At the detection port, the noise increases with the square root of the incoming power [19, Chpt. 2]. This means again that for the lower values of the logarithmic axis, no significant difference between one or two FMs is present. This is shown in fig. 3.9. In this plot both AC and DC noise are considered. DC noise is the directly measured response to a quantum shot-noise inserted into the simulation, so no demodulation is performed. AC refers to noise present in the modulated signal (after demodulation), which is generally slightly lower.

An important quantity to consider is the relative ratio between AC shot-noise and optical gain. This corresponds to the sensitivity of the detector, which is found as

$$\text{Sensitivity}\left[\frac{\text{m}}{\sqrt{\text{Hz}}}\right] = \frac{\text{Noise}\left[\frac{\text{W}}{\sqrt{\text{Hz}}}\right]}{\text{Optical gain}\left[\frac{\text{W}}{\text{m}}\right]}. \tag{3.2}$$

From the trends discussed earlier, the sensitivity in the y-arm is expected to be proportional to $\frac{\sqrt{T}}{T} = \frac{1}{\sqrt{T}}$. The x-arm will have a proportionality to $\frac{\sqrt{T(1-T)}}{T(1-T)} = \frac{1}{\sqrt{T(1-T)}}$. To calculate the sensitivity, the optical gain is first converted to the right units using

$$\text{Optical gain}\left[\frac{\text{W}}{\text{m}}\right] = \frac{2 \cdot 360^\circ \cdot \text{Optical gain}\,[\text{W}/^\circ]}{\lambda\,[\text{m}]}. \tag{3.3}$$

Here the conversion factor for degrees to meters is $2 \cdot 360^\circ / \lambda$. It contains the factor 2 since the degrees under consideration are those of the mirror positioning, while the meters refer to path lengths of the light. Any degree of mirror position change results in two degrees of path length change since the light travels back and forth to the mirror.

Fig. 3.10 shows that sensitivity improves as expected when the FMs become more transmissive. The x- and y-arms do not differ significantly, their fraction would follow $\sqrt{\frac{1}{1-T}}$. It is therefore important when designing the FMs to find a balance between making them more transmissive to achieve higher

sensitivity, while also not increasing the asymmetry between the arms too much. Increasing FM transmittance also has the downside of decreasing the cavity power, therefore lowering the precision of the ITF.

In conclusion the values for $T = 0.005$ are shown in table 3.1. The differences for one vs. two FMs are very small. Most importantly, the cavity power and sensitivity remain very similar. This shows the asymmetry introduced by the FMs will not cause any significant challenges for ETpf and the cavity control.

Quantity	Value y-arm	Value x-arm	Percentage change [%]
Optical gain	1.02554×10^{-2} W/°	1.02042×10^{-2} W/°	−0.5%
Cavity power	587.1 W	584.2 W	−0.5%
AC shot-noise	$1.645 \times 10^{-11} \frac{\mathrm{W}}{\sqrt{\mathrm{Hz}}}$	$1.640 \times 10^{-11} \frac{\mathrm{W}}{\sqrt{\mathrm{Hz}}}$	−0.3%
DC shot-noise	$2.323 \times 10^{-11} \frac{\mathrm{W}}{\sqrt{\mathrm{Hz}}}$	$2.317 \times 10^{-11} \frac{\mathrm{W}}{\sqrt{\mathrm{Hz}}}$	−0.3%
Sensitivity	$3.452 \times 10^{-18} \frac{\mathrm{m}}{\sqrt{\mathrm{Hz}}}$	$3.460 \times 10^{-18} \frac{\mathrm{m}}{\sqrt{\mathrm{Hz}}}$	+0.2%

TABLE 3.1: Summary of important values in this section for FM transmittance $T = 0.005$ and modulation index $m = 0.1$.

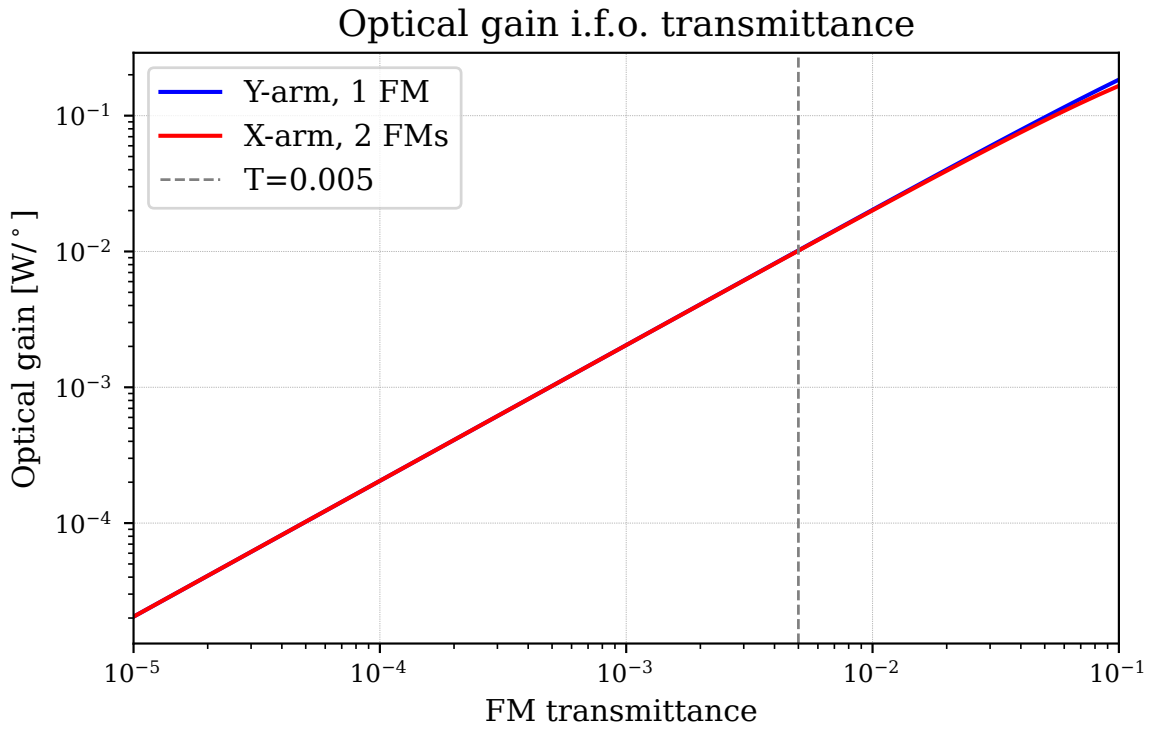

FIGURE 3.5: Optical gain as a function of FM transmittance

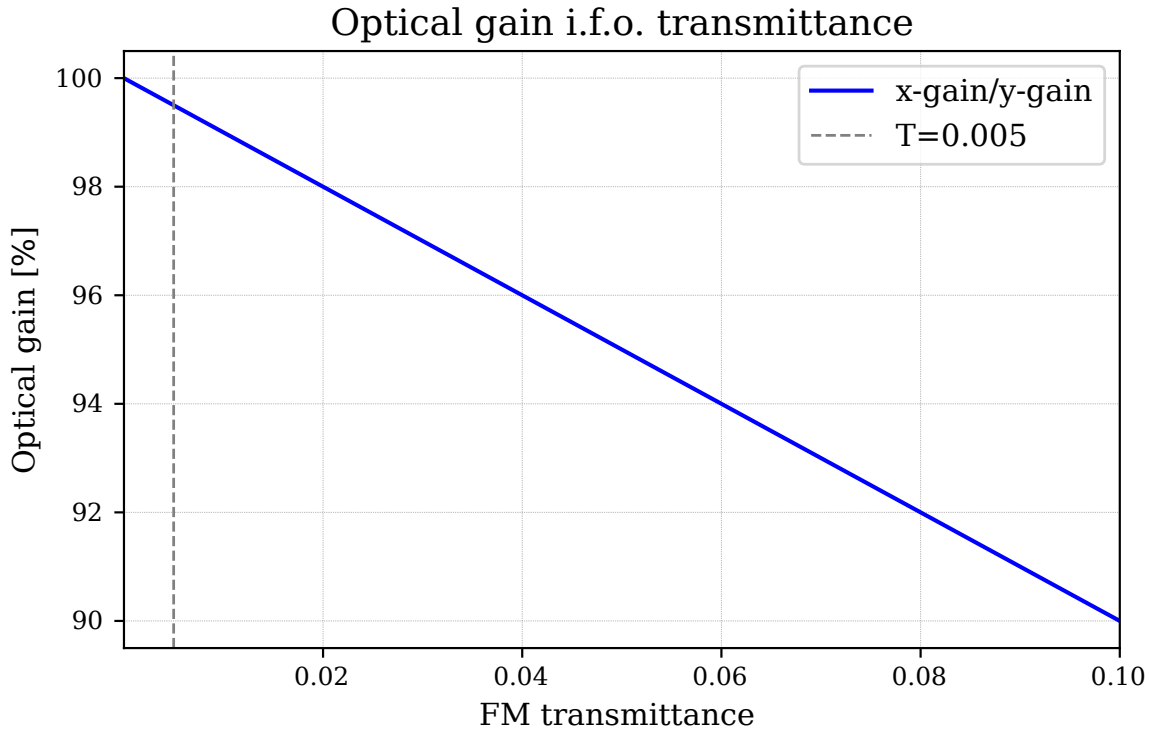

FIGURE 3.6: Optical gain of the x-arm divided by the optical gain of the y-arm. It is given by a percentage as a function of FM transmittance.

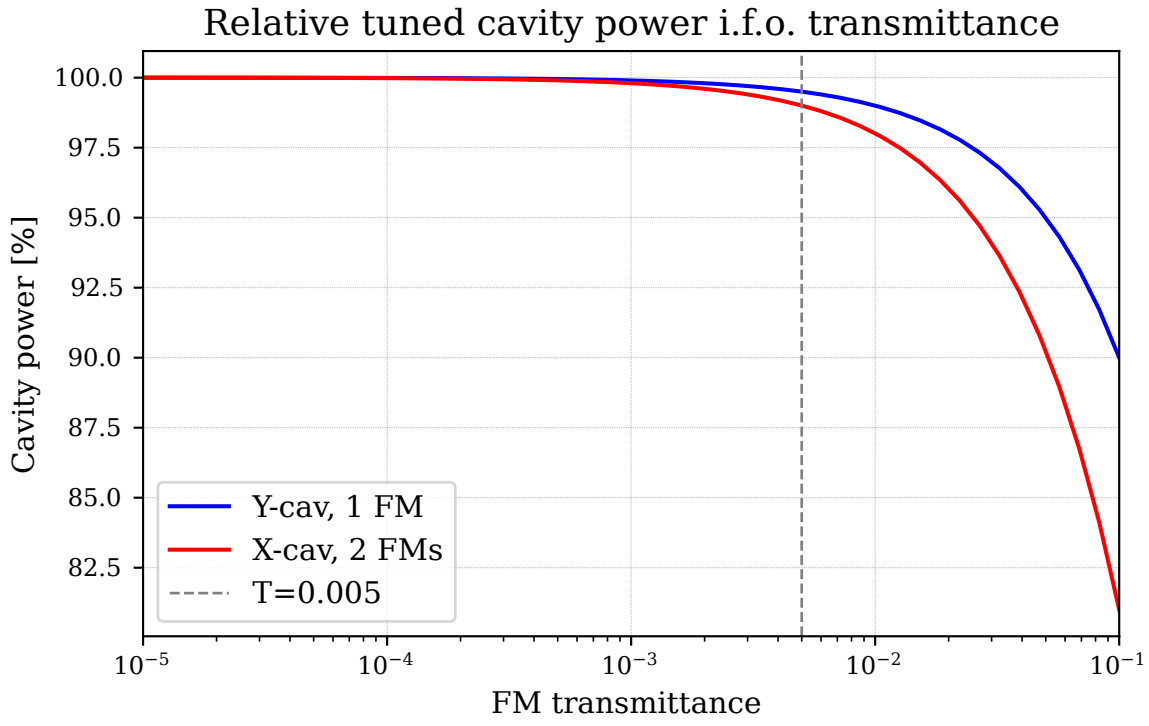

FIGURE 3.7: Relative circulating power as a function of FM transmittance

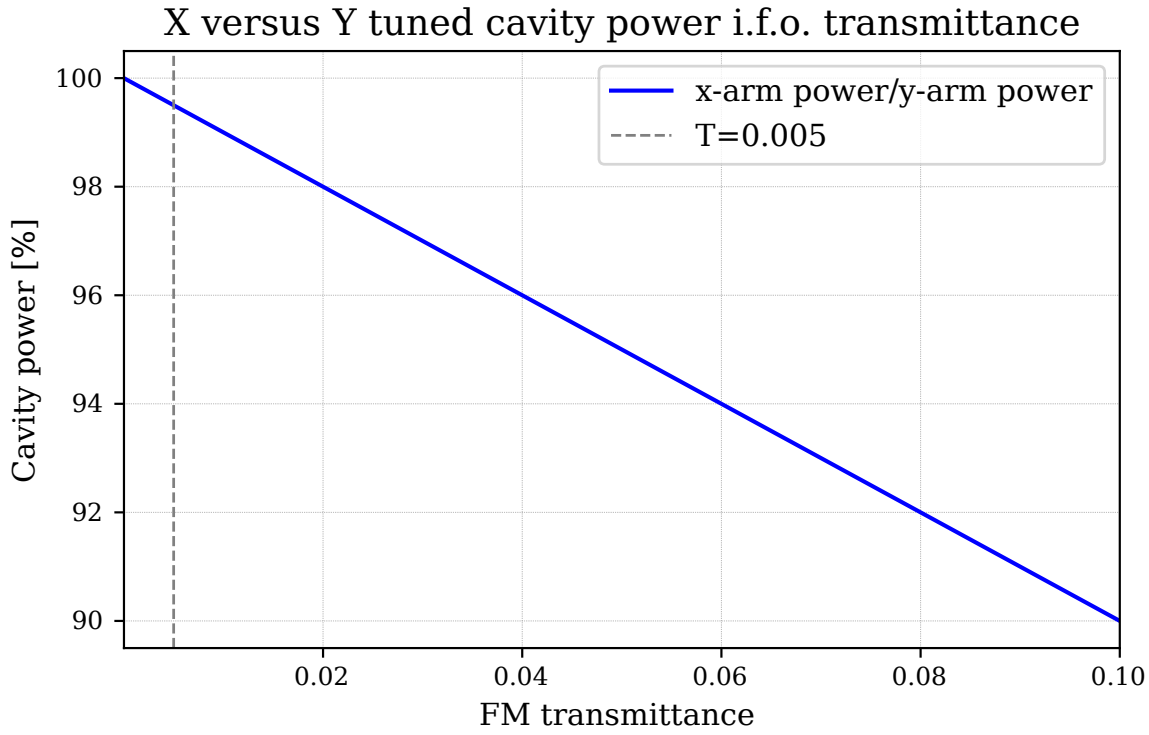

FIGURE 3.8: Circulating power of the x-arm divided by the power in the y-arm. It is given by a percentage as a function of FM transmittance

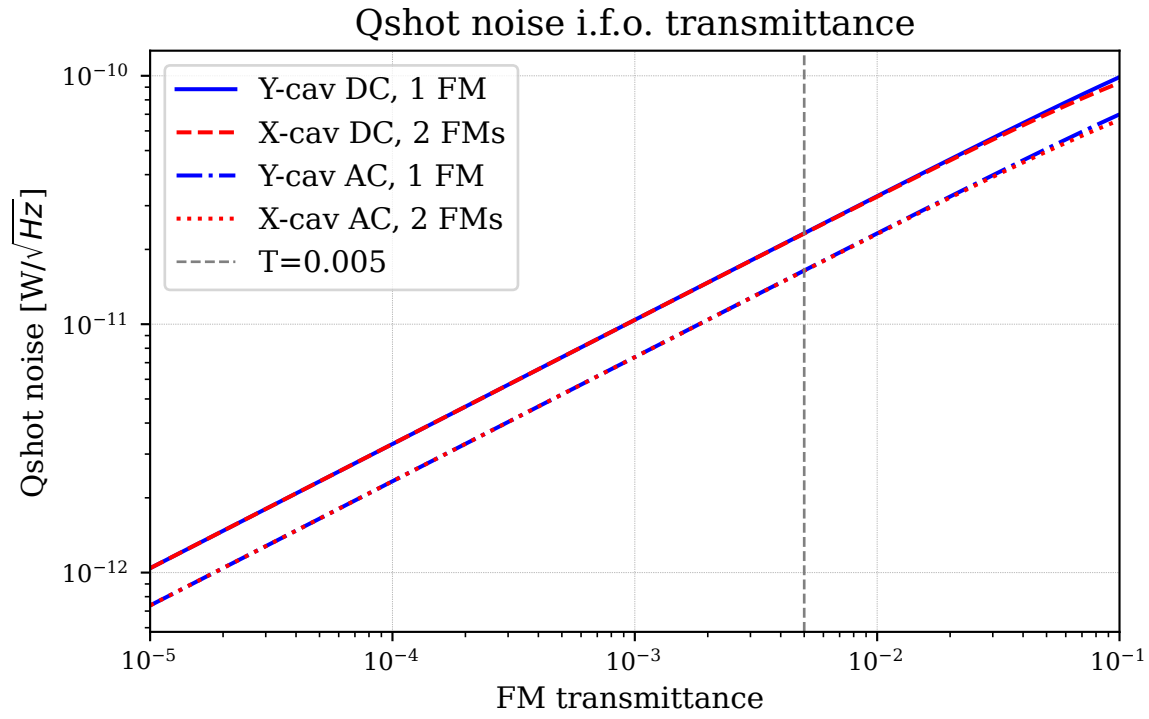

FIGURE 3.9: Quantum shot noise as a function of FM transmittance

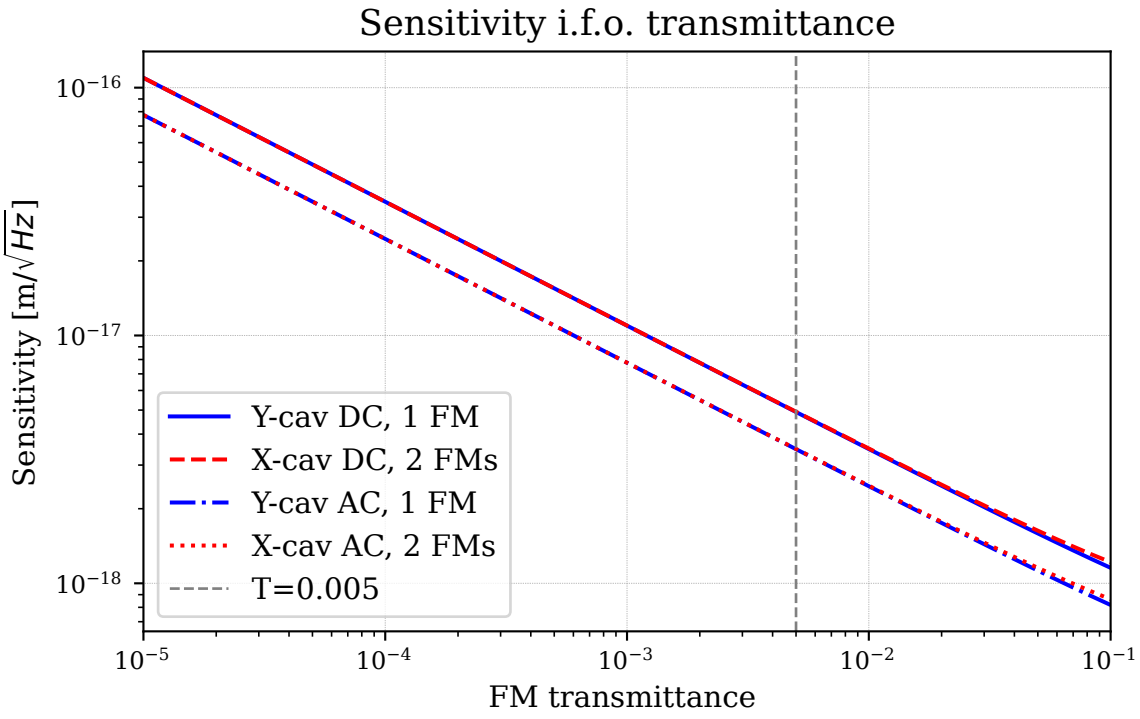

FIGURE 3.10: Noise sensitivity as a function of FM transmittance

3.1.3 Dependence on modulation index

A similar set of simulations has been done for the modulation index. As this value increases, a smaller portion of the light will be present in the carrier. This causes lower power in the cavities, but the sidebands and thus the optical gain will increase in size. The transmission of the FMs is set at $T = 0.005$. Previously a value of $m_R = 0.1$ has been used, this value is indicated by the dotted grey line. In the plots below it is clear that m_R is sufficiently large to have high optical gain without removing too much power from the cavities. Fig. 3.11 and 3.12 show that increasing m above 0.1 would not result in significantly more gain, while it would drastically reduce cavity power. In fig. 3.13 the shot-noise is shown to increase with m. This increase is only very small for DC noise while AC noise is affected slightly more. Fig. 3.14 shows increasing m further would not significantly improve the sensitivity. The sensitivity reached for $m = 0.1$ is already very good, given that ETpf aims for an output sensitivity of $1 \times 10^{-18} \frac{\mathrm{m}}{\sqrt{\mathrm{Hz}}}$ in its first phase [14, Chpt. 6]. A cavity is only one component of the ITF and therefore does not have to be as sensitive as the output detection. The sensitivity attained using the PDH technique with these parameters is therefore promising. It is also again clear that the asymmetry in the two arms does not pose a problem for cavity control. It should be reiterated that shot-noise is not the only source of noise that would be present in experiment. This is therefore a simplified representation.

The values at $m = 0.1$ can again be referenced in table 3.1. Table 3.2 shows all combinations of T and m for comparison. It shows the cavity power losses stemming from m and T are acceptable.

Quantity	$T = 0$ & $m = 0$	$T = 0$ & $m = 0.1$	$T = 0.005$ & $m = 0$
Cavity power x-arm	593.1 W	590.1 W	587.1 W
Cavity power y-arm	593.1 W	590.1 W	590.0 W
AC shot-noise x-arm	/	/	$1.638 \times 10^{-11}\ \frac{\mathrm{W}}{\sqrt{\mathrm{Hz}}}$
AC shot-noise y-arm	/	/	$1.642 \times 10^{-11}\ \frac{\mathrm{W}}{\sqrt{\mathrm{Hz}}}$
DC shot-noise x-arm	/	/	$2.316 \times 10^{-11}\ \frac{\mathrm{W}}{\sqrt{\mathrm{Hz}}}$
DC shot-noise y-arm	/	/	$2.322 \times 10^{-11}\ \frac{\mathrm{W}}{\sqrt{\mathrm{Hz}}}$

TABLE 3.2: Summary of important values in this section comparing different combinations of FM transmittance and modulation index.

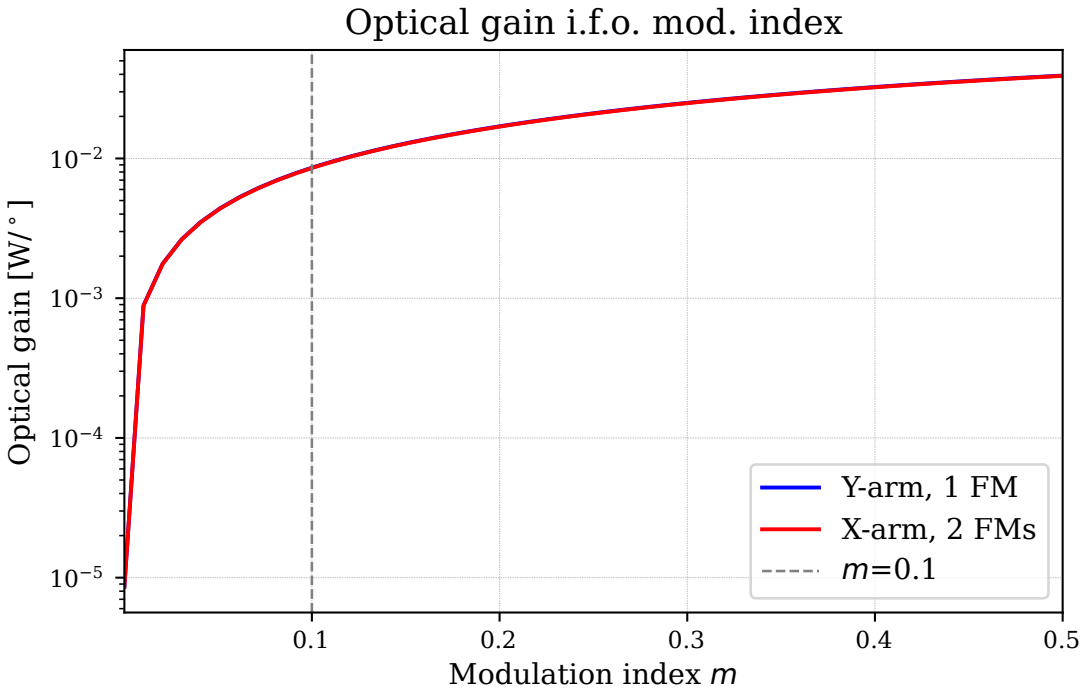

FIGURE 3.11: Optical gain as a function of modulation index

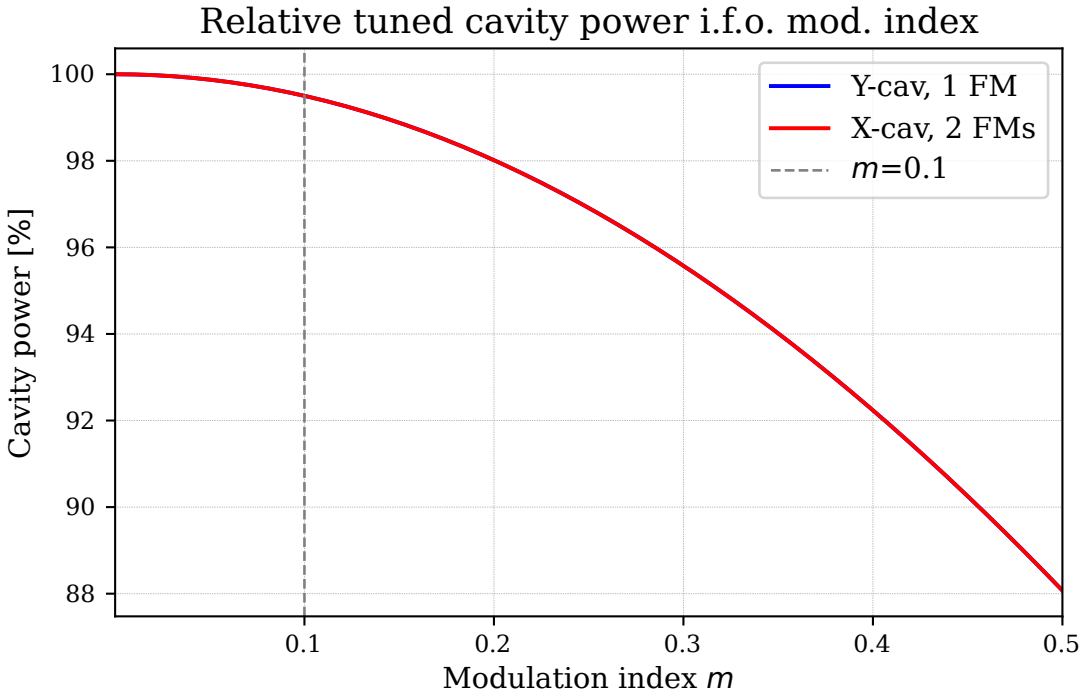

FIGURE 3.12: Relative circulating power as a function of modulation index. These are relative to the initial value for x and y. In general, the x-arm will have slightly lower power than the y-arm because of the two FMs.

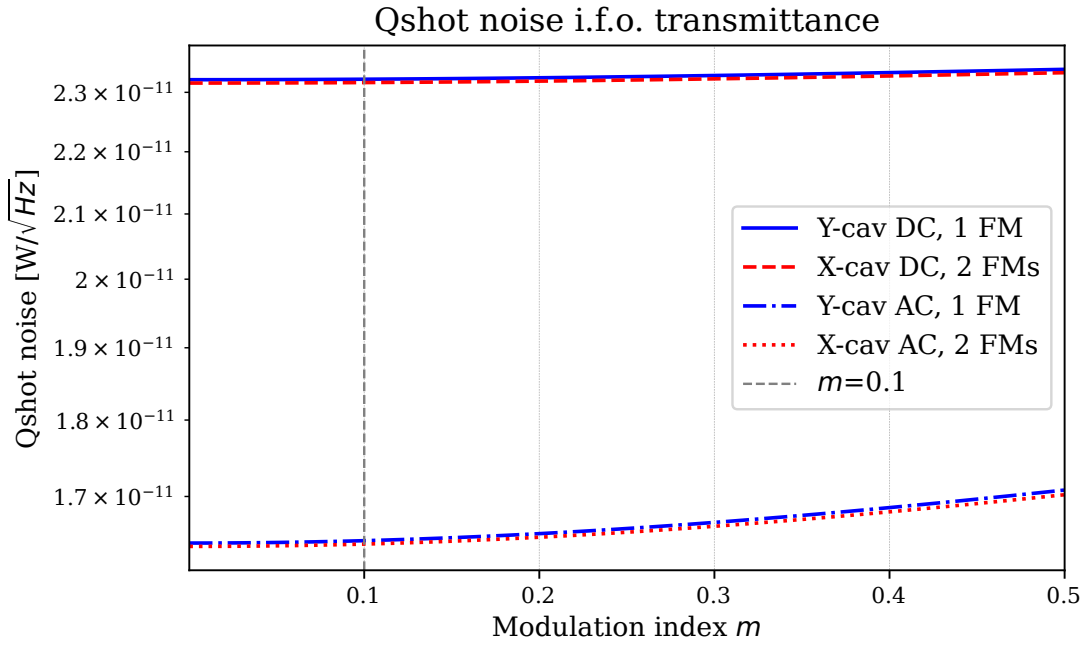

FIGURE 3.13: Quantum shot noise as a function of modulation index

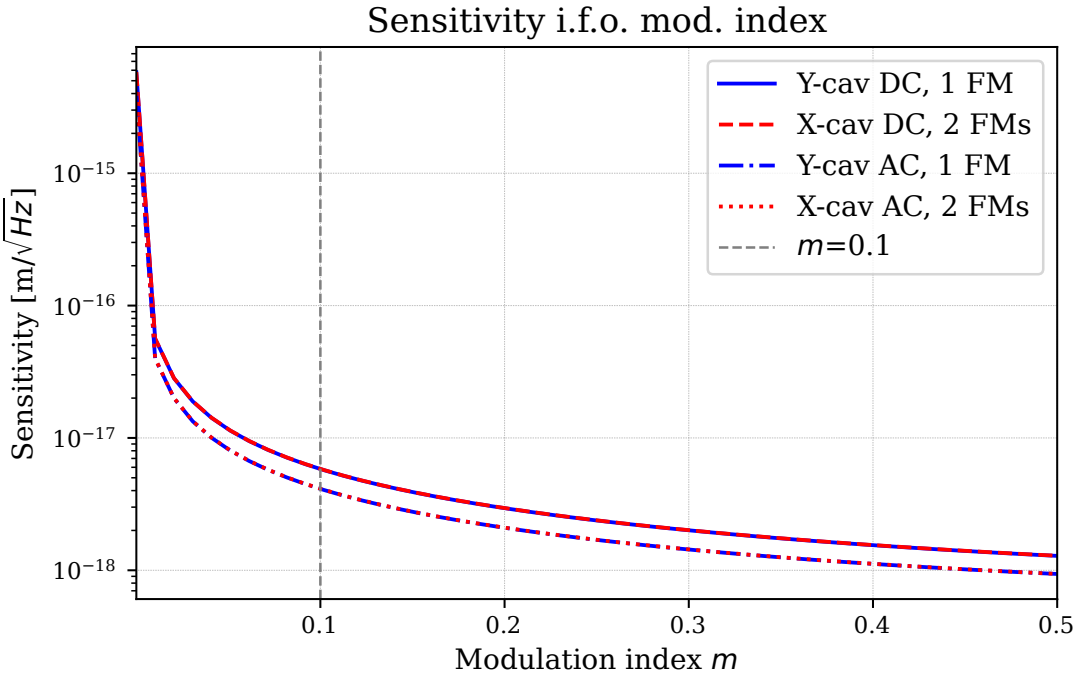

FIGURE 3.14: Noise sensitivity as a function of modulation index

3.2 Control of the combined ITF

All concepts discussed in the previous section can of course be expanded to other longitudinal degrees of freedom (DOFs). The three degrees of freedom that are studied in this work are DARM, CARM and MICH. Their definitions are based on those in [8, Chpt. 8]:

- **DARM**: Differential arm length, DARM = $L_x - L_y$. The definitions of these lengths can be seen in fig. 3.15. DARM is the length difference of the two arm cavities of the interferometer. In general, differential effects are expected to be measured at the output port. This is because differential motions generate sidebands that experience maximal constructive interference at the output port. The same is true for gravitational waves themselves.
- **CARM**: Common-mode arm length, CARM = $L_x + L_y$. This is the sum of the arm cavity lengths. Deviations in CARM can indicate the cavities have moved away from resonance.
- **MICH**: Michelson arm length difference, MICH = $l_x - l_y$. This reflects the difference the difference in length of the short arms of the ITF. These run from the BS to the ITMs and do not include the arm cavities. Keeping MICH under control guarantees the destructive interference condition of the carrier at the output port.

All three DOFs will be used w.r.t. their operating point: if the ITF is locked it means that DARM = CARM = MICH = 0. Any deviations from this point are measured in degrees of the microscopic tuning ϕ of the mirrors involved. A pure DARM motion is generated by moving the ETMs with

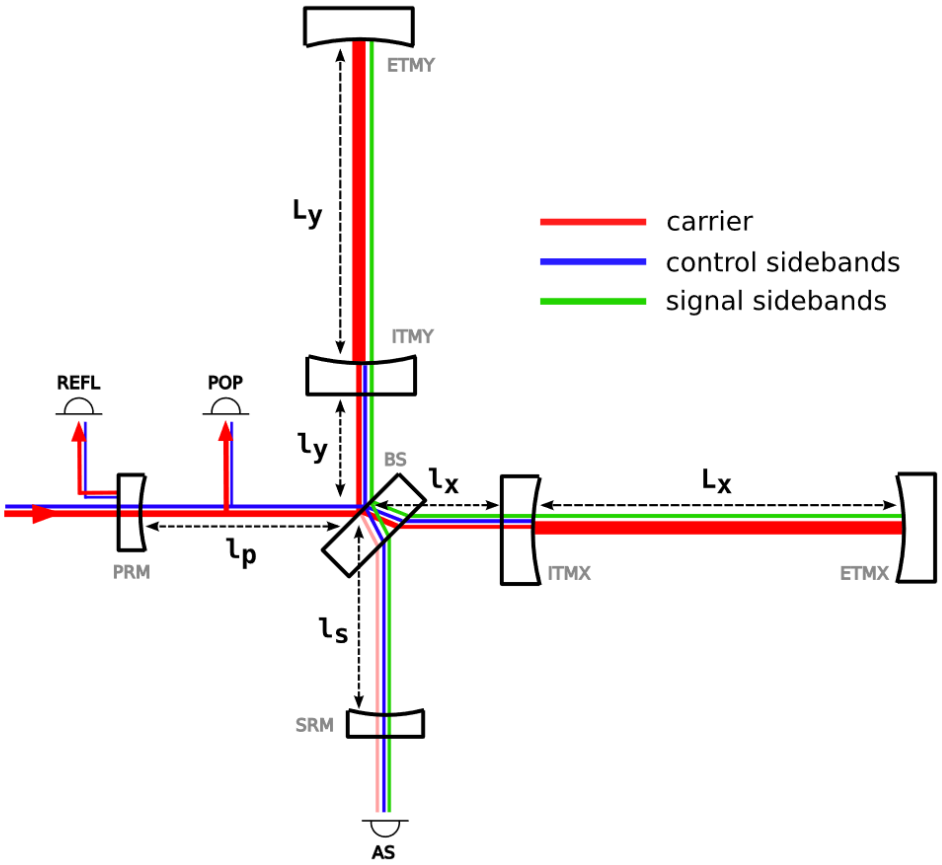

FIGURE 3.15: Schematic illustration of an ITF with all relevant lengths indicated. Also shown are how the carrier, control sidebands and signal sidebands propagate. l_p and l_s are less relevant for ETpf since power- and signal-recycling will (initially) not be implemented [8, App. B].

opposite phase i.e. one is moved away from the ITM and the other is moved towards the ITM. CARM motion involves moving both ETMs in the same direction. In fact, altering the frequency of the laser is similar to a common motion of the end mirrors since they both affect the resonance condition in the cavities. One can either set the frequency to match the length of the cavity or vice versa. This means the CARM DOF is also sensitive to changes of the laser frequency. To create MICH movement the same is done as for DARM, but now the ITMs perform the same motion as the ETM. The cavity length therefore stays constant, while only the short arms of the ITF undergo a length change. The result is similar to an ITF without arm cavities, since the whole cavities can be treated as a mirror that lets some light through and 'reflects' the rest.

For each degree of freedom, an error signal is defined to control that DOF. This will be a measured amount of light at a specific port, with a specific demodulation frequency and phase. Ideally, for example, when DARM deviates from zero, more or less light is measured, indicating that this degree of freedom needs to be corrected. It is important to note that one signal may be sensitive to multiple DOFs, this is the topic of section 3.2.1 and the following. Optical gain is again defined as the derivative of the error signal measured at the zero point of the degree of freedom. Based on [12], some promising measurement locations and phases were selected. The frequency is taken to be the same as for the cavity control: 12.3 MHz.

Ports There are two obvious locations to measure a signal. Firstly, at the output port, also known as the asymmetric (ASY) port because the measurement is taken on the side with destructive interference. This is also where the gravitational wave is measured. Based on theory, it is expected that differential signals such as DARM and MICH couple more strongly to this port. This can be seen in the very simple case considered in eq. 2.9 for example. Secondly, one can also measure at the input port, the symmetric side. The light coming back from the BS in the direction of the laser is measured, which is why it's also called the reflected (REF) port. Here, more effects are expected to be observed that are common in both arms, like with the CARM degree of freedom.

Phases/Quadratures On one hand, one can measure in phase with the modulation, denoted as I. Theoretically this means $\phi_d = 0°$. The other possibility is a measurement with a phase difference of 90°, denoted as Q. This latter signal is orthogonal to the former. Most often both these signals are extracted at one detection port and together they hold the full information on the response to changes in the DOF. In practice, these phases are not used exactly as stated above but rather defined at some advantageous value. Conventionally the phase is selected in a manner that allows the CARM (common) effects to appear in the I-phase, while the DARM and MICH (differential) effects are visible in the Q-phase. This phase is found by generating a motion in the chosen DOF and maximising the optical gain in the chosen error signal.

3.2.1 Introduction to the optical sensing matrix

When expanding the control to multiple degrees of freedom, the system becomes more complex. In the case of the cavity length, the response to changes in the error signal is relatively clear: the length of the cavity needs to be adjusted proportionally to the deviation from zero. When considering the full interferometer, multiple DOFs are present and they become coupled with each other. One signal at a certain demodulation frequency could be influenced by multiple DOFs at the same time. It is not immediately clear what action should be taken as a response to a change. In more mathematical terms, the problem actually becomes a matrix equation that takes into account each DOFs relative contribution to an error signal.

The matrix M can be set up for the four most obvious error signals in the ITF. These are the demodulated signals at the reflected and asymmetric port, both in-phase and at Q-phase. The convention and information surrounding the matrix was based on [20, Chpt. 4].

$$\begin{aligned} &\mathbf{M}\vec{\Delta} = \vec{S}_{demod} \\ \Longleftrightarrow &\begin{bmatrix} M_{CRI} & M_{MRI} & M_{DRI} \\ M_{CRQ} & M_{MRQ} & M_{DRQ} \\ M_{CAI} & M_{MAI} & M_{DAI} \\ M_{CAQ} & M_{MAQ} & M_{DAQ} \end{bmatrix} \cdot \begin{bmatrix} CARM \\ MICH \\ DARM \end{bmatrix} = \begin{bmatrix} REF\ I \\ REF\ Q \\ ASY\ I \\ ASY\ Q \end{bmatrix} \end{aligned} \tag{3.4}$$

The names of the matrix elements reflect the initials of the DOF, the port and the phase in that order. For example, the MICH response measured at the asymetric port at I-phase is M_{MAI}. The phases used are tuned specifically so that common effects (such as CARM) are measured at I-phase and

differential effects (DARM & MICH) are seen at Q-phase. In simulation this is done the same way as it was done for the arm cavities. For example, at the REF port this involves determining the CARM gain of a signal for phases between $[0, 180]$ and then defining the modulation phase of that detector where the CARM gain is maximal. The asymmetric port has maximal DARM gain at Q-phase. The implementation is similar to how this might be done in a real experiment: for CARM the end mirrors are shaken in phase with each other, the signal is measured and the derivative at zero-displacement is found. The phase ϕ_I with the highest derivative (optical gain) is then the optimal one. Conversely at $\phi_Q = \phi_I + 90^\circ$ the CARM gain is approximately zero. For the ASY port it is very similar except ϕ_Q is now optimised for DARM.

Before the actual values in the matrix are discussed, the normalisation of the elements is first shown. Without this, the elements of the matrix are gains measured in $W/^\circ$ or W/m. These depend on a lot of parameters in the ITF that make them difficult to compare to other experiments. The matrix elements can be normalised in a way that is outlined in [21]. In essence each row is divided by the Euclidean (i.e. quadratic) norm of that row. This means the new elements of the normalised matrix $\mathbf{M}'$ are

$$\mathbf{M}'_{ij} = \frac{\mathbf{M}_{ij}}{\sqrt{\sum_{k=1,2,3} |\mathbf{M}_{ik}|^2}}. \tag{3.5}$$

It would be very valuable to have theoretical predictions for these matrix elements. To find these, it is necessary to know the amplitude of the sidebands at the REF and ASY ports. From these the amplitude of the demodulated signal can be found. Eq. 2.32 and also eq. 2.28 show the relevant demodulated amplitude will be equal to $S = A_0 A^*_- + A_+ A^*_0$. The values of these A's can be found as in [12, Chpt. 3] for both the REF and ASY port. This involves treating the whole ITF system as a single compound mirror. The laser hits this 'mirror' and some portion is reflected back to the REF port while the rest passes through to the ASY port. The reflection coefficient can be built similarly to how it was done for eq. 2.8.

First of all, the BS has $r_{BS} = t_{BS} = \frac{\sqrt{2}}{2}$. For an input light field A_{in}, the amount reaching the x- and y-cavity is

$$A_{x,in} = \frac{\sqrt{2}}{2} A_{in} e^{i\phi_x/2},$$
$$A_{y,in} = i\frac{\sqrt{2}}{2} A_{in} e^{i\phi_y/2},$$

where it is assumed the paths to and from the cavity are lossless. This calculation therefore neglects the FMs, which is reasonable since their effect was shown to be very limited in the previous section. ϕ_x and ϕ_y would be the phase accumulated from going to the cavity and back to the BS. A_y has also gained the phase-factor i after passing through the BS. The tuning of the cavities are written as Φ_x and Φ_y, therefore the light fields coming back to the BS are

$$A_{x,out} = \frac{\sqrt{2}}{2} A_{in} e^{i\phi_x} r_c(\Phi_x),$$
$$A_{y,out} = -i\frac{\sqrt{2}}{2} A_{in} e^{i\phi_y} r_c(\Phi_y).$$

Here r_c refers to the cavity reflection coefficient shown in eq. 2.14. $A_{y,out}$ contains a minus sign since the ITF is tuned to the dark fringe. That means the y-arm cavity is set 90° back s.t. a round trip adds a 180° phase. The field at the ASY port is now the part of $A_{x,out}$ that passes through the BS interfering with the part of $A_{y,out}$ that bounces off it. The opposite is true for the REF port.

$$A_{REF} = \frac{1}{2}A_{in}\left(e^{i\phi_x}r_c(\Phi_x) + e^{i\phi_y}r_c(\Phi_y)\right),$$
$$A_{ASY} = \frac{1}{2}A_{in}\left(ie^{i\phi_x}r_c(\Phi_x) - ie^{i\phi_y}r_c(\Phi_y)\right).$$

The reflection and transmission coefficients of the compound mirror are then easily found as

$$r_{com}(\Phi_x,\Phi_y,\phi_x,\phi_y) = \frac{A_{REF}}{A_{in}} = \frac{1}{2}\left(e^{i\phi_x}r_c(\Phi_x) + e^{i\phi_y}r_c(\Phi_y)\right),$$
$$t_{com}(\Phi_x,\Phi_y,\phi_x,\phi_y) = \frac{A_{ASY}}{iA_{in}} = \frac{1}{2}\left(e^{i\phi_x}r_c(\Phi_x) - e^{i\phi_y}r_c(\Phi_y)\right).$$

The following redefinitions can be used to simplify these expressions

$$p_+(\Phi_x,\Phi_y) = \frac{1}{2}\left(r_c(\Phi_x) + r_c(\Phi_y)\right), \tag{3.6}$$
$$p_-(\Phi_x,\Phi_y) = \frac{1}{2}\left(r_c(\Phi_x) - r_c(\Phi_y)\right), \tag{3.7}$$
$$\phi_+ = \phi_x + \phi_y, \tag{3.8}$$
$$\phi_- = \phi_x - \phi_y. \tag{3.9}$$

The reflection and transmission coefficients become

$$r_{com}(\Phi_x,\Phi_y,\phi_x,\phi_y) = e^{i\phi_+/2}\left(p_+\cos(\phi_-/2) + ip_-\sin(\phi_-/2)\right), \tag{3.10}$$
$$t_{com}(\Phi_x,\Phi_y,\phi_x,\phi_y) = e^{i\phi_+/2}\left(p_-\cos(\phi_-/2) + ip_+\sin(\phi_-/2)\right). \tag{3.11}$$

The global phase of $e^{i\phi_+/2}$ can be chosen equal to 1 since any observable quantities will always contain an equal amount of regular and conjugated versions of r and t. For example, the measured carrier power behind a mirror is proportional to $t\cdot t^* = |t|^2$. The global phase factor can therefore just as well be dropped. This means the final expressions become

$$r_{com}(\Phi_x,\Phi_y,\phi_x,\phi_y) = \left(p_+\cos(\phi_-/2) + ip_-\sin(\phi_-/2)\right), \tag{3.12}$$
$$t_{com}(\Phi_x,\Phi_y,\phi_x,\phi_y) = \left(p_-\cos(\phi_-/2) + ip_+\sin(\phi_-/2)\right). \tag{3.13}$$

Now the difference for carrier and sideband should be analysed. Quantities referring to carrier and sideband will be denoted with the subscript 0 and 1 or -1 respectively. Note that the arms will be resonant for the carrier in the locked state. This means Φ_x will be a multiple of half the wavelength, s.t. a round trip in the carrier results in an integer number of wavelengths. In equation form

$$\Phi_{x,0} = 4\pi\frac{L}{\lambda} = 2\frac{L\omega_0}{c} \equiv 0 \mod 2\pi. \tag{3.14}$$

This ensures the resonance condition. The sidebands should however be close to anti-resonant in the cavities. The frequency is in fact chosen based on this condition. This means

$$\Phi_{x,\pm1} = 2\frac{L(\omega_0 \pm \Omega)}{c} \equiv \pm 2\frac{L\Omega}{c} \equiv \pi \mod 2\pi. \tag{3.15}$$

The last equivalence is only approximate since the modulation frequency is not chosen exactly at the anti-resonant frequency but rather at a frequency that is not significantly amplified while still far away from higher order resonances. This is shown in fig. 2.10, the exact anti-resonance is found at $f = \frac{\pi c}{4\pi L} = 8.13\ MHz$. The actual angle in eq. 3.15 is written as $\gamma = \frac{2L\Omega}{c}$. There holds $\Phi_{\pm1} = \Phi_0 \pm \gamma$, which can be generalised to higher orders.

The MICH tunings ϕ were introduced slightly differently: ϕ_x and ϕ_y are already round-trip phases in the small arms. The dark-fringe condition of 180° was already excluded from this definition. The Michelson offset introduced in sec. 2.4 should not be forgotten. This offset is $\phi_M = 2.114$, meaning the BS is misplaced by this angle. In round-trips, the effect is in fact double. This means the following composition is valid

$$\begin{aligned} \phi_- &= 2\phi_M + \Delta\phi_-, \\ \phi_+ &= \Delta\phi_+. \end{aligned} \tag{3.16}$$

Here $\Delta\phi_-$ and $\Delta\phi_+$ are possible fluctuations of the differential and common phase respectively. The phase ϕ_+ is the same for the carrier and the sidebands. The result for ϕ_- however will differ for the carrier and the sidebands. Since the wavelength of the sidebands is slightly shorter or longer than the carrier, the Michelson offset would have a slightly different value. Despite that, since $\Omega << \omega_0$, the difference is negligible. Another difference is introduced by the Schnupp asymmetry l_- which only affects the sidebands. They acquire at least a phase

$$\Delta\phi_{-,\pm1} = 2\frac{l_-(\omega_0 \pm \Omega)}{c} = \pm 2\frac{l_-\Omega}{c}. \tag{3.17}$$

Here the condition $2l_-\omega_0 \equiv 0 \mod 2\pi$ was applied. The angle β is defined as $\beta = \frac{l_-\Omega}{c}$. Finally, the relation between ϕ_- for sideband and carrier can be identified as being

$$\phi_{-,\pm1} = \phi_{-,0} \pm 2\beta. \tag{3.18}$$

For a Schnupp asymmetry of 10 cm and a modulation angular frequency of $\Omega = 2\pi \cdot 12.3$ MHz the angle β equals 1.477°.

3.2.2 Demodulated signal at the REF port

As a first step the fields at the reflected port are analysed. The easiest fields are the sidebands. Their fields are determined by using 3.12. Since the sidebands are anti-resonant in the arms, this implies that

$$r_{c,\pm1}(\Phi_{x/y}) \approx \frac{r_{IM} + r_{EM}}{1 + r_{IM}r_{EM}} \approx 1. \tag{3.19}$$

This means $p_{-,1} = 0 = p_{-,-1}$ and $p_{+,1} = 1 = p_{+,-1}$. Now in general, the reflected field is proportional to the input field E_{in}, the reflection coefficient of the compound mirror $r_{com,\pm}$ and the fraction of power in the sideband (found using the Bessel functions as in 2.18). In mathematical terms

$$A_{REF,+} = J_1(m)E_{in}r_{com,+} = J_1(m)E_{in}\cos(\phi_{-,+1}/2), \tag{3.20}$$
$$A_{REF,-} = J_{-1}(m)E_{in}r_{com,-} = -J_1(m)E_{in}\cos(\phi_{-,-1}/2). \tag{3.21}$$

In [12, Appendix C] a transmission coefficient t_{ref} is also added to denote how much light actually reaches the detector. This would consider the transmittances of all mirrors along the path from the BS to the detector, but in simulation there are none and $t_{ref} = 1$. Applying eq. 3.18 gives

$$A_{REF,+} = J_1(m)E_{in}\cos(\phi_{-,0}/2+\beta), \tag{3.22}$$
$$A_{REF,-} = -J_1(m)E_{in}\cos(\phi_{-,0}/2-\beta). \tag{3.23}$$

For the carrier the coefficients $p_{+,0}$ and $p_{-,0}$ are not trivial and they depend on the DOF being considered. The calculation can be done while keeping the p's as variables. They will be filled in later depending on the DOF under consideration. The following shorter notation is used: $p_+ := p_{+,0}$, $p_- := p_{-,0}$, $J_0 := J_0(m)$, $J_1 := J_1(m)$ and $E := E_{in}$.

$$A_{REF,0} = J_0E\left[p_+\cos(\phi_-/2) + ip_-\sin(\phi_-/2)\right] \tag{3.24}$$

The amplitude of the demodulated signal is now found in eq. 2.28 and can be expanded using

$$\cos(\alpha\pm\beta) = \cos(\alpha)\cos(\beta) \mp \sin(\alpha)\sin(\beta), \tag{3.25}$$
$$\sin(\alpha\pm\beta) = \sin(\alpha)\cos(\beta) \pm \sin(\alpha)\cos(\beta). \tag{3.26}$$

Finally, the calculation for the demodulated signal S_{REF} becomes

$$S_{REF} = A_{REF,0}A^*_{REF,-} + A_{REF,+}A^*_{REF,0} \tag{3.27}$$

$$\begin{aligned} &= J_0J_1|E|^2\{-\left[p_+\cos(\phi_-/2) + ip_-\sin(\phi_-/2)\right]\cos\left(\phi_-/2-\beta\right) \\ &\quad + \left[p^*_+\cos(\phi_-/2) - ip^*_-\sin(\phi_-/2)\right]\cos\left(\phi_-/2+\beta\right)\} \end{aligned} \tag{3.28}$$

$$\begin{aligned} &= J_0J_1|E|^2\{\cos(\phi_-/2)\left[\cos(\phi_-/2)\cos(\beta)(-p_+ + p^*_+) + \sin(\phi_-/2)\sin(\beta)(-p_+ - p^*_+)\right] \\ &\quad + \sin(\phi_-/2)\left[\cos(\phi_-/2)\cos(\beta)(-ip_- - ip^*_-) + \sin(\phi_-/2)\sin(\beta)(-ip_- + ip^*_-)\right]\} \end{aligned} \tag{3.29}$$

$$\begin{aligned} &= J_0J_1|E|^2\{-2i\Im(p_+)\cos(\phi_-/2)^2\cos(\beta) - 2\Re(p_+)\cos(\phi_-/2)\sin(\phi_-/2)\sin(\beta) \\ &\quad - 2i\Re(p_-)\sin(\phi_-/2)\cos(\phi_-/2)\cos(\beta) + 2\Im(p_-)\sin(\phi_-/2)^2\sin(\beta)\} \end{aligned} \tag{3.30}$$

The result becomes more manageable once values for the p's are found. As stated earlier the distinction between DOFs has to be made. For ease of use the equation for r_c is repeated here.

$$r_c(\phi) = \frac{r_{IM} - r_{EM}\exp(2i\phi)}{1 - r_{IM}r_{EM}\exp(2i\phi)} \tag{3.31}$$

DARM For a DARM movement the phases of the x and y cavity change in opposite directions. The DOF is defined as $\Delta\Phi_{=}\Phi_x - \Phi_y$, which is shortened in this calculation to $\Delta\Phi_- = \phi$. The p coefficients can be calculated using $\Phi_x = \phi/2$ and $\Phi_y = -\phi/2$. A small angle approximation is applied, meaning the calculation is only done to first order. This means that $\exp(i\phi) = 1 + i\phi$. The results will only hold for small deviations from the locked state. Finally the constant $r_c = r_c(0)$ is defined and the approximation $F = \frac{\pi}{1-r_{IM}r_{EM}}$ from 2.13 will be used.

$$\begin{aligned}
p_- &= \frac{1}{2}\left(r_c(\phi/2) - r_c(-\phi/2)\right) \\
&= \frac{1}{2}\left(\frac{r_{IM} - r_{EM}\exp(i\phi)}{1 - r_{IM}r_{EM}\exp(i\phi)} - \frac{r_{IM} - r_{EM}\exp(-i\phi)}{1 - r_{IM}r_{EM}\exp(-i\phi)}\right) \\
&\approx \frac{1}{2}\left(\frac{r_{IM} - r_{EM} - r_{EM}i\phi}{1 - r_{IM}r_{EM} - r_{IM}r_{EM}i\phi} - \frac{r_{IM} - r_{EM} + r_{EM}i\phi}{1 - r_{IM}r_{EM} + r_{IM}r_{EM}i\phi}\right) \\
&\approx \frac{1}{2}\left(\frac{2(r_{IM} - r_{EM})r_{IM}r_{EM}i\phi - 2(r_{EM} - r_{IM}r_{EM}^2)i\phi}{(1 - r_{IM}r_{EM})^2}\right) \\
&= \frac{r_{EM}(r_{IM}^2 - 1)i\phi}{(1 - r_{IM}r_{EM})^2} \\
&= \frac{r_{EM}(r_{IM} - 1)(r_{IM} + 1)i\phi}{(1 - r_{IM}r_{EM})^2}
\end{aligned}$$

To make this expression slightly nicer, the approximations $r_{EM}(r_{IM} - 1) \approx r_{IM} - r_{EM}$ and $r_{IM} + 1 \approx 2$ can be made.

$$\begin{aligned}
p_- &\approx 2i\frac{r_c}{1 - r_{IM}r_{EM}}\phi \\
&\approx 2ir_c\frac{F}{\pi}\phi = 2ir_c\frac{F}{\pi}\Delta\Phi_-
\end{aligned}$$

p_+ is found in a similar way.

$$\begin{aligned}
p_+ &= \frac{1}{2}\left(r_c(\phi/2) + r_c(-\phi/2)\right) \\
&\approx \frac{1}{2}\left(\frac{r_{IM} - r_{EM} - r_{EM}i\phi}{1 - r_{IM}r_{EM} - r_{IM}r_{EM}i\phi} + \frac{r_{IM} - r_{EM} + r_{EM}i\phi}{1 - r_{IM}r_{EM} + r_{IM}r_{EM}i\phi}\right) \\
&\approx \frac{1}{2}\left(\frac{2(r_{IM} - r_{EM})(1 - r_{IM}r_{EM})}{(1 - r_{IM}r_{EM})^2}\right) = r_c.
\end{aligned}$$

Since $r_c < 1$ and $\frac{F}{\pi} \approx 635$, $p_+ \approx 0$ is used to make the equations shorter. In the end only the optical gain will be considered, which is a derivative with respect to $\Delta\Phi_-$, so p_+ as a constant will not contribute. The summary of the coefficients for DARM is:

$$p_- \approx 2i\frac{F}{\pi}r_c\Delta\Phi_- \tag{3.32}$$

$$p_+ \approx 0 \tag{3.33}$$

To fill in eq. 3.30, also ϕ_- is needed. For a DARM movement ϕ_- stays constant and it will equal twice the Michelson offset: $\phi_- = 2\phi_M$. The demodulated signal becomes

$$S_{REF} = J_0 J_1 |E|^2 \left(4\frac{F}{\pi} r_c \Delta\Phi_- \sin(\phi_M)^2 \sin(\beta) \right). \tag{3.34}$$

With no DC offset this becomes identically zero, no DARM effect would be measured at the REF port. In the non-zero offset case a small DARM signal will be measured with a real amplitude. Since it is a differential DOF, the convention would be to have it in the Q-component, meaning a phase factor of i should be added to this result. This factor then also has to be applied to all other results at the REF port. The gain is the derivative w.r.t. the DOF $\Delta\Phi_-$

$$\begin{aligned} M_{DRQ} &= 4J_0 J_1 |E|^2 \frac{F}{\pi} r_c \sin(\phi_M)^2 \sin(\beta) && (3.35) \\ &= -7.440458 \times 10^{-5}\ \mathrm{W}/^\circ. && (3.36) \end{aligned}$$

The numerical value was found using the values in table A.1.

CARM For a CARM movement the angle under consideration is $\Delta\Phi_+ = \Phi_x + \Phi_y = \phi$ and the coefficients can be calculated using $\Phi_x = \phi/2$ and $\Phi_y = \phi/2$. The calculation again only needs to be done to first order.

$$\begin{aligned} p_- &= \frac{1}{2}\left(r_c(\phi/2) - r_c(\phi/2)\right) \\ &= 0 \end{aligned}$$

p_+ is found in a similar way as the coefficients for DARM.

$$\begin{aligned} p_+ &= \frac{1}{2}\left(r_c(\phi/2) + r_c(\phi/2)\right) = r_c(\phi/2) \\ &\approx \frac{r_{IM} - r_{EM} - r_{EM} i\phi}{1 - r_{IM} r_{EM} - r_{IM} r_{EM} i\phi} \\ &\approx \frac{[r_{IM} - r_{EM} - r_{EM} i\phi][1 - r_{IM} r_{EM} + r_{IM} r_{EM} i\phi]}{(1 - r_{IM} r_{EM})^2} \\ &= \frac{[r_{IM} - r_{EM}][1 - r_{IM} r_{EM}] - r_{EM} i\phi [1 - r_{IM} r_{EM}] + [r_{IM} - r_{EM}] r_{IM} r_{EM} i\phi}{(1 - r_{IM} r_{EM})^2} \\ &= r_c + i\phi r_{EM} \frac{-1 + r_{IM} r_{EM} + r_{IM}^2 - r_{IM} r_{EM}}{(1 - r_{IM} r_{EM})^2} \\ &= r_c + i\phi r_{EM} \frac{-1 + r_{IM}^2}{(1 - r_{IM} r_{EM})^2} \\ &= r_c + i\phi r_{EM} \frac{(-1 + r_{IM})(1 + r_{IM})}{(1 - r_{IM} r_{EM})^2} \end{aligned}$$

The approximations $r_{EM}(-1+r_{IM}) \approx -r_{EM}+r_{IM}$ and $1+r_{IM} \approx 2$ can be made again to arrive at

$$\begin{aligned} p_+ &\approx r_c - i\phi r_c \frac{2}{(1-r_{IM}r_{EM})} \\ &\approx r_c - 2i\phi r_c \frac{F}{\pi} = r_c(1-2i\frac{F}{\pi}\Delta\Phi_+). \end{aligned}$$

The summary of the coefficients for CARM is

$$\begin{aligned} p_- &= 0, \\ p_+ &\approx r_c(1-2i\frac{F}{\pi}\Delta\Phi_+). \end{aligned}$$

The demodulated signal in eq. 3.30 becomes

$$S_{REF} = J_0 J_1 |E|^2 \left(4i\frac{F}{\pi} r_c \Delta\Phi_+ \cos(\phi_M)^2 \cos(\beta) - 2r_c \cos(\phi_M)\sin(\phi_M)\sin(\beta) \right). \tag{3.37}$$

With no DC offset the imaginary component becomes maximal. To find the matrix element, a phase factor of i should again be added to this result. The gain is the derivative w.r.t. the DOF $\Delta\Phi_+$

$$\begin{aligned} M_{CRI} &= -4J_0 J_1 |E|^2 \frac{F}{\pi} r_c \cos(\phi_M)^2 \cos(\beta) && (3.38) \\ &= 2.114381 \text{ W}/^\circ. && (3.39) \end{aligned}$$

The numerical value was found using the values in table A.1.

MICH In the case of MICH movements, $\Phi_{x/y}$ stays constant. This means $p_- = 0$ and $p_+ = r_c$. What will change however is $\Delta\phi_-$ in eq. 3.16. This was zero in the case of DARM and CARM. Here it is exactly the MICH DOF. In the calculation it will be shortened to $\Delta\phi_- = \phi$, which is considered up to the first order. This means $\cos(\phi) \approx 1$ and $\sin(\phi) \approx \phi$. The demodulated signal becomes

$$\begin{aligned} S_{REF} &= J_0 J_1 |E|^2 \left[-2r_c \cos(\phi_M + \phi/2)\sin(\phi_M + \phi/2)\sin(\beta) \right] && (3.40) \\ &= -2J_0 J_1 |E|^2 r_c \sin(\beta) \left[\cos(\phi_M)\cos(\phi/2) - \sin(\phi_M)\sin(\phi/2) \right] \cdot && (3.41) \\ &\quad \left[\sin(\phi_M)\cos(\phi/2) + \cos(\phi_M)\sin(\phi/2) \right] && (3.42) \\ &\approx -2J_0 J_1 |E|^2 r_c \sin(\beta) \left[\cos(\phi_M) - \sin(\phi_M)\phi/2 \right] \cdot && (3.43) \\ &\quad \left[\sin(\phi_M) + \cos(\phi_M)\phi/2 \right] && (3.44) \\ &= -2J_0 J_1 |E|^2 r_c \sin(\beta) \left[\cos(\phi_M)\sin(\phi_M) + \left(\cos(\phi_M)^2 - \sin(\phi_M)^2 \right) \phi/2 \right] && (3.45) \\ &= -2J_0 J_1 |E|^2 r_c \sin(\beta) \left[\cos(\phi_M)\sin(\phi_M) + \cos(2\phi_M)\phi/2 \right]. && (3.46) \end{aligned}$$

The optical gain and matrix element now becomes

$$\begin{aligned} M_{MRQ} &= -2J_0 J_1 |E|^2 \cos(2\phi_M)\sin(\beta) && (3.47) \\ &= 4.317419 \times 10^{-5} W/^\circ && (3.48) \end{aligned}$$

With this the theoretical values for the first two rows of the sensing matrix are known. Now the same treatment will be done for the asymmetric port to complete the matrix.

3.2.3 Demodulated signal at the ASY port

The sideband fields are now determined by using 3.13. The transmitted field is also proportional to the input field E_{in}, the transmission coefficient of the compound mirror $t_{com,\pm}$ and the fraction of power in the sideband (found using the Bessel functions as in 2.18). In mathematical terms:

$$A_{ASY,+} = J_1(m)E_{in}t_{com,+} = iJ_1(m)E_{in}\sin(\phi_{-,+1}/2), \tag{3.49}$$
$$A_{ASY,-} = J_{-1}(m)E_{in}t_{com,-} = -iJ_1(m)E_{in}\sin(\phi_{-,-1}/2). \tag{3.50}$$

The factor t_{ASY} is again omitted. Applying eq. 3.18 gives

$$A_{REF,+} = iJ_1(m)E_{in}\sin(\phi_{-,0}/2+\beta), \tag{3.51}$$
$$A_{REF,-} = -iJ_1(m)E_{in}\sin(\phi_{-,0}/2-\beta). \tag{3.52}$$

For the carrier the coefficients $p_+ := p_{+,0}$ and $p_0 := p_{-,0}$ are not trivial and they depend on the DOF being considered. The calculation can again be done without specifying the values of the p's.

$$A_{ASY,0} = J_0E\left[p_-\cos(\phi_-/2)+ip_+\sin(\phi_-/2)\right] \tag{3.53}$$

The demodulated signal becomes

$$S_{ASY} = A_{ASY,0}A^*_{ASY,-}+A_{ASY,+}A^*_{ASY,0} \tag{3.54}$$

$$\begin{aligned}&= J_0J_1|E|^2\left\{i\left[p_-\cos(\phi_-/2)+ip_+\sin(\phi_-/2)\right]\sin\left(\phi_-/2-\beta\right)\right.\\&\quad\left.+i\left[p^*_-\cos(\phi_-/2)-ip^*_+\sin(\phi_-/2)\right]\sin\left(\phi_-/2+\beta\right)\right\}\end{aligned} \tag{3.55}$$

$$\begin{aligned}&= J_0J_1|E|^2\left\{\cos(\phi_-/2)\left[\sin(\phi_-/2)\cos(\beta)(ip_-+ip^*_-)\ +\cos(\phi_-/2)\sin(\beta)(-ip_-+ip^*_-)\right]\right.\\&\quad\left.+\sin(\phi_-/2)\left[\sin(\phi_-/2)\cos(\beta)(-p_++p^*_+)+\ \cos(\phi_-/2)\sin(\beta)(p_++p^*_+)\right]\right\}\end{aligned} \tag{3.56}$$

$$\begin{aligned}&= J_0J_1|E|^2\left\{2i\Re(p_-)\cos(\phi_-/2)\sin(\phi_-/2)\cos(\beta)+2\Im(p_-)\cos(\phi_-/2)^2\sin(\beta)\right.\\&\quad\left.-2i\Im(p_+)\sin(\phi_-/2)^2\cos(\beta)+2\Re(p_+)\sin(\phi_-/2)\cos(\phi_-/2)\sin(\beta)\right\}\end{aligned} \tag{3.57}$$

The p's are the same as in the case of the reflected port, the results are repeated below and applied to eq. 3.57.

DARM

$$p_- \approx 2i\frac{F}{\pi}r_c\Delta\Phi_- \tag{3.58}$$

$$p_+ \approx 0 \tag{3.59}$$

This leads to a signal of

$$S_{ASY} = J_0J_1|E|^2\left(4\frac{F}{\pi}r_c\Delta\Phi_-\cos(\phi_M)^2\sin(\beta)\right). \tag{3.60}$$

Since it is a differential DOF, the convention would be to have it's error signal in the Q-component, meaning a phase factor of i should be added to this result. This factor then also has to be applied to all other results at the ASY port. The gain is

$$M_{DAQ} = 4J_0J_1|E|^2\frac{F}{\pi}r_c\cos(\phi_M)^2\sin(\beta) \tag{3.61}$$

$$= -5.460604\times10^{-2}\ \mathrm{W}/^\circ. \tag{3.62}$$

This matrix element is related to the CARM REF element by $M_{DAQ} = -\tan(\beta)M_{CRI}$ with $\tan(\beta) \approx 0.026$, showing the influence of the angle β. If no Schnupp asymmetry was added, $\beta = 0$ and DARM would not be measured at this port.

CARM

$$p_- = 0,$$
$$p_+ \approx r_c(1-2i\frac{F}{\pi}\Delta\Phi_+).$$

The demodulated signal in eq. 3.30 becomes

$$S_{ASY} = J_0J_1|E|^2\left(4i\frac{F}{\pi}r_c\Delta\Phi_+\sin(\phi_M)^2\cos(\beta) + 2r_c\cos(\phi_M)\sin(\phi_M)\sin(\beta)\right). \tag{3.63}$$

To find the matrix element, a phase factor of i should again be added to this result.

$$M_{CAI} = -4J_0J_1|E|^2\frac{F}{\pi}r_c\sin(\phi_M)^2\cos(\beta) \tag{3.64}$$

$$= 2.880994\times10^{-3}\ \mathrm{W}/^\circ. \tag{3.65}$$

The numerical value was found using the values in table A.1.

MICH

$$p_- = 0,$$
$$p_+ = r_c.$$

S_{ASY} is found similar to the REF case. In the calculation the MICH DOF will be shortened to $\Delta\phi_- = \phi$, which is considered up to the first order. The demodulated signal becomes the same as for the REF port with an opposite sign

$$S_{ASY} = J_0 J_1 |E|^2 \left[2 r_c \cos(\phi_M + \phi/2) \sin(\phi_M + \phi/2) \sin(\beta)\right] \tag{3.66}$$
$$= 2 J_0 J_1 |E|^2 r_c \sin(\beta) \left[\cos(\phi_M) \sin(\phi_M) + \cos(2\phi_M)\phi/2\right]. \tag{3.67}$$

The optical gain and matrix element again becomes

$$M_{MAQ} = 2 J_0 J_1 |E|^2 \cos(2\phi_M) \sin(\beta) \tag{3.68}$$
$$= -4.317419 \times 10^{-5} W/^\circ \tag{3.69}$$

3.2.4 Theoretical sensing matrix

The previous calculations can now all be summarised in the sensing matrix as it is predicted by the theory. The matrix that is found is

$$\mathbf{M}_{theory} = \begin{bmatrix} M_{CRI} & M_{MRI} & M_{DRI} \\ M_{CRQ} & M_{MRQ} & M_{DRQ} \\ M_{CAI} & M_{MAI} & M_{DAI} \\ M_{CAQ} & M_{MAQ} & M_{DAQ} \end{bmatrix} \tag{3.70}$$

$$= 2 J_0 J_1 |E|^2 r_c \begin{bmatrix} -2\frac{F}{\pi}\cos(\phi_M)^2 \cos(\beta) & 0 & 0 \\ 0 & -\cos(2\phi_M)\sin(\beta) & 2\frac{F}{\pi}\sin(\phi_M)^2 \sin(\beta) \\ -2\frac{F}{\pi}\sin(\phi_M)^2 \cos(\beta) & 0 & 0 \\ 0 & \cos(2\phi_M)\sin(\beta) & 2\frac{F}{\pi}\cos(\phi_M)^2 \sin(\beta) \end{bmatrix} \tag{3.71}$$

$$= \begin{bmatrix} 2.1144 \times 10^{0} & 0 & 0 \\ 0 & 4.3174 \times 10^{-5} & -7.4405 \times 10^{-5} \\ 2.8810 \times 10^{-3} & 0 & 0 \\ 0 & -4.3174 \times 10^{-5} & -5.4606 \times 10^{-2} \end{bmatrix} \tag{3.72}$$

After normalisation this matrix becomes

$$\mathbf{M}'_{theory} \begin{bmatrix} 1 & 0 & 0 \\ 0 & 0.50189 & -0.86493 \\ 1 & 0 & 0 \\ 0 & -0.00079 & -1 \end{bmatrix} \tag{3.73}$$

This shows the REF I channel is suited for controlling the CARM DOF. The DARM DOF could be read out at the port with maximal gain, which is ASY Q. The effect of MICH should be taken into account there. MICH response is currently equal in REF Q and ASY Q. The choice for the better port may also take noise into account. The simplest case would be to consider only shot-noise, which depends on the power hitting the detector. It also shows up in the demodulated signal (AC shot-noise), a formula for this is taken from [19, Chpt. 2]. AC shot-noise influences the demodulated signal power

as

$$\delta P_{AC,shot} = \sqrt{\frac{hcP_{DC}}{\eta\lambda}}. \tag{3.74}$$

Here h is the Planck constant, P_{DC} is the undemodulated signal at the detector and η is the quantum efficiency of the detector which will be unity for simulated detectors. As stated earlier, around the modulation frequency shot-noise is approximately flat meaning there is no frequency dependence. The following DC powers are measured at the REF and the ASY port in simulation

$$P_{DC,REF} = 828.9840 \text{ mW}, \tag{3.75}$$
$$P_{DC,ASY} = 4.5389 \text{ mW}. \tag{3.76}$$

The shot-noise is therefore

$$\delta P_{AC,shot,REF} = 3.260 \times 10^{-10} \frac{\text{W}}{\sqrt{\text{Hz}}}, \tag{3.77}$$
$$\delta P_{AC,shot,ASY} = 2.412 \times 10^{-11} \frac{\text{W}}{\sqrt{\text{Hz}}}. \tag{3.78}$$

Since the simulated DC power was used this is only a pseudo-theoretical result and is simply checked to make sure everything in the simulation is understood. The sensitivities can again be found using eq. 3.2, the first two rows using the REF shot-noise and the last two the ASY shot-noise. This results in the sensitivity matrix in $m/\sqrt{Hz}$ given by

$$\mathbf{S}_{theory} = \begin{bmatrix} 3.3187 \times 10^{-19} & / & / \\ / & 1.6253 \times 10^{-14} & 9.4307 \times 10^{-15} \\ 1.8022 \times 10^{-17} & / & / \\ / & 1.2026 \times 10^{-15} & 9.5084 \times 10^{-19} \end{bmatrix} \tag{3.79}$$

This indicates that ASY Q might be a better port for measuring the MICH DOF since the amount of shot-noise is lower.

3.2.5 Simulated sensing matrix

It's not possible to experimentally verify these results at the moment. However, they are expected to match the simulation, which serves as an initial test. Before finding the matrices, the technique for determining the correct demodulation phase should be described. The method is inspired by [21, Chpt. 3], where it is done for angular control. For every matrix element the simulation loops from 0° to 180° and finds the phase that yields the maximal gain. The minimum is consistently this value plus 90°. The REF port phase is then set to the maximal CARM I-gain ($\phi_{REF} \approx 167.4°$), which automatically maximises MICH Q-gain. Similarly, the ASY port is optimised for maximal DARM Q-gain ($\phi_{ASY} \approx 146.9°$), which gives high MICH Q-gain as well since MICH effects are close to in-phase with DARM. The process is shown in fig. 3.16.

An issue with this technique is that the 'correct' phase is never perfectly found like it is easy to do in theory. For example, because of numerical limitations, the looping over the phases never exactly hits the maximum or the zero crossing. Therefore, not all CARM signal will be in the I-component,

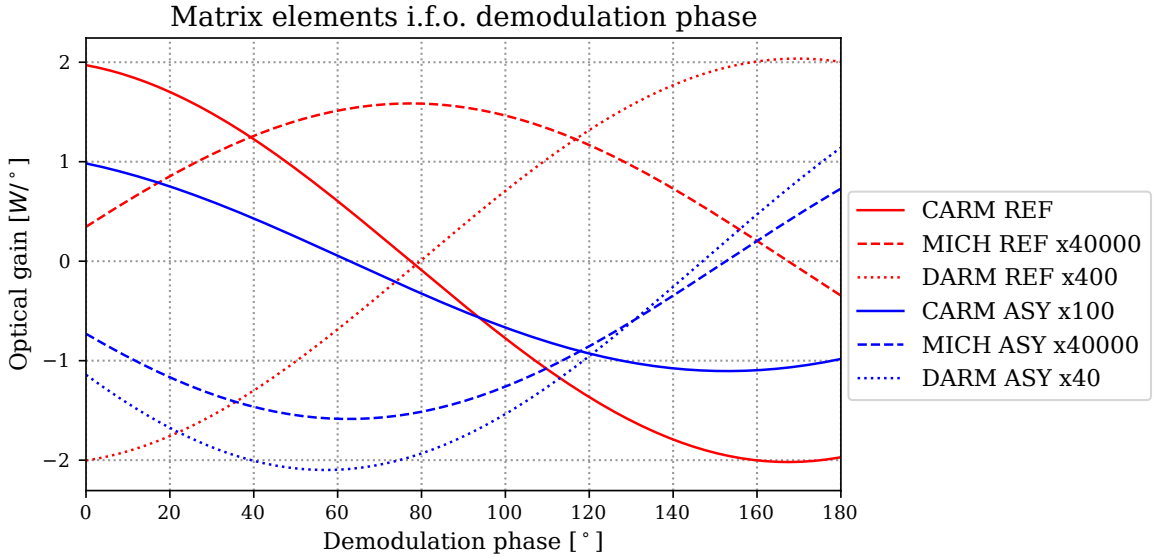

FIGURE 3.16: Finding the optimal demodulation phase, which turned out to be $\phi_{REF} \approx 167.4°$ and $\phi_{ASY} \approx 146.9°$. Some curves have been multiplied by constant factors to make them visible.

some will 'leak' into the Q-component as well. It does seem realistic this will be the case in the real experiment as well. It could be fixed in simulation by increasing the phase accuracy further, but that would not be realistic for an experiment. This simulation was run with an accuracy of two decimal places on the phase.

The simulated sensing matrix is now shown in eq. 3.81. The normalised matrix is given in eq. 3.82. The 'diagonal' elements (if the third row is removed) M_{CRI}, M_{MRQ} and M_{DAQ} are predicted relatively well by the theory. The simulated results are all within 10% of the theoretical values. The Michelson offset causes the non-zero values of the matrix elements M_{CAI} and M_{DRQ}. However, the theory underestimates their size by approximately an order of magnitude. This then makes the REF Q signal less suited for reading the MICH signal as the signal will be dominated by the DARM DOF, which is clear from the normalised matrix. This currently forms a problem for the MICH control. It does turn out that CARM and DARM can be read out without trouble since their diagonal values are close to unity.

$$\mathbf{M}_{simulation} = \begin{bmatrix} M_{CRI} & M_{MRI} & M_{DRI} \\ M_{CRQ} & M_{MRQ} & M_{DRQ} \\ M_{CAI} & M_{MAI} & M_{DAI} \\ M_{CAQ} & M_{MAQ} & M_{DAQ} \end{bmatrix} \tag{3.80}$$

$$= \begin{bmatrix} 2.0189 \times 10^{0} & 5.9723 \times 10^{-9} & -5.0877 \times 10^{-3} \\ -8.7752 \times 10^{-5} & 3.9648 \times 10^{-5} & -1.9948 \times 10^{-4} \\ 1.0990 \times 10^{-2} & 3.8383 \times 10^{-6} & -7.7740 \times 10^{-6} \\ 1.1156 \times 10^{-3} & -3.9462 \times 10^{-5} & -5.2473 \times 10^{-2} \end{bmatrix} \tag{3.81}$$

$$\mathbf{M}'_{simulation} = \begin{bmatrix} 1.00000 & 0.00000 & -0.00252 \\ -0.39615 & 0.17899 & -0.90057 \\ 1.00000 & 0.00035 & -0.00071 \\ 0.02126 & -0.00075 & -0.99977 \end{bmatrix} \tag{3.82}$$

Readers interested in the influence of the FMs are referred to appendix C. The difference is most noticeable in three matrix elements that were predicted to be zero: M_{DRI}, M_{MAI} and M_{CAQ}. Without FMs, the simulation is closer to this prediction. It seems that the asymmetry introduced by the FMs causes an increase in the response in these error signals. Their value is still very low and therefore they will not pose a challenge when trying to control the three DOFs. It is concluded that the asymmetric FMs will not create an issue for the longitudinal control of the combined ITF.

The error signals that are intended to be used are shown in the figures below. The DARM error signal is shown in fig. 3.17. The error signal for CARM is given in fig. 3.18. The two error signals for MICH are provided in 3.19 and 3.20. The names 'nBSin' and 'nout' refer to the nodes of measurement, which are the REF and ASY port respectively.

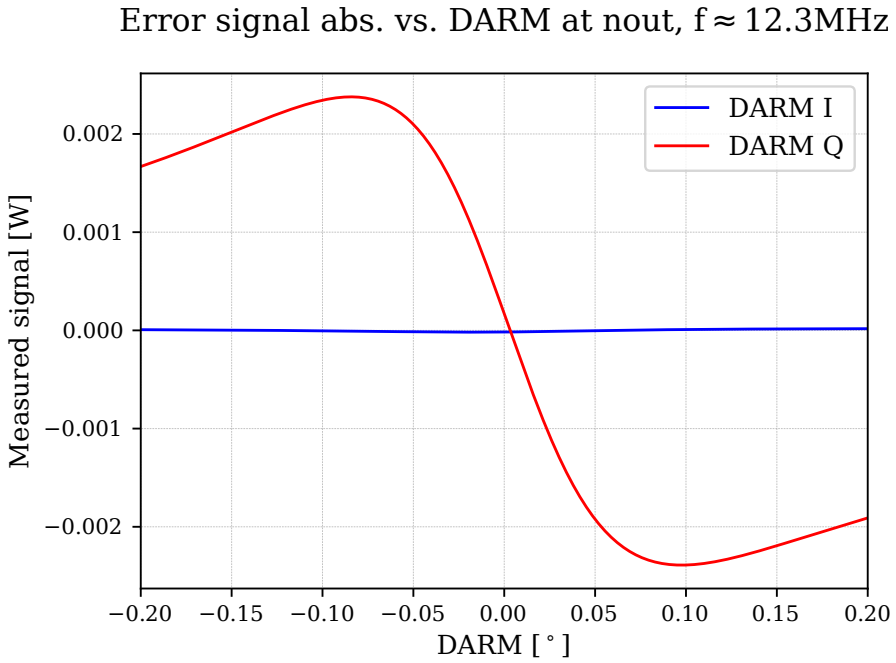

FIGURE 3.17: DARM error signal at ASY port.

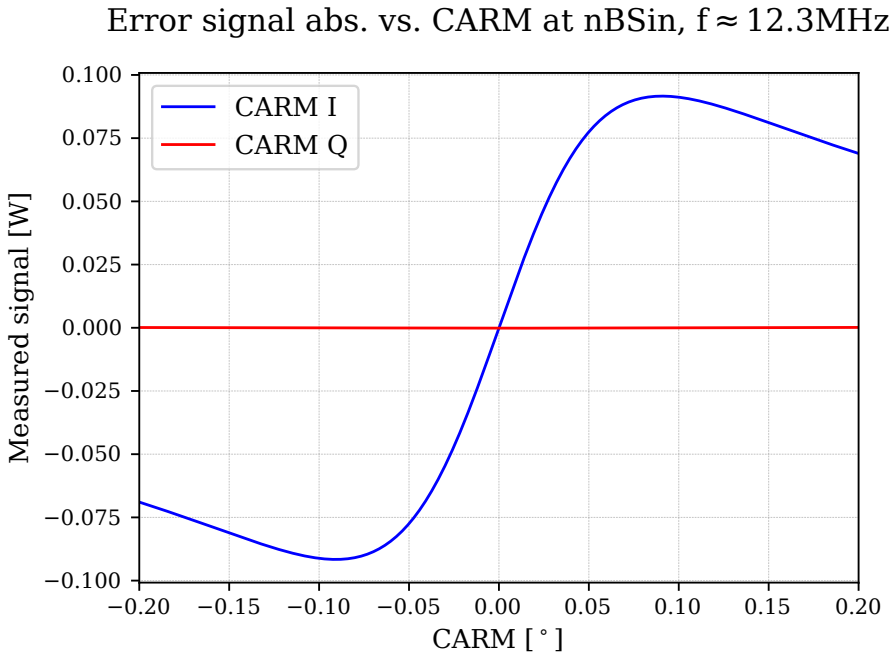

FIGURE 3.18: CARM error signal at REF port.

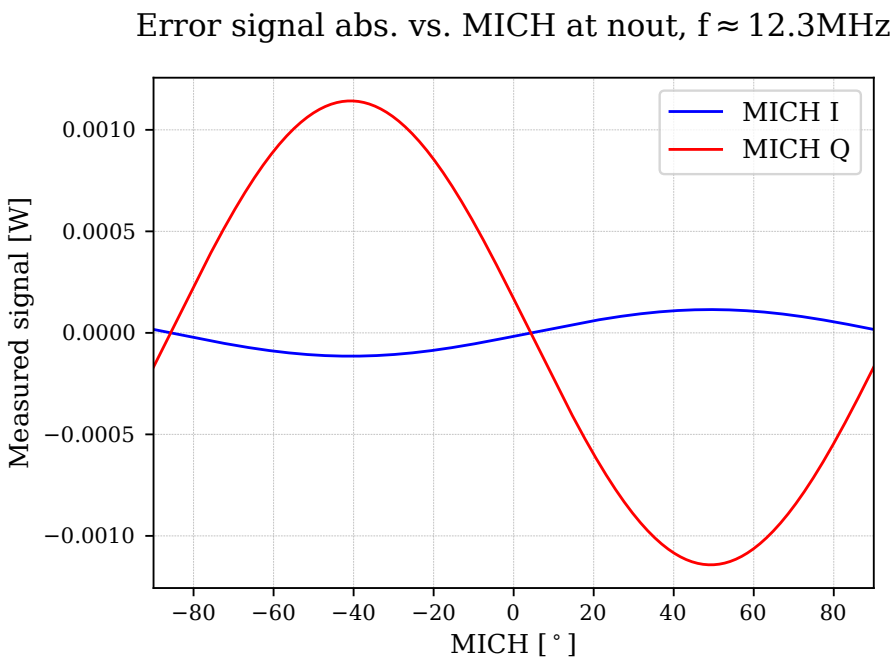

FIGURE 3.19: MICH error signal at ASY port.

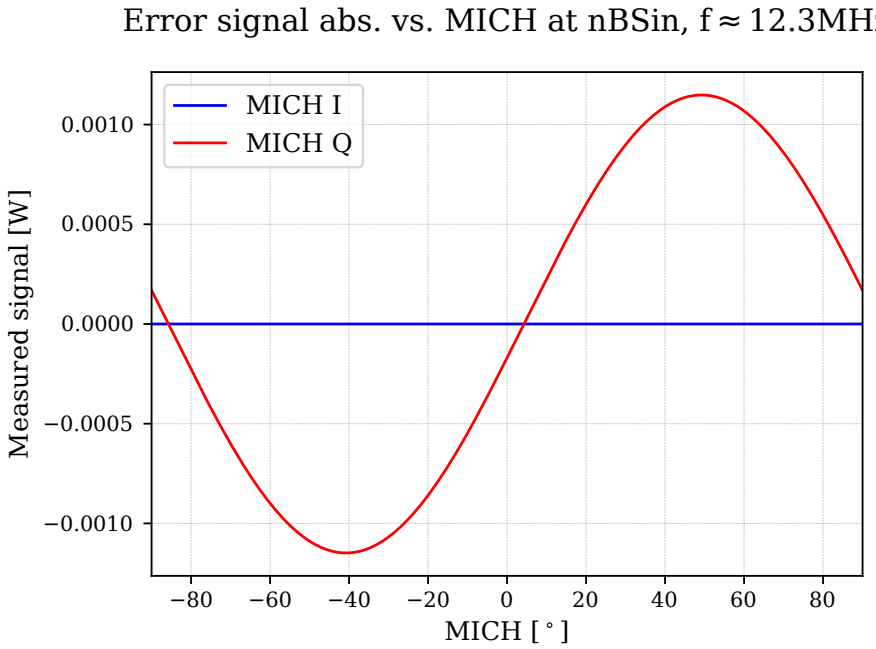

FIGURE 3.20: MICH error signal at REF port.

The sensing matrix can alternatively be represented in a radar plot. This was done following the examples in [22, Chpt. A]. Such a plot contains a vector per DOF and detection port. The angle of the vector shows the phase of the response of an error signal. If the vectors are perpendicular, a phase can be found at which the responses are perfectly separated. If they are not, they will have some mixing which could be minimised by an optimal choice in demodulation phase. The radar plots for the REFL port and ASY port are displayed in fig. 3.21. The matrix elements are shown in a polar plane where I-phase corresponds with 0° and Q-phase with 90°. Since at both ports either CARM or DARM dominates the signal, the other DOFs have been multiplied by some factor to make them visible. These radar plot can thus not be used to compare the relative magnitudes, but they do provide insight into the choice of the demodulation phase. Most noticeably they show that the CARM and MICH responses always differ by 90°, while also revealing the MICH and DARM response are not exactly in-phase with each other at the ASY port. The former indicates it still makes sense to try to measure the MICH response at the REFL port. The latter is only the case after adding the Michelson offset, but the effect is small nonetheless.

Finally, the sensitivity matrix can now also be found. The simulated shot-noises agree very well with the theoretical formula.

$$\delta P_{AC,shot,REF,sim} = 3.262 \times 10^{-10} \frac{\mathrm{W}}{\sqrt{\mathrm{Hz}}}, \tag{3.83}$$

$$\delta P_{AC,shot,ASY,sim} = 2.412 \times 10^{-11} \frac{\mathrm{W}}{\sqrt{\mathrm{Hz}}}. \tag{3.84}$$

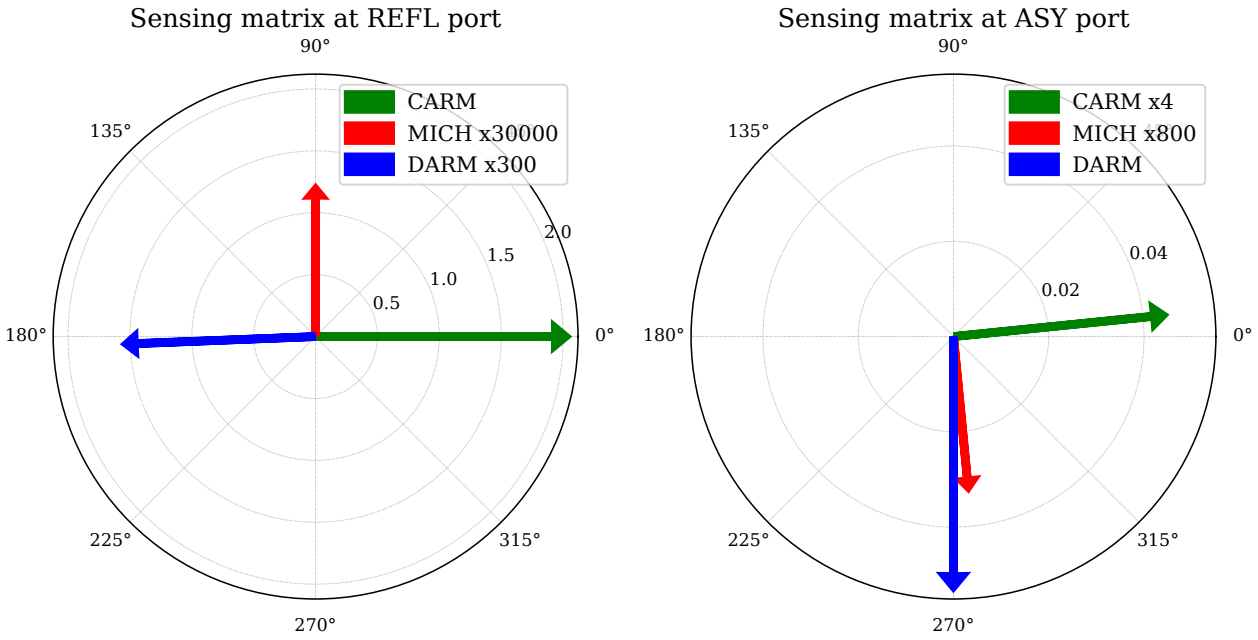

FIGURE 3.21: Radar plots showing the angular distribution of the matrix elements at (a) the REFL port and (b) the ASY port.

The sensitivity matrix in $\mathrm{m}/\sqrt{\mathrm{Hz}}$ becomes

$$\mathbf{S}_{simulation} = \begin{bmatrix} 3.4770 \times 10^{-19} & 1.1760 \times 10^{-10} & 1.3798 \times 10^{-16} \\ 4.2745 \times 10^{-15} & 1.7714 \times 10^{-14} & 2.5438 \times 10^{-15} \\ 4.7224 \times 10^{-18} & 1.3519 \times 10^{-14} & 3.4172 \times 10^{-15} \\ 4.3521 \times 10^{-17} & 1.3150 \times 10^{-15} & 9.8984 \times 10^{-19} \end{bmatrix}. \tag{3.85}$$

When taking sensitivity into consideration, ASY Q should be regarded as a serious candidate for the readout of MICH as well. Its sensitivity is an order of magnitude better than the REF Q signal. A minimum required sensitivity is given in sec. 3.2.7. The ASY Q signal is dominated by the DARM signal, but in section 3.2.6 it will be shown that in practice this might not form a big issue. DARM can independently be controlled, after which only the MICH signal would remain.

3.2.6 Realistic experimental implementation

How the error signals are used in the experiment is slightly outside of the scope of this thesis, but the concept can be summarised as follows. The sensing matrix equation 3.4 is inverted, to show which DOFs are off-resonance based on which error signals deviate from the locked signal:

$$\vec{\Delta} = \mathbf{M}^{-1}\vec{S}_{demod} \tag{3.86}$$

These DOFs can then be corrected by actuating on the laser frequency or the mirror positions. The latter is done through coil-magnets implemented like voice coils which accompany the mirror below the attenuator. These can produce a magnetic field that pushes or pulls a conductive element attached to the mirror [7, Chpt 6, 11]. This process works well in the region of deviations for which the error signals are approximately linear. That is true when the ITF is locked and the deviations are small.

However, bringing the ITF to its locked state is called lock acquisition and is a very non-trivial task, which would be a topic for an entirely new study. In this work only the control starting from the locked state is considered.

The situation becomes more complex when taking into account the frequency at which the DOF is changing. The noise transfer of shot-noise is frequency independent, but signal transfer generally is not. The optical gains that were determined in the previous section were done so by moving the mirror(s) by some distance, taking a measurement, and then moving the mirror(s) to the next position. The effective speed of this motion is therefore in fact zero, meaning the situation is equivalent to the limit of the signal frequency going to zero. For realistic signals with a frequency higher than zero, the dynamic behaviour of the cavity should be considered as well as that of the sensor and actuator [19, Chpt. 4]. The sensitivity would then no longer be just a number but in fact a frequency dependent function. To work this out for the longitudinal control of ETpf was outside the scope of this thesis, but it would be of value if done in the future.

The control scheme outlined previously in this chapter is based on the one that was worked out for Virgo and LIGO. As hinted in the preceding paragraph the real longitudinal stabilisation that was eventually implemented is much more complex. The rest of this section discusses some differences that improve the performance for Virgo and could be applied at ETpf as well.

CARM An important difference for Virgo specifically is the way the CARM DOF is controlled. Virgo applies an extra high-bandwidth (10 kHz) control loop called the Second Stage of Frequency Stabilization (SSFS) which actuates on the laser frequency. It turns out actuation on the frequency can happen at a much higher speed than actuating on the mirrors would. Hence, the CARM DOF can be controlled much faster than others. It follows that the level of CARM DOF mixing into other error signals, which was observed in the simulation, is not a significant concern once this control loop is active. This type of system will be implemented at ETpf as well. [12, Chpt. 2] [23]

DARM The DARM DOF can also be controlled using more recent methods. The addition of the Michelson offset enables DC detection (also called homodyne detection), which works well for DARM. This detection method is explained below. Virgo applies a similar offset as well, with about 8 mW reaching the dark port. For the parameters used in ETpf this is about 5 mW as shown in eq. 3.76. The difference with Virgo is that they apply the offset at the end mirrors and not at the BS, which is called a DARM offset instead [23].

DC detection uses the carrier signal directly instead of demodulating with some frequency. This is equivalent to demodulating at 0 MHz. Without an offset, the DC signal at the dark port would be symmetrical around the dark fringe. Any deviation would cause light to leak to the dark port but as the signal is symmetrical it would not be clear in which direction the mirrors should be moved to compensate. The problem is in fact the derivative being zero. If it isn't, linear control theory can be applied and the deviations can be compensated. This is exactly what adding the offset achieves. The concept is shown in fig. 3.22. Another advantage is that a reference signal of the carrier is available, instead of measuring w.r.t. zero [23].

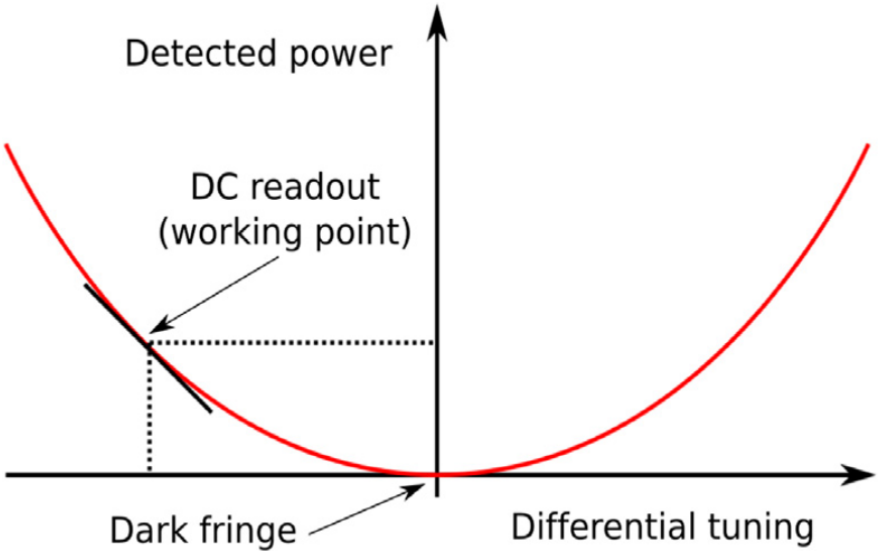

FIGURE 3.22: Plot showing the power variation at the detection port in response to a differential offset in the arms [23].

The simulated DARM signal at the output port of ETpf looks very similar to this illustration. It is shown in fig. 3.23, while the other two responses are shown in fig. 3.24. The gains and sensitivities measured are shown in table 3.3. The sensitivity is again limited to shot-noise only. Shot-noise on the measured carrier power is related to the AC shot-noise that was calculated before by $\delta P_{DC} = \sqrt{2}\delta P_{AC}$ [19]. It shows DC detection proves to be an extremely sensitive and uncontaminated readout channel for the DARM DOF. The acquired sensitivity is well below the projected noise budget shown in fig. 2.16. For Virgo, a stage of noise reduction is also applied, which reduces the coupling of MICH to DARM, making the readout of DARM even more accurate [23].

	DARM	CARM	MICH
Gain $[W/^\circ]$	-2.775	1.636×10^{-6}	-2.117×10^{-3}
Gain [normalized]	-1	5.89549×10^{-7}	-7.62883×10^{-4}
Sensitivity $\left[\frac{m}{\sqrt{Hz}}\right]$	2.64617×10^{-20}	4.48846×10^{-14}	3.46865×10^{-17}

TABLE 3.3: Summary of DC detection: gain and sensitivity

MICH At Virgo, the CARM DOF is being resolved with very high bandwidth by the SSFS (10 kHz), and DARM is resolved using DC detection at a higher bandwidth as well (70 Hz). This 'filters' the CARM and DARM contamination from the MICH control loop since it is slower (18 Hz). All other effects have faster actuation and will therefore already be controlled in a large capacity when the MICH control comes into action. At Virgo MICH is therefore read out at the REF Q port with no issues. Applying the same methods at ETpf is likely to yield successful results. [23]

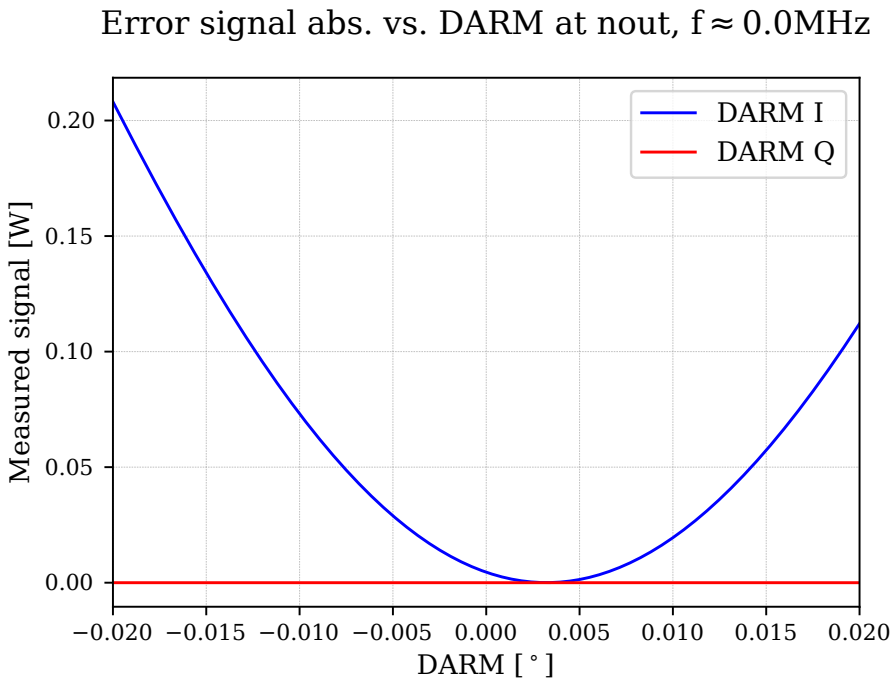

FIGURE 3.23: DARM DC response in the ASY port. The title mentions demodulating at 0 MHz, which gives the same result as not demodulating at all.

3.2.7 Motivation for global longitudinal control

After implementation of the Superattenuators, the residual motion of the TMs at Virgo is of the order of 1 μm RMS [23]. It is reasonable to assume the same will be true for ETpf. There are however several constraints that require precision that is multiple orders of magnitude greater. Some of these were outlined in [12, Chpt. 3] and adapted here. For CARM a limiting factor is that fluctuations must be at least an order of magnitude smaller than the recycling cavity resonance. Since ETpf will not contain a power recycling stage, the finesse of this 'imaginary' recycling cavity is simply $F_{rec} = 1$. CARM fluctuations are amplified by the arm cavities, so the condition becomes

$$\frac{2F}{\pi}\Delta L_+ < \frac{1}{10}\frac{\lambda}{4} \tag{3.87}$$

$$\implies \Delta L_+ < 4 \times 10^{-11} m \tag{3.88}$$

$$\approx 8 \times 10^{-3}\,\text{deg} \tag{3.89}$$

Note that this is only an upper bound, as other factors may pose more stringent requirements. DARM and MICH fluctuations are restricted by the coupling of laser amplitude noise to the Michelson offset. This effect is discussed in more detail in section 4.3. If DARM or MICH vary, the offset will vary as well which acts as a noise source that can be avoided by demanding strict longitudinal control. The variation of the offset in function of DARM and MICH variations can be found through

$$\Delta\phi_M\ [\text{rad}] = \frac{4\pi}{\lambda}\left(\Delta l_- + \frac{2F}{\pi}\Delta L_-\right), \tag{3.90}$$

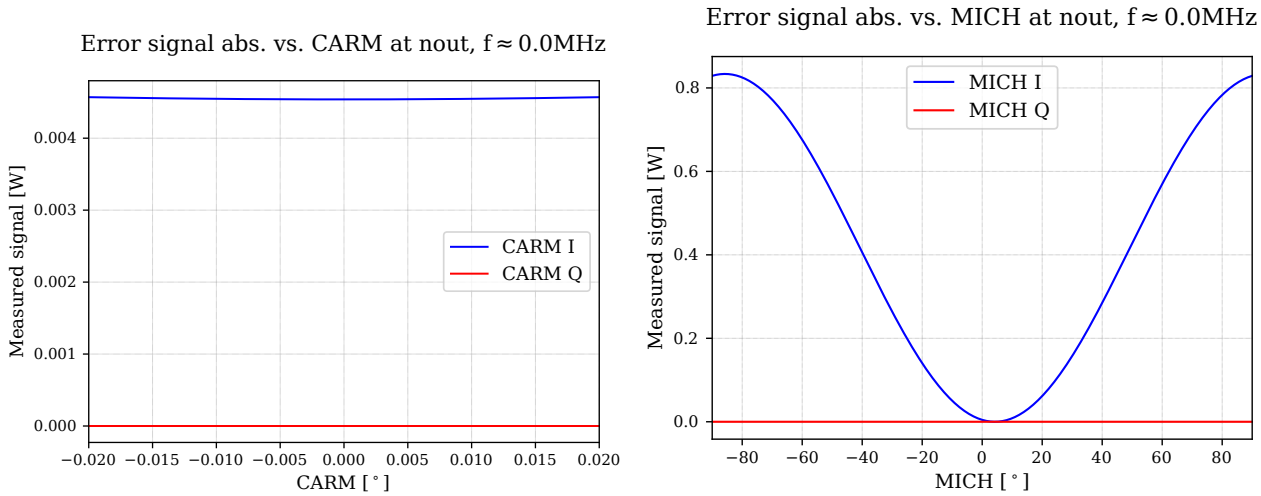

FIGURE 3.24: Other DC error signals at the output port. (a) CARM DC response in the ASY port. As calculated in sec. 2.2, this readout channel is insensitive to CARM. (b) MICH DC response in the ASY port. The response is similar to DARM in shape but a lot wider. This is due to the lack of amplification by the cavities.

where DARM effects are amplified by the arm cavities. The amplitude of phase noise due to such fluctuations is

$$\delta\phi = \frac{\widetilde{\delta P}}{P}\Delta\phi_M \tag{3.91}$$

These fluctuations are demanded to be at least smaller than the expected phase fluctuations caused by shot-noise at the ASY port. The latter are given by [19, Chpt. 2]

$$\frac{\delta P_{DC}}{P_{DC}} = \sqrt{\frac{2hc}{\eta\lambda P_{DC}}} \approx 8.1\times10^{-9}\frac{\text{rad}}{\sqrt{Hz}} \tag{3.92}$$

Combining these results produces the condition given by

$$\delta\phi < \sqrt{\frac{2hc}{\eta\lambda P_{DC}}} \tag{3.93}$$

$$\implies \Delta l_- + \frac{2F}{\pi}\Delta L_- < \frac{\frac{\lambda}{4\pi}\sqrt{\frac{2hc}{\eta\lambda P_{DC}}}}{\frac{\widetilde{\delta P}}{P}}. \tag{3.94}$$

The values of the parameters in this condition are shown below. The efficiency is no longer assumed to be unity but rather a more realistic value of 0.78. The size of average power fluctuations at ETpf is

taken from figure 4.10. The goal is to produce an order-of-magnitude estimate.

$$\frac{\delta P}{P} \approx 10^{-6} \frac{1}{\sqrt{\text{Hz}}}, \tag{3.95}$$
$$\eta = 0.78, \tag{3.96}$$
$$\lambda = 1550\,\text{nm}, \tag{3.97}$$
$$P_{DC} \approx 5\,\text{mW}, \tag{3.98}$$
$$h = 6.62607015 \cdot 10^{-34}\,\text{J} \cdot \text{s}. \tag{3.99}$$

Filling these into eq. 3.93 and demanding that both DARM and MICH fluctuations separately fulfil the condition gives

$$\Delta l_- < \frac{\frac{\lambda}{4\pi}\sqrt{\frac{2hc}{\eta\lambda P_{DC}}}}{\widetilde{\frac{\delta P}{P}}} \tag{3.100}$$
$$< 1 \times 10^{-9}\ \text{m RMS} \tag{3.101}$$
$$\approx 0.5\,\text{deg}, \tag{3.102}$$
$$\Delta L_- < \frac{\pi}{2F} \frac{\frac{\lambda}{4\pi}\sqrt{\frac{2hc}{\eta\lambda P_{DC}}}}{\widetilde{\frac{\delta P}{P}}} \tag{3.103}$$
$$< 8 \times 10^{-13}\ \text{m RMS} \tag{3.104}$$
$$\approx 4 \times 10^{-4}\,\text{deg}. \tag{3.105}$$

In conclusion, all three DOFs require precision that is multiple orders of magnitude below the residual mirror motion. These are only upper limits, for example at Virgo DARM is even controlled with precision below 10^{-16} m RMS [23, Chpt. 2]. This indicates the importance of longitudinal control, as the detector would not be functional without it. The strive for higher finesse and lower noise has made such control systems an unavoidable feature.

Chapter 4

Laser frequency & amplitude noise

The results in this section are based on work started by dr. Aaron Jones, dr. Phil Jones and dr. Teng Zhang. Their goal was to characterise how certain components and parameters of ETpf influence the transfer of laser frequency noise to the detector output. Any laser will have some inherent fluctuations on its frequency, and if they are large these will occupy some place within the noise budget. Frequency noise can be suppressed and their calculations make predictions on what suppression factors will be needed for this noise to be below the existing noise budget shown in fig 2.16. In this chapter some of their calculations will be repeated/updated and FMs will be added as well. The code written for the simulations in this chapter is based on code authored by dr. Aaron Jones. The same treatment will then be applied for laser amplitude noise.

4.1 Etalon effect of the input mirror

In a lot of the simulations in this and other works, mirrors are assumed to be infinitely thin. In reality they are not, and the light experiences internal reflections inside the mirror as a result. This becomes important when considering for example the IM of the arm cavities, since it changes the effective reflectance and transmittance of the IM. This is referred to as the etalon effect. As the effect is dependent on the microscopic tuning of the mirror thickness, it might not be the same for the x- and y-IMs. That would introduce an asymmetry in the finesses of the two cavities for example. This could cause changes in noise transfer and the amount of light reaching the ASY port, which is referred to as a contrast defect. This will be of importance when researching the noise contribution of having mirrors with finite thickness the following sections and is therefore treated first. The idea for investigating this and help with simulations came from dr. Teng Zhang of Maastricht University.

A realistic IM can be modelled by creating two reflective surfaces with a mirror-like space between them. The surface facing the BS is called the anti-reflective side (AR), the space in between is approximately modelled after silicon and the surface facing the cavity is the highly-reflective side (HR). Together this is now called the compound mirror, similar to how the arm cavities and later the whole ITF were modelled as a single compound mirror in the previous chapter. The standard parameters that were used are given in table 4.1.

The reflectance of this compound mirror is predicted in eq. 2.14. This system cannot be considered

Parameter	Value
T_{AR}	0.99957
L_{AR}	3×10^{-5}
R_{AR}	1×10^{-4}
$n_{compound}$	3.5
Mirror thickness	8 *cm*
T_{HR}	0.003056
L_{HR}	5×10^{-5}
R_{HR}	0.996889

TABLE 4.1: Parameters for the compound mirrors used in simulation, taken from [24, App. A] and [14, Chpt. 6]

lossless, meaning the losses have to be included in the formula. Since the equation is not symmetric for the IM and EM, the roles must be filled in carefully. The more important effect is how the compound mirror behaves towards the inside of the cavity and not w.r.t. the light coming from the BS. The HR side is therefore the IM and the AR side is the EM. The equation becomes

$$r_{eff}(\phi) = \frac{r_{HR} - r_{AR}\exp(2i\phi) - L_{HR}r_{AR}\exp(2i\phi)}{1 - r_{HR}r_{AR}\exp(2i\phi)}. \tag{4.1}$$

Here ϕ is the microscopic tuning of the AR surface. This is first tested in simulation to confirm the validity. The compound mirror is placed in front of a laser source and the effective reflectance R_{eff} is measured by comparing the returning with the incoming light. A loop is then made over R_{AR} and the result is plotted in fig. 4.1 for various tunings. It turns out that at a tuning of 0° results in a decrease in reflectance of the IM. For 45° the reflectance stays approximately constant. At a tuning of 90° the reflectance increases with the AR reflectance. For $R_{AR} = 0$ the effective reflectance becomes R_{HR}.

Now the attention should be drawn to the radius of curvature (ROC) of the AR surface. Until this point it was set to 14.5 m which matches the HR surface of the IM and EM [14, Chpt. 6]. A more realistic value however would be 9 m as investigated in [24]. This value collimates the exiting beam towards the folding mirrors. Inside the mirror it forms an imperfection however. In [25, Chpt. 5] it is outlined how the formula for r_{eff} would be altered to include this ROC mismatch. Light from the fundamental TEM_{00} mode is scattered into higher order modes because of the imperfection, but it can also couple back into the fundamental mode. The equation becomes:

$$r_{eff}(\phi) = \frac{r_{HR} - |k_{0000}|r_{AR}\exp(2i\phi) - |k_{0000}|L_{HR}r_{AR}\exp(2i\phi)}{1 - |k_{0000}|r_{HR}r_{AR}\exp(2i\phi)}. \tag{4.2}$$

The factor k_{0000} adjusts for the higher order modes coupling back to the fundamental one. The calculation of this factor is shown in [25, Chpt. 5]. For ETpf parameters this results in a value of about $|k_{0000}| = 0.564$. To see this effect in simulation the 'maxtem' should be increased to about $n = 8$, meaning higher-order modes up to the eighth order are simulated. For higher maxtem no further changes were seen, therefore using a higher value would be unnecessary. The result is shown in fig. 4.2. The trends are the same as for a ROC of 14.5 m, but the maximal deviation from the starting point is smaller. Again, the theory and simulation agree well, showing this is a good theoretical model for the compound mirror. From this point on the AR ROC will be set to 9 m.

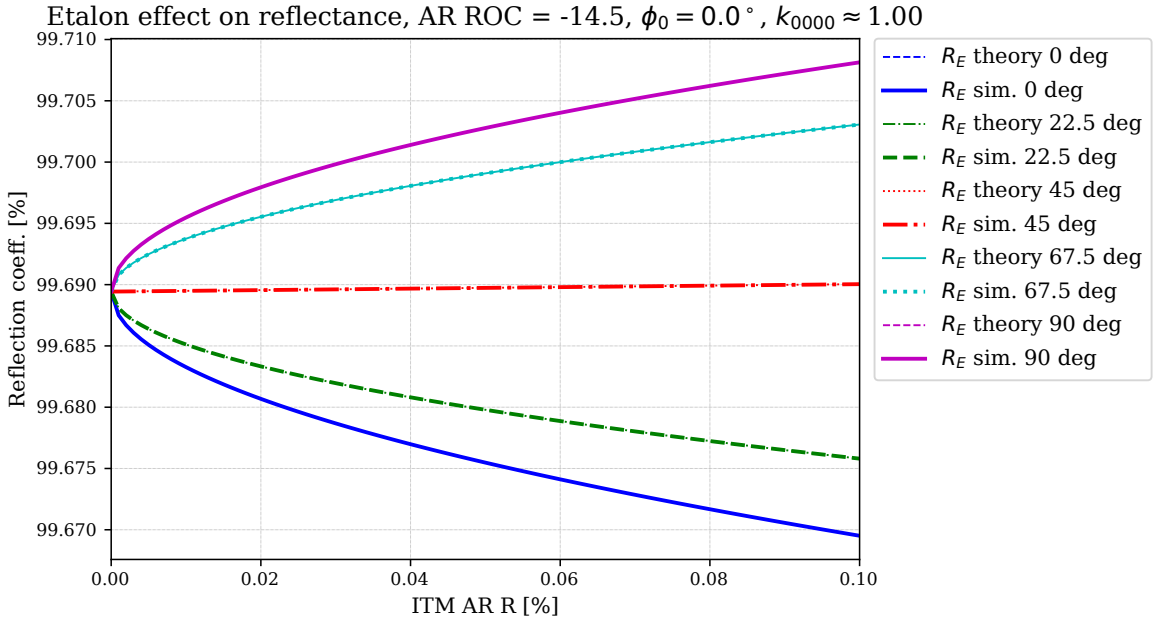

FIGURE 4.1: Simulation and theoretical evolution of R_{eff} agree very well. The theoretical and simulated reflectance is plotted for tunings varying from 0° to 90°. ϕ_0 is referring to potentially adding an initial phase to the theoretical formula (not necessary here). The negative radius of curvature (ROC) ensures the curvature is aimed towards the inside of the cavity.

4.2 Laser frequency noise

In this chapter the noise sources described in section 2.5 will be taken from a custom entry for the 1550 nm interferometer of ETpf for the pygwinc package[1]. The version used was last updated in May of 2022.

If the interferometer is run perfectly at the dark fringe, any fluctuations in the laser frequency cancel perfectly at the ASY port. As referenced in sec. 2.4, the detector is run at a Michelson offset (DC offset) of 2.114°, meaning a constant amount of light reaches the dark port. This forms the first of three cases that will be covered. The second case also introduces the Schnupp asymmetry of 10 cm in the x-arm. Finally, the third case will add compound mirrors as discussed in the previous section. This causes not only an imbalance in the R-value of the x- and y-arm ITM, but also higher order effects experienced by the light inside the compound mirror. The third case will consider various tunings for the x-arm compound mirror, while the y-arm will be kept at zero tuning (on resonance). These three situations will all increase the amount of laser noise that is transferred to the output port. This will generally be frequency dependent. To summarise the three cases:

- Case 1: DC offset
- Case 2: DC offset + Schnupp asymmetry
- Case 3: DC offset + Schnupp asymmetry + compound mirrors

[1] https://git.ligo.org/gwinc/pygwinc/-/tree/master/

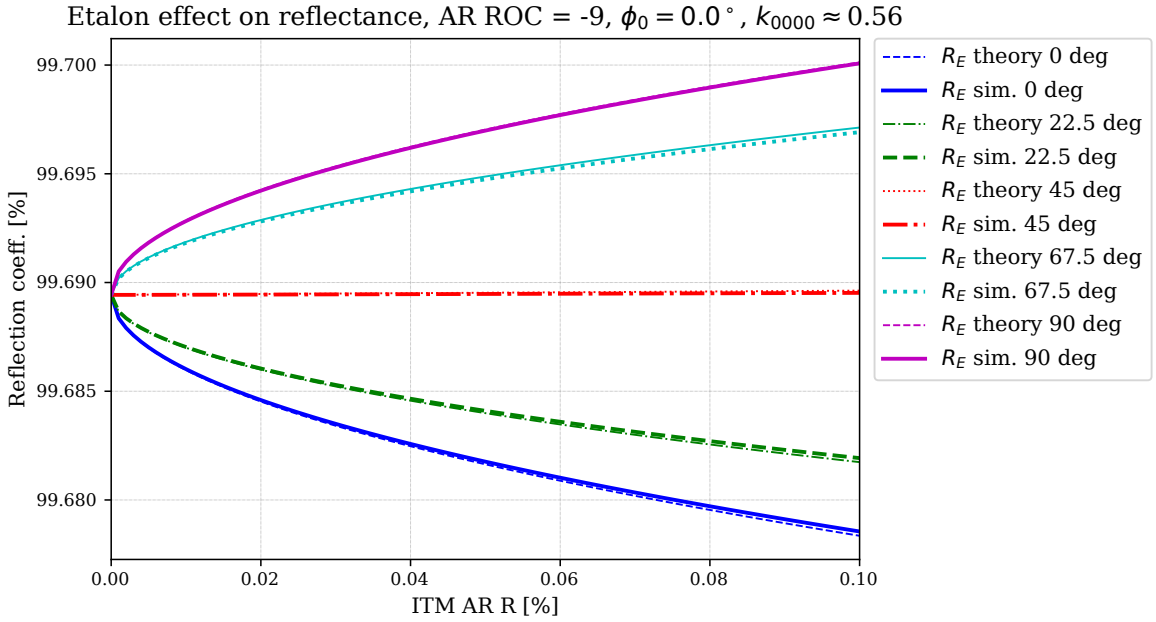

FIGURE 4.2: r_{eff} for an AR ROC of 9 m. For this value of k_{0000}, the simulation agrees well with the theory. The theoretical and simulated reflectance is plotted for tunings varying from 0° to 90°.

The exact transfer functions can easily be simulated in FINESSE. It is done by adding a noise of unitary amplitude to the laser frequency, setting a detector at the output port that demodulates at the frequency of the noise and then looping over the frequency of the noise from 10 Hz to 300 kHz. The demodulation isolates the noise from the carrier, however the EOM used for longitudinal control should be turned off so it does not show up in the demodulated signal. This generates the frequency noise transfer function $H_n(f)$ $\left[\frac{\mathrm{W}}{\mathrm{Hz}}\right]$. To convert to sensitivities at a later point the signal transfer function should also be measured. It will be called $H_s(f)$ $\left[\frac{\mathrm{W}}{\mathrm{m}}\right]$. It is found in exactly the same way, however now instead of noise on the laser a differential signal is generated inside the cavity. Lastly an estimate on the real laser noise should be used to scale the sensitivity. The input system that is proposed for ETpf is the combination of an Orion laser source, a booster optical amplifier (BOA) and finally a 10 W Boostik amplifier, resulting in an 11W output. The corresponding noise curve is found in [26, Chpt. 3] and recreated in fig. 4.3. It shows the amplitude spectral density of the laser frequency noise $N_f(f)$.

All this information can be combined into a limit on the sensitivity given by:

$$S_f(f)\left[\frac{\mathrm{m}}{\sqrt{\mathrm{Hz}}}\right] = \frac{N_f(f)|H_n(f)|}{|H_s(f)|}\left[\frac{\frac{\mathrm{Hz}}{\sqrt{\mathrm{Hz}}}\cdot\frac{\mathrm{W}}{\mathrm{Hz}}}{\frac{\mathrm{W}}{\mathrm{m}}}\right]. \tag{4.3}$$

This indicates the size of noise, meaning it is a lower limit on the sensitivity of the detector. It is also referred to as the noise spectrum. For reference, ETpf has a target sensitivity for its first phase of around $1 \times 10^{-18}\mathrm{m}/\sqrt{\mathrm{Hz}}$, which can also be seen in figure 2.16. The first step in the construction of the sensitivity limit is simulating all the transfer functions involved. Only for this part a fourth case was added as suggested by dr. Teng Zhang. For compatibility reasons this was called case 2.5. It describes the effect of the R-imbalance of the two IMs, without introducing the compound mirrors yet. It therefore does not include the noise transfer implications of having mirrors with a thickness.

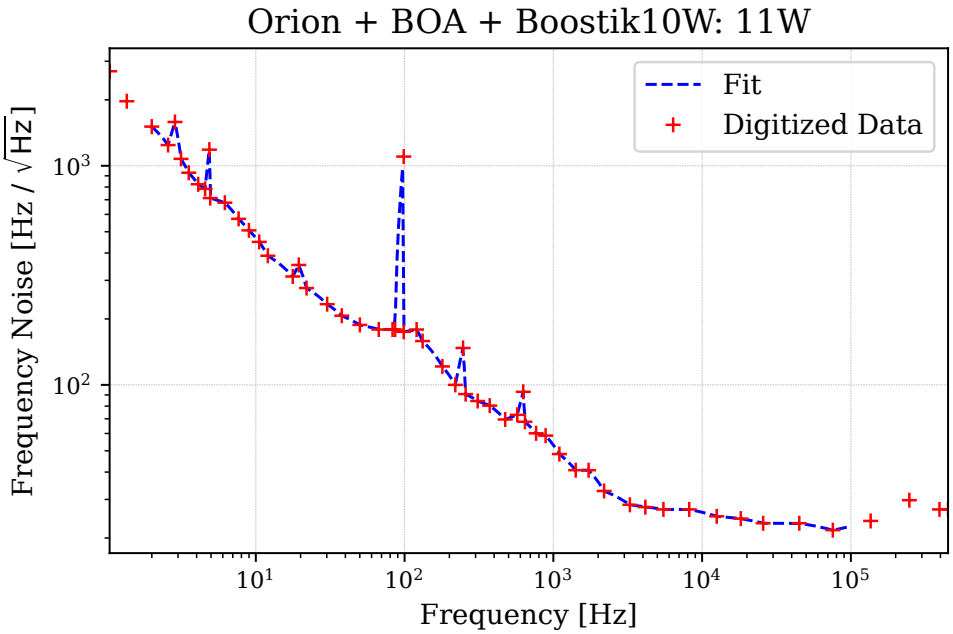

FIGURE 4.3: Frequency noise used as input for sensitivity calculations, taken from [26, Chpt. 3] using Web Plot digitizer[2].

The simulation contains infinitely thin mirrors with an adjusted reflectance:

$$R_{\text{IM, new}} = R_{eff}(R_{AR} = 0.01\%). \tag{4.4}$$

This means the new reflectance is equal to the reflectance of the compound mirror with an AR reflectance of 0.01%, which is realistic [24]. The transmission T is also adjusted s.t. $R+T+L=1$ with the loss remaining $L = 50$ ppm. The changes are only applied for the x-IM, meaning the y-IM does not change w.r.t. case 2. The effect will differ based on the microscopic tuning of the etalon. The three phases of $\phi = 0°$, $\phi = 45°$ and $\phi = 90°$ will be simulated. They respectively decrease, unalter and increase the x-IM's reflectance as shown in fig. 4.1. The values of reflectance and transmittance that were found in simulation are shown in table 4.2. For an AR reflectance of 0.01%, the mirror's effective reflectance varies by -34 ppm and $+34$ ppm for 0° and 90° respectively.

Tuning	$\phi = 0°$	$\phi = 45°$	$\phi = 90°$
$R_{\text{IM, new}}$	0.996860	0.996894	0.996928
$T_{\text{IM, new}}$	3090 ppm	3056 ppm	3022 ppm

TABLE 4.2: Adjusted reflectance of the IM to imitate the effect of a compound input mirror.

The resulting transfer functions are shown in figures 4.4, D.1 and D.2. It also shows the difference between having folding mirrors and not having them. For these plots, the transmittance of the FMs is set to an unrealistically high value: $T = 0.1$. This is only done to make the effect visible at this scale but does not represent a realistic prospect. At a later point it will be switched to an acceptable estimate of $T = 0.005$. The distinction between one and two x-FMs is negligible for realistic values of the transmission and is therefore not included.

[2] https://automeris.io/WebPlotDigitizer/

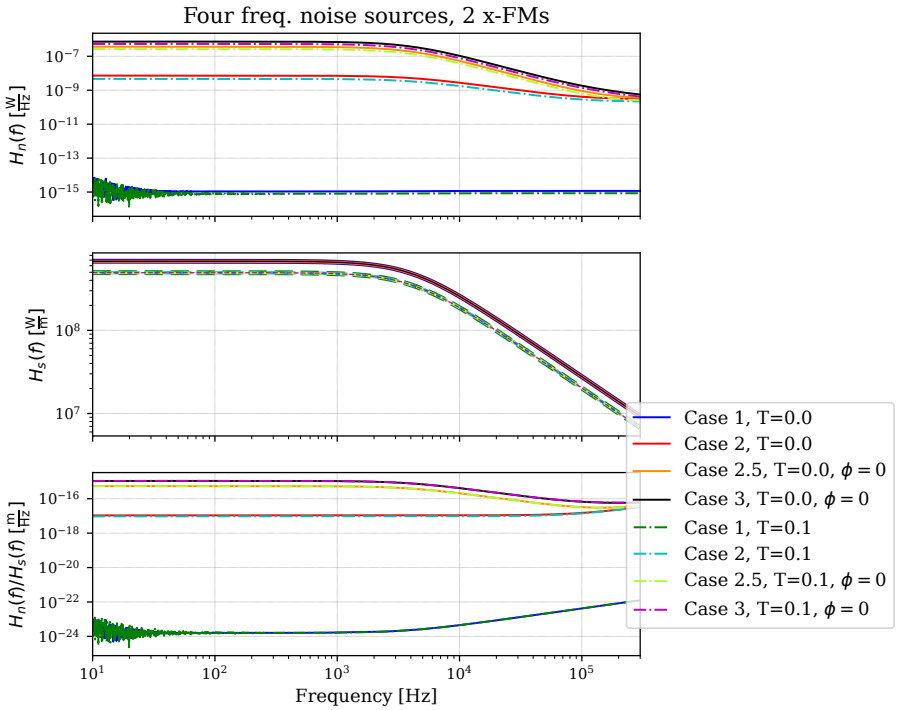

FIGURE 4.4: Frequency noise and signal transfer functions for two x-FMs with etalon tuning $\phi = 0°$. The four cases are plotted for folding mirror transmittance $T = 0$ and $T = 0.1$.

Noise transfer function From fig. 4.4, it is clear that relative to the other cases, the DC offset (case 1) only contributes a small amount to the noise transfer. The irregularities at low frequencies are attributed to radiation pressure effects. The Schnupp asymmetry (case 2) increases the noise transfer by a couple of orders of magnitude. In fact, the maximum noise has a power-law dependence on the Schnupp asymmetry, as shown in fig 4.5. On one hand, this would warrant lowering the value for Schnupp asymmetry. On the other hand, case 3 noise is often stronger by multiple orders, which would not be changed by lowering the Schnupp asymmetry. Secondly, the Schnupp asymmetry should be high enough for sidebands to sufficiently pass to the ASY port for usage in longitudinal control.

Next, it is clear that both $\phi = 0°$ and $\phi = 90°$ add about two orders of magnitude if only the R-imbalance is considered. As predicted $\phi = 45°$ does not change anything. When considering the final case with the full compound mirrors, some peculiar results arise. It turns out a compound mirror with $\phi = 0°$ and $\phi = 45°$ would both add about two orders of magnitude to the noise transfer. For $\phi = 90°$ however the effect of the R-imbalance is approximately cancelled out by the presence of the compound mirror. The resulting noise transfer is of the same order as case 2. In theory, the tuning of the etalon could therefore correct the contrast defect. It would however be very difficult to control the actual microscopic tuning of the etalon, therefore it is wise to continue working with the ”worst case” tuning of $\phi = 0°$. As of the 2020 design report [14, Chpt. 6], it was not yet decided whether to exploit or rather avoid the etalon effect, which is why this work assumes the effect is present in its maximal capacity.

The reason this is considered the worst case starts from also considering the compound mirror in the y-arm. The AR side is tuned to $\phi = 0°$, but it should not be forgotten that the HR side is tuned at 90° to preserve the dark-fringe condition at the ASY port. The y-arm thus experiences the effect that the

x-side would have at 90°, i.e. an increased reflectance. If the x-arm then simultaneously experiences reduced reflectance, the mismatch is the largest. This makes it the worst case when trying to achieve symmetry between the two arms.

Finally, it should be noted that adding the FMs slightly decreases the noise transfer function across the board. This is a result of generally less light reaching the BS and the output port.

Signal transfer function The signal transfer is not affected by the different cases. It is also clear that signal transfer is slightly reduced by the addition of the FMs. The cavity pole is found around 4.1 kHz.

The fraction H_n/H_s Since the effect caused by the FMs on the transfer functions is equal for the noise- and signal transfer functions, it cancels out in their fraction. The FMs will therefore not significantly influence the sensitivity limit. Any slight deviations are caused by the asymmetry in the x-and y-arm since they have respectively two and one FM. This becomes clearer in the plot in figure D.3 where the fraction already has been multiplied by $N_f(f)$. A somewhat surprising result is that the FMs slightly decrease the noise spectrum for case 2. In figure 4.6 a more realistic value for T is used, showing that the real FMs do not make a significant difference in simulation.

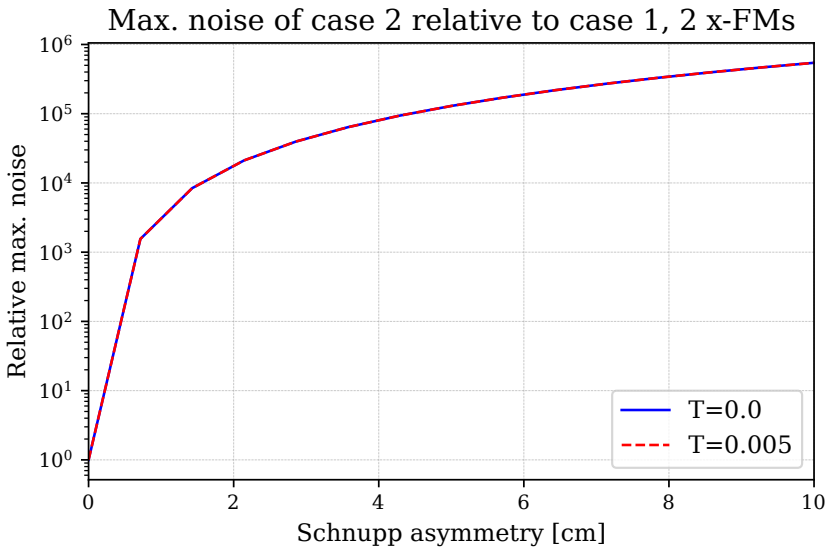

FIGURE 4.5: Maximum noise dependence on the Schnupp asymmetry relative to case 1. The result is plotted for folding mirror transmittance $T = 0$ and $T = 0.005$.

Subsequently, these displacement noise sources are placed within the context of some prominent noise sources for ETpf. The ones included in these plots are quantum noise, suspension thermal noise and coating brownian noise. The result is shown in fig. 4.7. It is clear that case 2 and 3 will need suppression before they would be small enough to fit below the currently outlined budget. Case 1 is already low enough to remain unchanged.

Figure 4.8 shows the suppression factor that would necessary. It is given by the ratio of the noise and the budget. It also contains two suggested suppressive control schemes. They consist of a DC gain

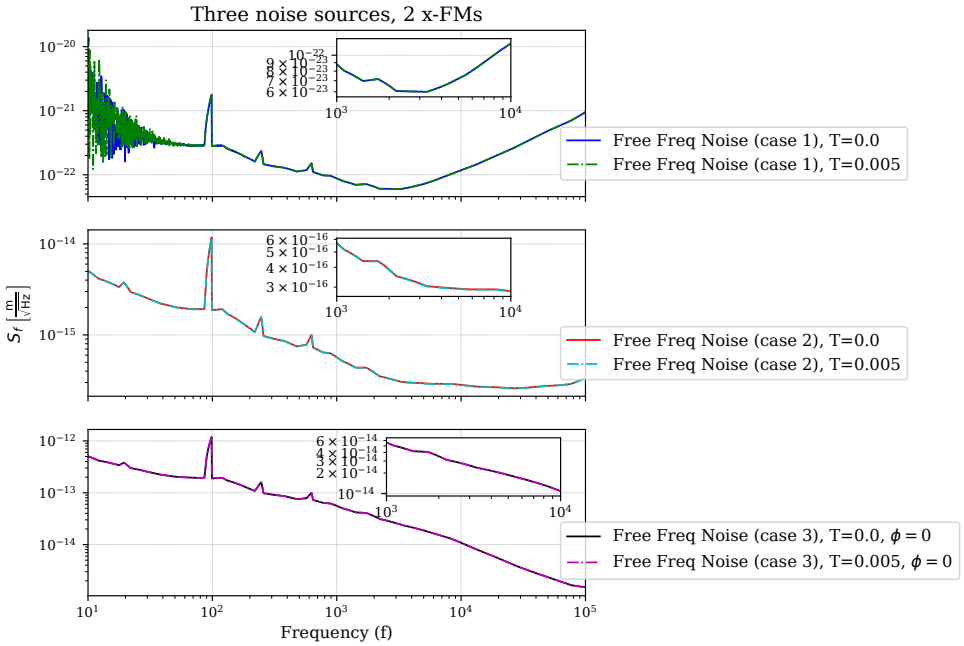

FIGURE 4.6: Frequency noise spectrum S_f before suppression with FM transmittance $T = 0$ and $T = 0.005$.

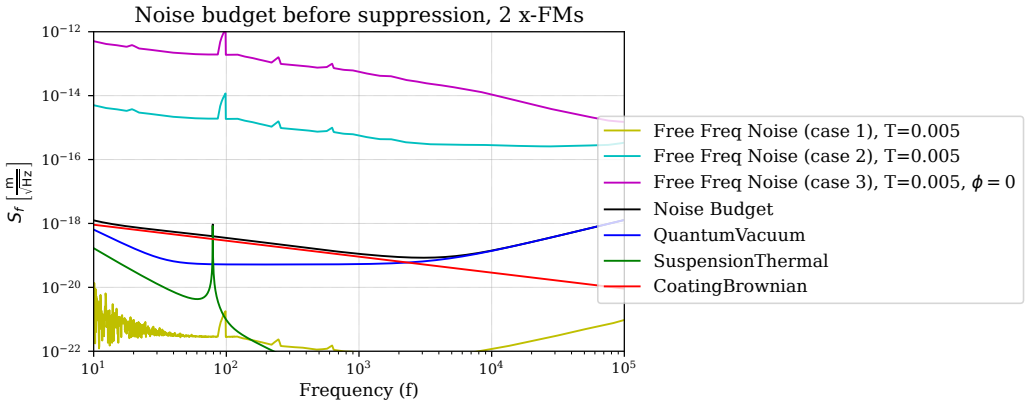

FIGURE 4.7: Frequency noise spectrum S_f before suppression within the noise budget.

and a f^2 low-pass filter with a cut-off frequency of 10 kHz. For case 2 and 3 the required gains are 10^6 and 10^7 respectively.

Finally, the budget is again plotted after the displacement noise of case 2 and 3 has been divided by the suggested suppression factor. It is shown in figure 4.9. This new noise is referred to as closed noise since it is part of a control loop. The new noise curves now fit below the line set by the budget. This means that adding the FMs into the system did not provide any major changes with respect to the work of dr. Aaron Jones. The method of suppression itself has not been studied in this work. A solution could be similar to the longitudinal control system for common-mode mirror movements. Frequency fluctuations affect the error signals the same way a common end-mirror fluctuation would, as explained in the beginning of sec. 3.2. Therefore, a system controlling the CARM DOF automatically suppresses laser frequency fluctuations as well. In fact, ETpf will likely implement a CARM control loop that actuates on the laser frequency itself.

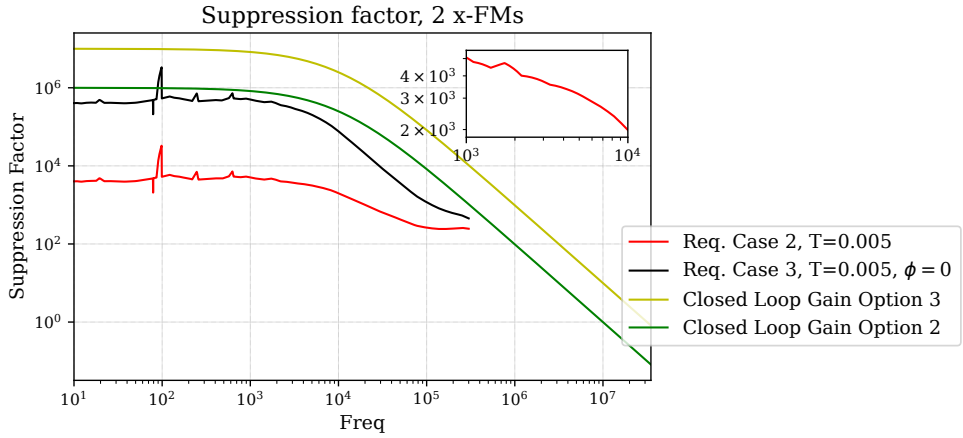

FIGURE 4.8: Suppression factor requirements and suggested control loop gains. The suppression factor is the fraction of the noise spectrum and the noise budget. The gain options have a DC gain of 10^6 for option 2 and 10^7 for option 3.

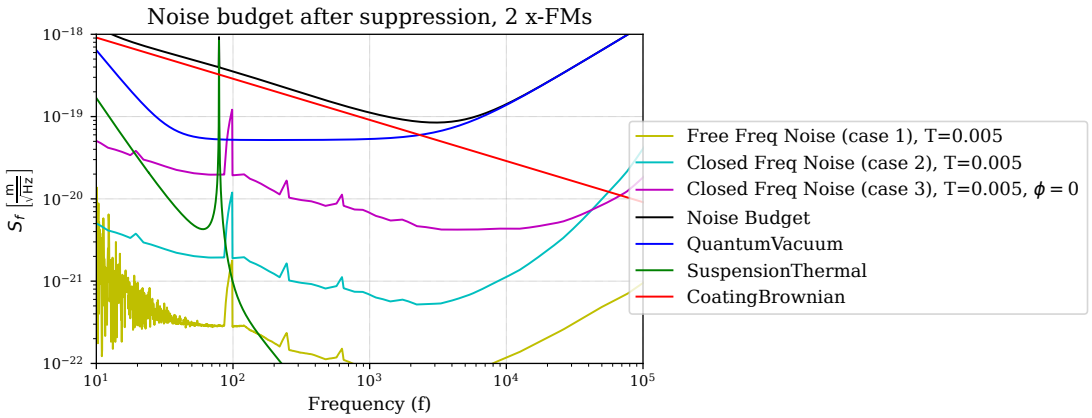

FIGURE 4.9: Noise budget after frequency noise suppression.

4.3 Laser amplitude noise

The treatment of laser amplitude noise will be entirely the same as for frequency noise, resulting again in a displacement noise curve that should fit below the noise budget. The way to achieve a sensitivity limit will contain the same building blocks. The units involved will be different however:

$$S_a(f)\left[\frac{\mathrm{m}}{\sqrt{\mathrm{Hz}}}\right] = \frac{N_a(f)|H_n(f)|}{|H_s(f)|}\left[\frac{\frac{\mathrm{W}}{\sqrt{\mathrm{Hz}}}\cdot\frac{\mathrm{W}}{\mathrm{W}}}{\frac{\mathrm{W}}{\mathrm{m}}}\right]. \tag{4.5}$$

Here $N_a(f)$ is the amplitude spectral density of the laser amplitude noise, H_n the amplitude noise transfer function and H_s the signal transfer function. H_s remains the same w.r.t. frequency noise, the amplitude noise transfer is now measured by adding noise to the laser amplitude. $N_a(f)$ is again taken from [26, Chpt. 3] and recreated in fig. 4.10. The curve chosen is again the combination of the Orion laser source, a booster optical amplifier (BOA) and finally a 10 W Boostik amplifier, resulting in an 11 W output.

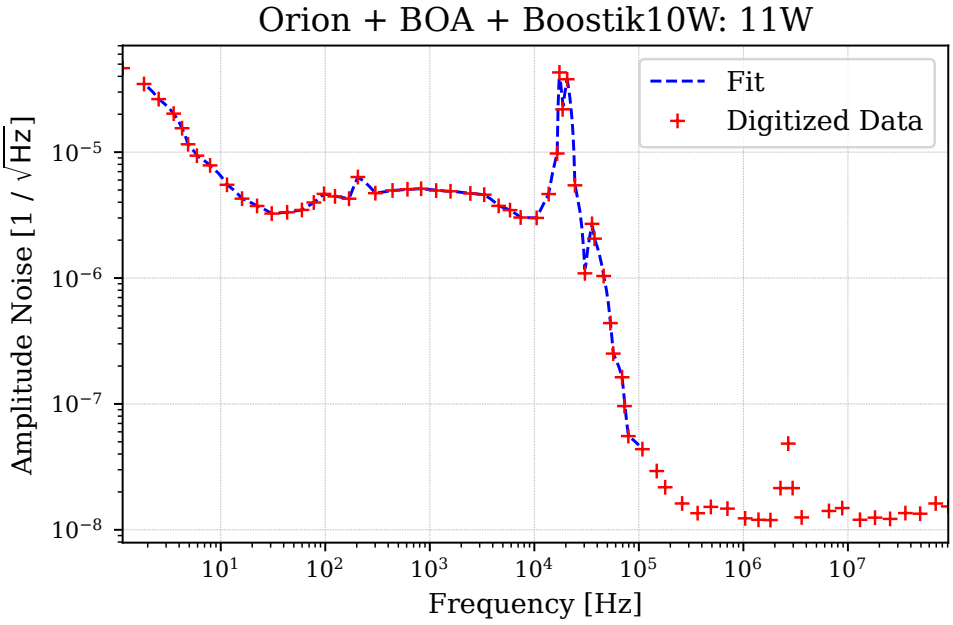

FIGURE 4.10: Amplitude noise used as input for sensitivity calculations, taken from [26, Chpt. 3] using Web Plot digitizer[3].

The transfer functions of amplitude noise are given in 4.11, D.4 and D.5. A significant difference with frequency noise is that the DC offset already contributes a large part of the total noise. The influence of the DC offset has been made clearer in fig. 4.12, showing the DC noise steeply increases as the offset goes up. Looking at the other noise cases, the difference only becomes clear at lower frequencies. It is clear that amplitude noise is thus very sensitive to the destructive interference condition. This can also be seen by observing two other features. Firstly, case 2.5 already contains a large part of the noise of case 3 with $\phi = 0°$. Secondly, for all noise cases, the asymmetry caused by the FMs with $T = 0.1$ adds about an order of magnitude of noise at low frequencies. To indicate this second point, a plot was also made with only one x-FM and thus symmetrical arms. It's shown in figure D.6. In this case the fraction of the two transfer functions is unaffected. It is worth noting that the influence of the asymmetric setup will be limited when using a realistic value of T.

A final noteworthy point is the behaviour for $\phi = 45°$ and $\phi = 90°$. The former again has case 2.5 being the same as case 2. For case 3 the noise at low frequencies increases, but for the region of 100-1000 Hz the noise transfer is actually slightly lower. At $\phi = 90°$ case 2.5 seems to display some sort of resonance decreasing low-frequency noise transfer. Case 3 is exactly the same as case 2 and 1. It should be restated that it is unlikely this phase would be controllable, meaning the worst case $\phi = 0°$ should be considered.

The plot in figure 4.13 shows the displacement noise of the three cases. Since the FM transmittance is kept to a realistic value, the influence of the FMs is only small. It can be seen to slightly increase the noise at low frequencies, but not at all at higher frequencies. At this point the noise is too high to fit the budget, as seen in fig. 4.14. It is expected that this could also be solved by applying a suppressive control loop. The DC gain necessary for this loop is only 10^5. This is shown in figure 4.15.

After applying this suppression to all three cases, they all fit the budget. This is shown in figure

[3] https://automeris.io/WebPlotDigitizer/

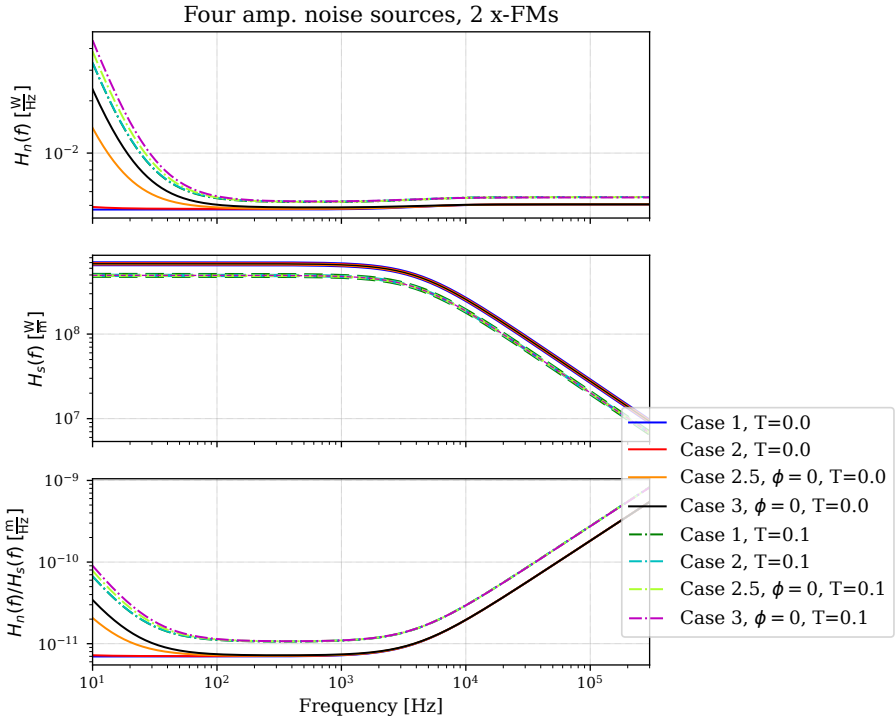

FIGURE 4.11: Amplitude noise and signal transfer functions for two x-FMs with etalon tuning $\phi = 0°$. The four cases are plotted for folding mirror transmittance $T = 0$ and $T = 0.005$.

4.16. The way in which the control loop should be implemented is not studied in this work. An important factor of suppression could be the control of the DARM and MICH DOFs however, since they contribute to the amplitude noise transfer of case 1. This was shown in section 3.2.7.

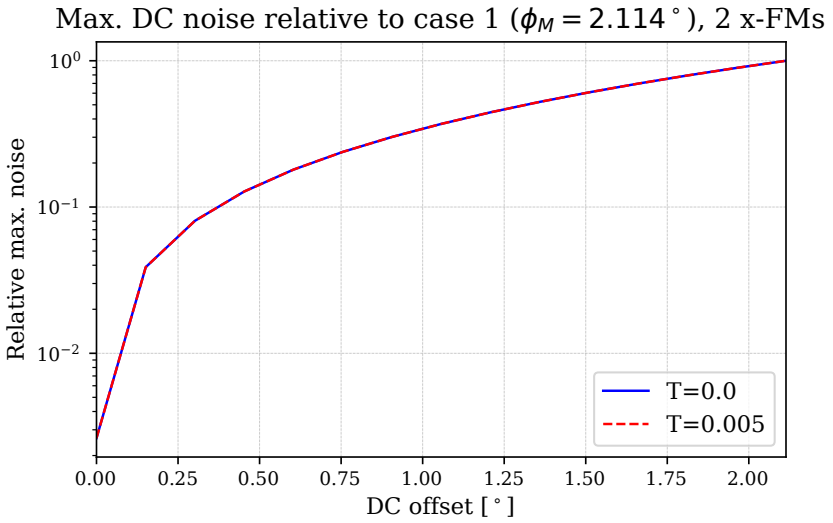

FIGURE 4.12: Maximum noise dependence on the DC offset relative to case 1. The result is plotted for folding mirror transmittance $T = 0$ and $T = 0.1$

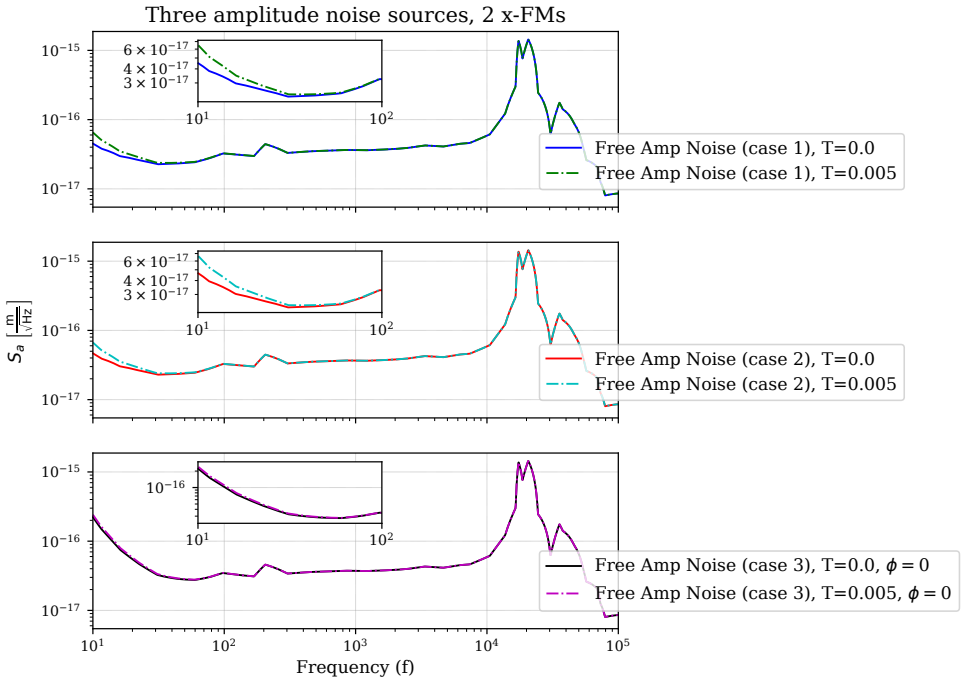

FIGURE 4.13: Amplitude noise spectrum S_a before suppression with FM transmittance $T = 0$ and $T = 0.005$.

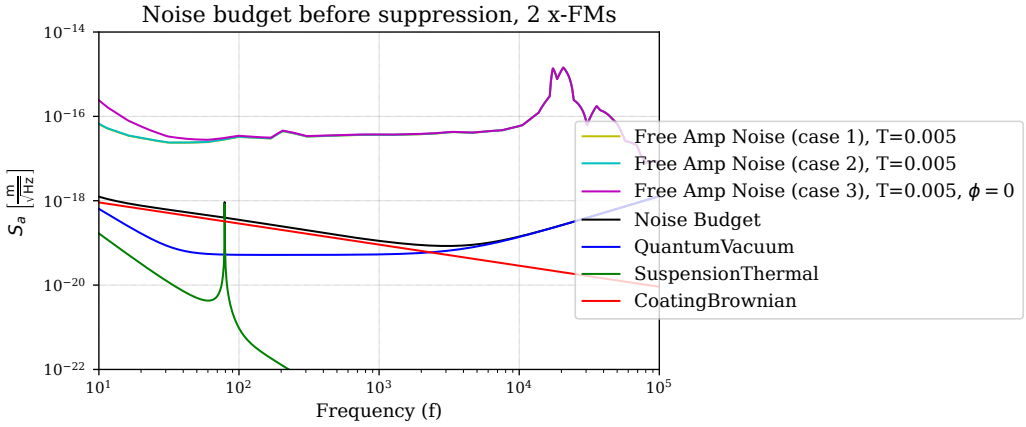

FIGURE 4.14: Amplitude noise spectrum S_a before suppression within the noise budget.

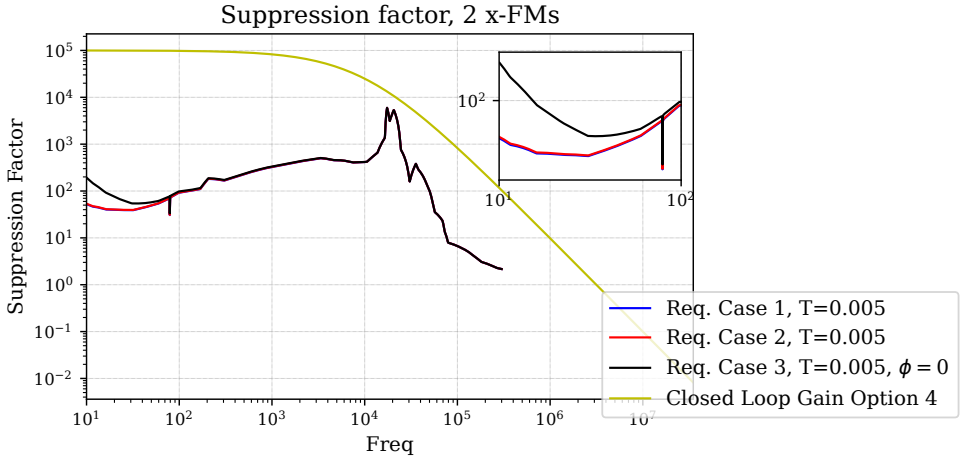

FIGURE 4.15: Suppression factor requirements and suggested control loop gains. The suppression factor is the fraction of the noise spectrum and the noise budget. The suggested control loop has a DC gain of 10^5.

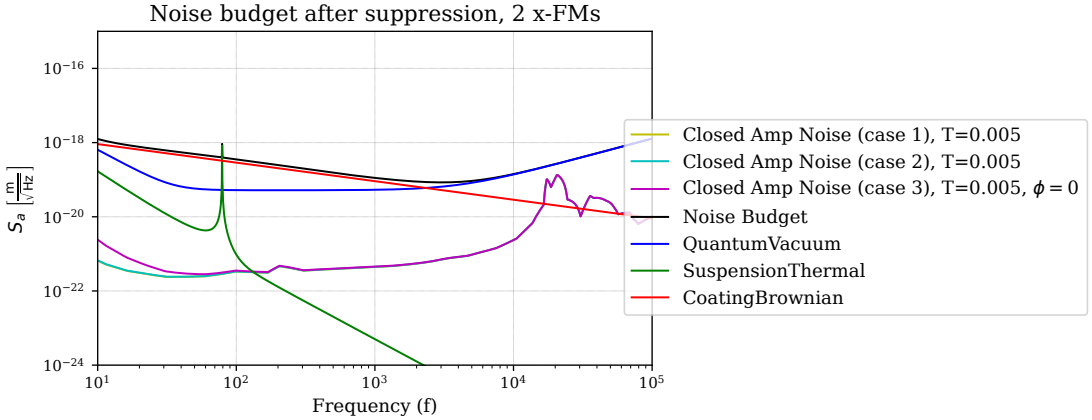

FIGURE 4.16: Noise budget after amplitude noise suppression.

Chapter 5

Conclusion

The Einstein Telescope pathfinder (ETpf) at Maastricht University is a research facility focused on exploring innovative techniques and methodologies to enhance the capabilities of future gravitational wave detectors. Such detectors will be able to observe gravitational waves arriving from sources in previously unreachable regions of space and time, possibly on an hourly basis. This will provide invaluable data which will be used to assess various physical theories and improve the understanding of GW sources. One of these future detectors is the Einstein Telescope (ET), which will implement major technological advancements w.r.t. the previous generation to improve its sensitivity to gravitational waves. ETpf plans to research and develop these modern technologies, which include cryogenic silicon test masses and the use of the 1550 nm and 2 μm wavelengths. The ETpf interferometer is currently transitioning from the simulation phase to the experimental phase. This thesis has contributed by performing FINESSE simulations regarding the longitudinal control of the interferometer and investigating laser-induced noise sources. This helps to pave the way for achieving the necessary sensitivity of ETpf and future GW detectors. Such simulations had not yet been performed for the specific layout of ETpf but will be important when the Pathfinder becomes operational.

In the second chapter, a solid theoretical foundation was established, delving into the concepts and theories crucial for understanding GWs and their detection methods. The working principle of gravitational interferometers was reviewed and an investigation was conducted into the implementation of arm-cavities and the application of phase-modulation techniques. Moreover, an overview of the ETpf experiment and its role in the broader context of the ET project was also given, highlighting its intended contributions to future observatories. A description of the various noise sources that will complicate the measurements was outlined, providing the necessary context for the later discussion of laser-induced noise sources.

The third chapter centred around the crucial topic of longitudinal control of the interferometer (ITF). A lot of experience surrounding this topic was already gathered by other experiments such as Virgo and LIGO. The control system of an ITF involves laser carrier modulation and extracting demodulated error signals at the demodulation phase associated with maximal optical gain. These techniques were successfully applied to the control of the ETpf arm cavities and the control of the whole interferometer. Cavity control was done using the light extracted behind folding mirrors positioned between the beam splitter and the arm cavities. Introducing these folding mirrors into the ETpf geometry and analysing their influence for the first time was an important achievement of this work. A shot-noise limited sensitivity in the order of 10^{-18} m$/\sqrt{\text{Hz}}$ was achieved for the cavity mirror positions. The three large-scale degrees of freedom of the ITF were also effectively controlled, with

sensitivities already close to the goal precision of 1×10^{-18} m$/\sqrt{\text{Hz}}$. For common arm movements (CARM) the shot-noise limited sensitivity achieved at the reflected port I-phase was already of the order 10^{-19} m$/\sqrt{\text{Hz}}$. The small arms of the ITF (MICH) could be controlled with sensitivities of 10^{-14} m$/\sqrt{\text{Hz}}$ and 10^{-15} m$/\sqrt{\text{Hz}}$ at the reflected and asymmetric port respectively, both measured at Q-phase. These readout channels were both dominated by response to other DOFs however. Differential arm movements (DARM) could be read out using the asymmetric Q-phase signal with a sensitivity in the order of 10^{-19} m$/\sqrt{\text{Hz}}$. Another option would be DC readout, where no demodulation is applied. The response is therefore determined directly from the carrier power, leading to a sensitivity of 10^{-20} m$/\sqrt{\text{Hz}}$ for DARM. To make the system more precise, advanced control loops and noise reduction techniques that are already present at Virgo should be implemented for ETpf as well. This would introduce a signal-frequency dependence and take into account the dynamic behaviour of all the components in the control loop. It would also be worthwhile to develop an algorithm for lock acquisition of the pathfinder, as this has currently not been investigated.

In the last chapter, laser frequency- and amplitude-induced noise were examined, addressing the challenges introduced by an imperfect optical input system. The impact of various design parameters on noise transfer and signal sensitivity were evaluated, including the DC offset, Schnupp asymmetry, and the etalon tuning of the input mirror of the cavity (IM). The etalon tuning refers to the microscopic tuning of the thickness of the IM that is no longer considered infinitely thin. This allows for internal reflections which influence the effective reflectance of the mirror. It was confirmed that the influence of the tuning in simulation matches the theoretical prediction. For an AR reflectance of 0.01%, the mirror's effective reflectance varies by ± 34 ppm, which significantly increases noise transfer if the x- and y-IM reflectance become mismatched. All these contributions to the noise transfer were considered as well as the expected noise spectral densities for ETpf when setting up the frequency- and amplitude noise spectra. The necessary gain factors for noise suppression were determined to fit these noise sources within the predefined budgets. Although no specific noise reduction technique is currently put forward, no major difficulties are expected with gains varying from 10^5 for amplitude noise to 10^7 for frequency noise. If a complete longitudinal control system is worked out in the future, it would be informative to check that they sufficiently suppress these noise sources.

In conclusion, this thesis has endeavoured to contribute to the advancement of GW detector technologies through the development of the ETpf. By working on key objectives related to longitudinal control and noise characterisation, valuable insights have been gained into how ETpf could be controlled. Potential challenges have been identified and addressed such as the asymmetry caused by the folding mirrors, the mixing of the other DOFs in the MICH error signal and the etalon effect of the IM. When necessary, effective strategies have been proposed to mitigate them based on simulation results. The insights gained from this research may not only address unresolved objectives of the ETpf project but may also guide future researchers working on similar subjects. This work forms a part of the global quest to ultimately unravelling the mysteries of the universe with unprecedented precision and clarity with 3G detectors.

Bibliography

[1] American Museum of Natural History. *Essay: Waiting for Gravity at LIGO*. URL: https://www.amnh.org/explore/videos/space/gravity-making-waves/essay-waiting-for-gravity-at-ligo.

[2] James B. Hartle. *Gravity: an introduction to Einstein's general relativity*. 1st. 2003. ISBN: 1269374508.

[3] M. Bailes et al. *Gravitational-wave physics and astronomy in the 2020s and 2030s*. May 2021. DOI: 10.1038/s42254-021-00303-8.

[4] ET steering committee. *Design Report Update 2020 for the Einstein Telescope*. 2020.

[5] Andreas Freise and Kenneth Strain. *Interferometer techniques for gravitational-wave detection*. 2010. DOI: 10.12942/lrr-2010-1.

[6] Sean M. Carroll. *Spacetime and Geometry*. Cambridge University Press, Aug. 2019. ISBN: 9781108488396. DOI: 10.1017/9781108770385. URL: https://www.cambridge.org/core/product/identifier/9781108770385/type/book.

[7] F. Acernese et al. "Advanced Virgo: a 2nd generation interferometric gravitational wave detector". In: (Aug. 2014). DOI: 10.1088/0264-9381/32/2/024001. URL: http://arxiv.org/abs/1408.3978.

[8] Charlotte Bond et al. *Interferometer techniques for gravitational-wave detection*. Dec. 2016. DOI: 10.1007/s41114-016-0002-8.

[9] GWoptics. *Resonance*. URL: http://www.gwoptics.org/learn/02_Plane_waves/01_Fabry_Perot_cavity/01_Resonance.php.

[10] GWoptics. *Impedance matched*. URL: http://www.gwoptics.org/learn/02_Plane_waves/01_Fabry_Perot_cavity/02_Impedance_matched.php.

[11] Andrei Utina. *Finesse simulation of arm-cavity and IMC HOMs*. URL: https://etpathfinder.maastrichtuniversity.nl/finesse-simulation-of-arm-cavity-and-imc-homs/.

[12] Francesco Fidecaro, Matteo Barsuglia, and Lisa Barsotti. *The control of the Virgo interferometer for gravitational wave detection*. 2006.

[13] Gerhard Heinzel. *Advanced optical techniques for laser-interferometric gravitational-wave detectors*. 1999.

[14] The Etpathfinder Team. *ETpathfinder DESIGN REPORT*. 2020. URL: www.ETpathfinder.eu.

[15] Samuel Rowlinson et al. "Feasibility study of beam-expanding telescopes in the interferometer arms for the Einstein Telescope". In: (2020).

[16] A. Utina et al. “ETpathfinder: a cryogenic testbed for interferometric gravitational-wave detectors”. In: *Classical and Quantum Gravity* 39 (21 Nov. 2022). ISSN: 13616382. DOI: 10.1088/1361-6382/ac8fdb.

[17] Amy E Turner et al. *Mechanical Loss and Deposition of Mirror Coatings on Silica*.

[18] Andreas Freise. *Frequency domain INterferomEter Simulation SoftwarE: manual*. 2014. URL: http://www.gwoptics.org/finesse.

[19] Bas Swinkels. *Requirements on sensing noise for the Pound-Drever-Hall technique for the lock of the arm-cavities*. 2012.

[20] Matthew Evans. “Lock Acquisition in Resonant Optical Interferometers”. 2001.

[21] M. Mantovani and A. Freise. “Evaluating mirror alignment systems using the optical sensing matrix”. In: *Journal of Physics: Conference Series* 122 (2008). ISSN: 17426596. DOI: 10.1088/1742-6596/122/1/012026.

[22] Kiwamu Izumi. *Multi-Color Interferometry for Lock Acquisition of Laser Interferometric Gravitational wave Detectors*. 2012.

[23] F. Acernese et al. “The advanced Virgo longitudinal control system for the O2 observing run”. In: *Astroparticle Physics* 116 (Mar. 2020). ISSN: 09276505. DOI: 10.1016/j.astropartphys.2019.07.005.

[24] Annabel Wolf, Stefan Hild, and Sebastian Steinlechner. *Optical System Design of the Einstein Telescope Pathfinder*. Maastricht University, 2020.

[25] S. Hild et al. “Using the etalon effect for in-situ balancing of the Advanced Virgo arm cavities”. In: (July 2008). DOI: 10.1088/0264-9381/26/2/025005. URL: http://arxiv.org/abs/0807.2045%20http://dx.doi.org/10.1088/0264-9381/26/2/025005.

[26] Fabian Meylahn and Benno Willke. “Characterization of Laser Systems at 1550 nm Wavelength for Future Gravitational Wave Detectors”. In: *Instruments* 6 (1 Mar. 2022). ISSN: 2410390X. DOI: 10.3390/instruments6010015.

[27] ETPathfinder. *ETpathfinder*. URL: https://www.etpathfinder.eu/gallery/.

Appendix A

Parameter table

Category	Parameter	Value
Cavity parameters	T_{IM}	3056 ppm
	L_{IM}	50 ppm
	R_{IM}	0.9969
	T_{EM}	6.405 ppm
	L_{EM}	50 ppm
	R_{EM}	0.999936
	r_c	-0.9644
	F	1984
	IM and EM ROC	14.5 m
	Cavity length	9.22 m
Light and modulation	λ	1550×10^{-9} nm
	ω_0	3.216×10^{15} rad/s
	E_{in}	1 W
	f_{lock}	12.3 MHz
	m	0.1
	J_0	0.9975
	J_1	0.04994
	Ω	77.283×10^9 rad/s
	β	0.08208
Central ITF	l_{Schnupp}	0.1 m
	Length BS to IM	6.406 m
	ϕ_M	2.114°
	T_{FM}	5000 ppm
	R_{FM}	0.995
	L_{FM}	0
	Operating temperature	120 K

TABLE A.1: Parameters for ETpf used in simulation

Appendix B

Pictures of ETpathfinder

FIGURE B.1: Picture showing the construction of the interferometer. Each tower will contain suspended optics and measurement equipment [27].

FIGURE B.2: Picture displaying one of the ETpf towers with humans for scale. Taken during the ETpf workshop in February, 2023.

Appendix C

Simulated sensing matrix without folding mirrors

The simulated sensing matrix without folding mirrors in $\mathrm{W}/^{\circ}$ is given by:

$$\mathbf{M}_{\text{simulation, no FM}} = \begin{bmatrix} M_{CRI} & M_{MRI} & M_{DRI} \\ M_{CRQ} & M_{MRQ} & M_{DRQ} \\ M_{CAI} & M_{MAI} & M_{DAI} \\ M_{CAQ} & M_{MAQ} & M_{DAQ} \end{bmatrix} \tag{C.1}$$

$$= \begin{bmatrix} 2.0495 \times 10^{0} & 6.0628 \times 10^{-9} & -3.0565 \times 10^{-8} \\ -2.2246 \times 10^{-4} & 4.0249 \times 10^{-5} & -2.0295 \times 10^{-4} \\ 1.1201 \times 10^{-2} & -4.6061 \times 10^{-9} & -6.0674 \times 10^{-6} \\ -8.7542 \times 10^{-5} & -4.0249 \times 10^{-5} & -5.3017 \times 10^{-2} \end{bmatrix} \tag{C.2}$$

The normalised version of this matrix is:

$$\mathbf{M}'_{\text{simulation, no FM}} = \begin{bmatrix} 1.00000 & 0.00000 & -0.00000 \\ -0.73225 & 0.13248 & -0.66802 \\ 1.00000 & -0.00000 & -0.00054 \\ -0.00165 & -0.00076 & -1.00000 \end{bmatrix} \tag{C.3}$$

Appendix D

Noise budget plots

D.1 Laser frequency noise

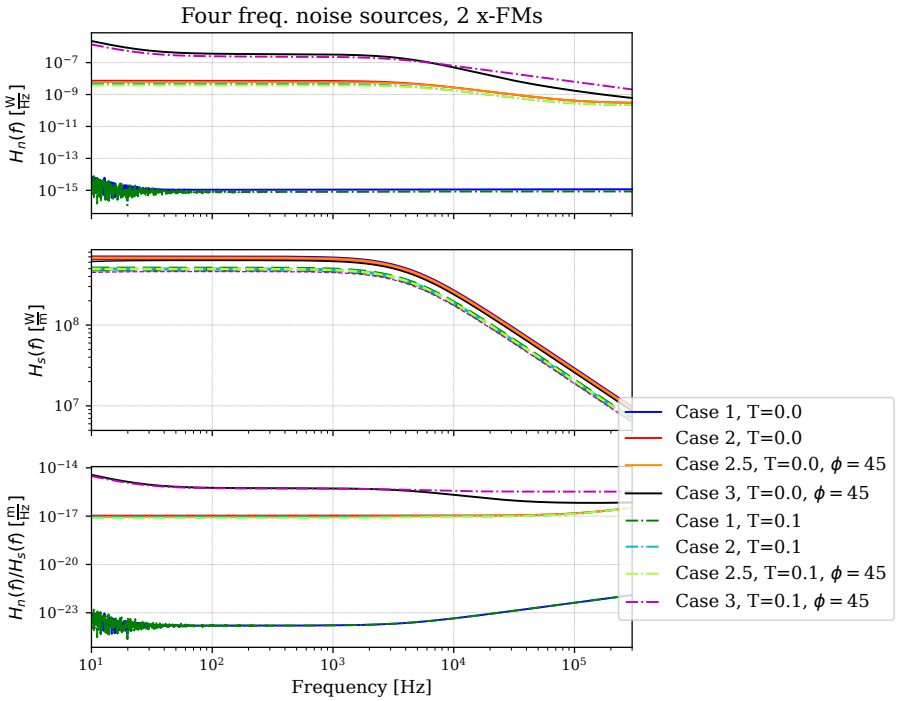

FIGURE D.1: Frequency noise and signal transfer functions for two x-FMs with etalon tuning $\phi = 45°$. The four cases are plotted for folding mirror transmittance $T = 0$ and $T = 0.1$.

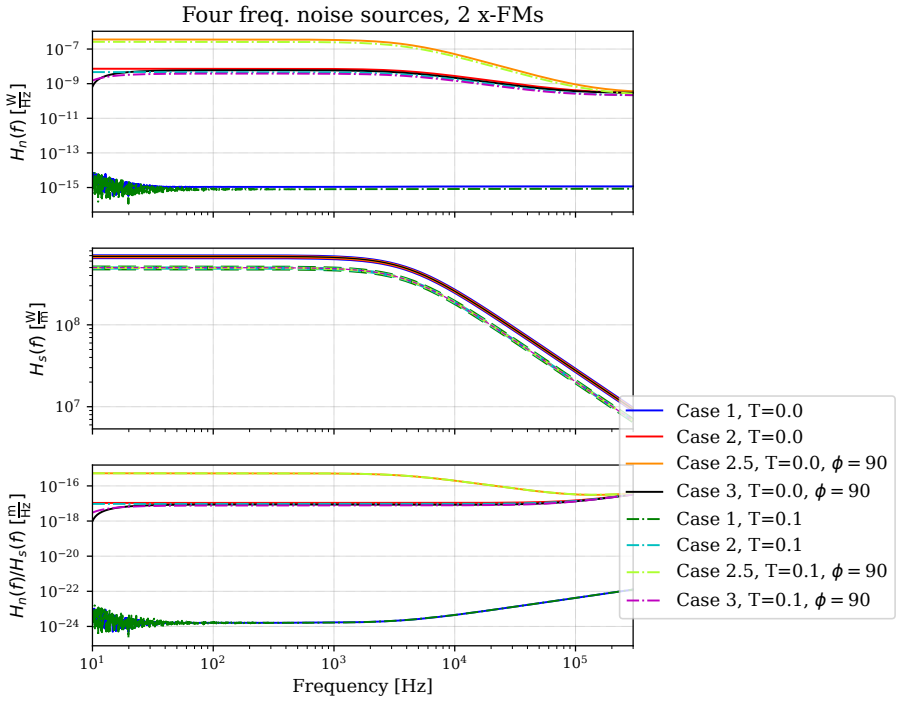

FIGURE D.2: Frequency noise and signal transfer functions for two x-FMs with etalon tuning $\phi = 90°$. The four cases are plotted for folding mirror transmittance $T = 0$ and $T = 0.1$.

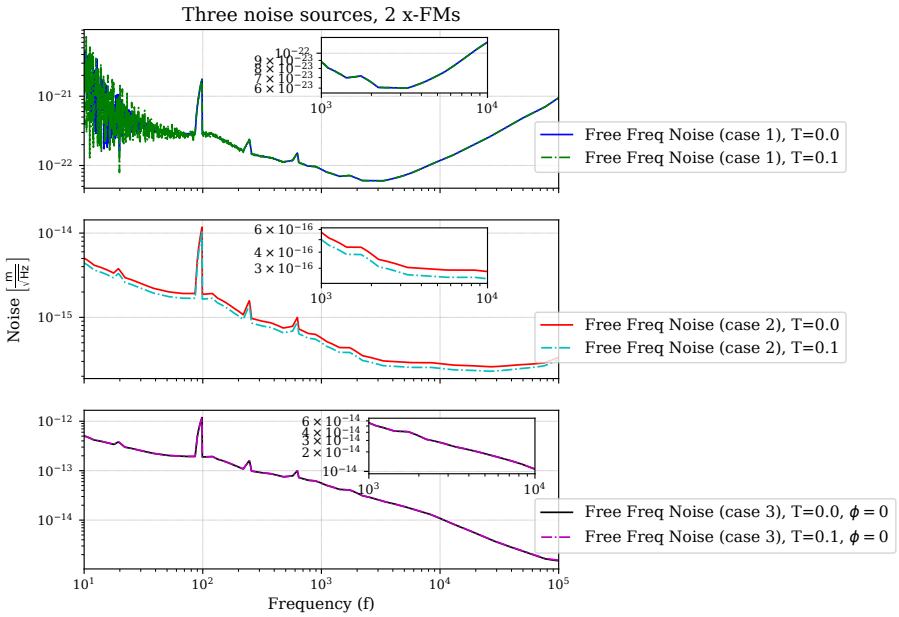

FIGURE D.3: Frequency noise spectrum before suppression.

D.2 Laser amplitude noise

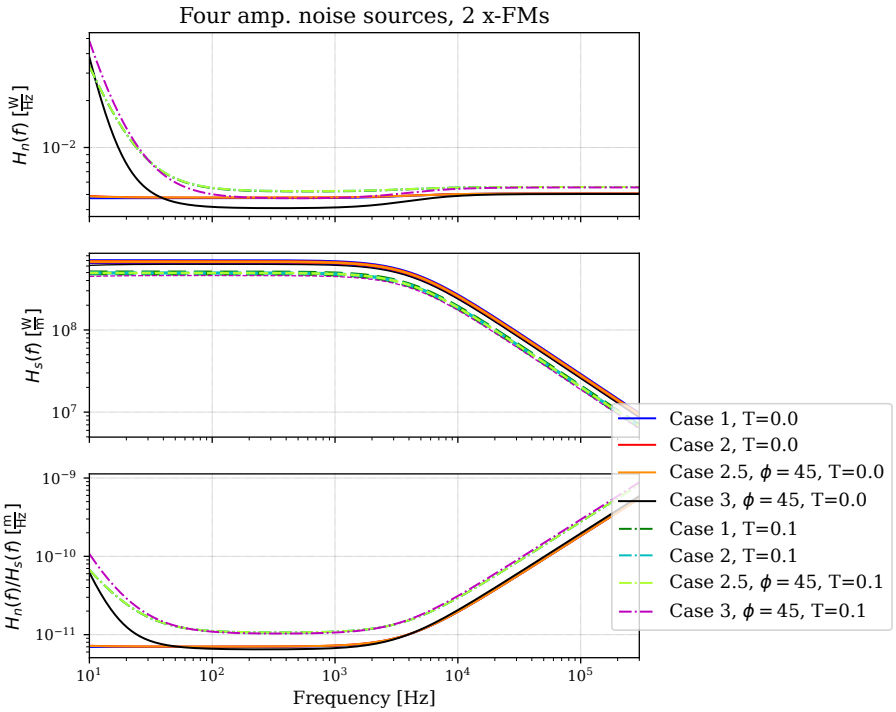

FIGURE D.4: Amplitude noise and signal transfer functions for two x-FMs with etalon tuning $\phi = 45°$. The four cases are plotted for folding mirror transmittance $T = 0$ and $T = 0.1$.

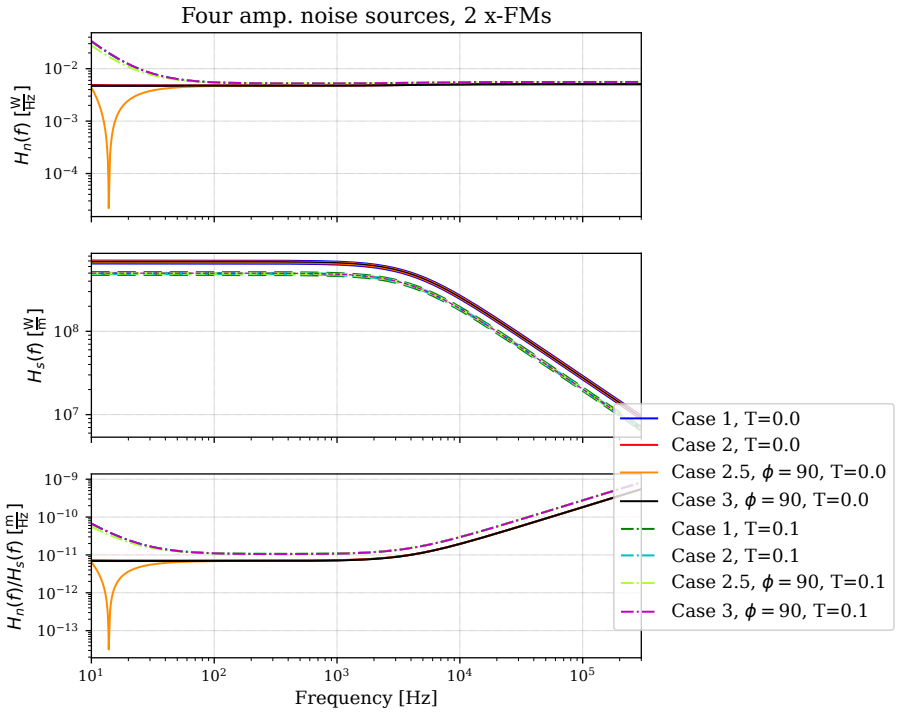

FIGURE D.5: Amplitude noise and signal transfer functions for two x-FMs with etalon tuning $\phi = 90°$. The four cases are plotted for folding mirror transmittance $T = 0$ and $T = 0.1$.

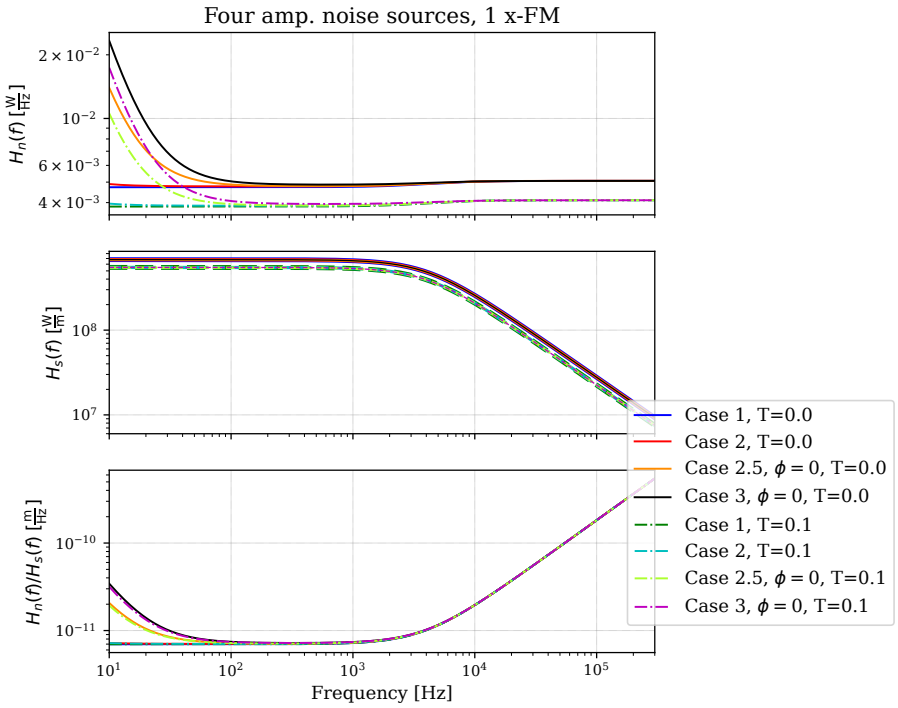

FIGURE D.6: Amplitude noise and signal transfer functions for one x-FMs with etalon tuning $\phi = 0°$.